Study of Fueling by Supersonic Molecular Beam Injection in the GAMMA 10 Tandem Mirror

Md. Maidul Islam

February 2018

Study of Fueling by Supersonic Molecular Beam Injection in the GAMMA 10 Tandem Mirror

Md. Maidul Islam
Doctoral Program in Physics

Submitted to the Graduate School of
Pure and Applied Sciences
in Partial Fulfillment of the Requirements
for the Degree of Doctor of Philosophy in
Science

at the
University of Tsukuba

Contents

Chapter 1
Introduction

1.1 Necessity of Nuclear Energy

Our beloved world is now moving to industrial one and hence safe, secured, and unlimited source of energy is needed to meet the future energy demand. There are various sources of energy. The most popular source of energy is the fossil fuels, such as coal, oil and natural gas. In the case of fossil fuels, depletion is of special concern and over consumption can lead to serious environmental issues such as air pollution due to releasing carbon dioxide gas when it is burnt. In the case of renewable energy sources such as solar and wind power, the stable power cannot be supplied because it often relies on the weather for its source of power. Stable electric power is essential for manufacturing factories. An energy source that can produce a lot of energy is the nuclear power. There are two processes to produce the nuclear power. One is fission process in which the nucleus of an atom is split into lighter nuclei of nearly equal size and release a large amount of energy. The other is fusion process in which the nuclei of atom are combined together to form a heavier nucleus and release huge amount of energy. Nuclear power has an advantage of producing huge stable power. However, there is safety problem in the case of fission plants. One of the most difficult problems is to manage high-level radioactive wastes from fusion power plants. We must control these high-level radioactive wastes for over tens of thousands of years.

Nuclear fusion process is more safety than nuclear fission process because there are no nuclear chain reactions in nuclear fusion. In nuclear fusion reactions, small amount of helium ash is produced which is inert gas and will not pollute the atmosphere. The deuterium-tritium (D-T) is selected for thermo-nuclear fusion process because of its large reaction cross-section [1]. Deuterium can be extracted from seawater and tritium is produced from lithium which is found in the earth`s crust. Research on fusion study started in 1950s. Many experiments related to nuclear fusion have been carried out in the world. In order to demonstrate the possibility of fusion reactor, International Thermonuclear Experimental Reactor (ITER) has been under construction at Cadarache, France [2]. The schematic view of ITER is shown in Fig. 1.1. If ITER can finish its mission successfully, then it can solve our future energy demand which satisfies all necessary requirements of the future energy source.

1.2 Importance of Fueling System

Establishment of fueling system is one of the critical issues for the future fusion reactor. There are four control factors of heat and particle transport in fusion plasmas which are fueling system, heating system, exhaust system and heat removal system. In order to obtain the high performance plasma, particle control is a very important issue in the plasma confinement devices. To obtain the high
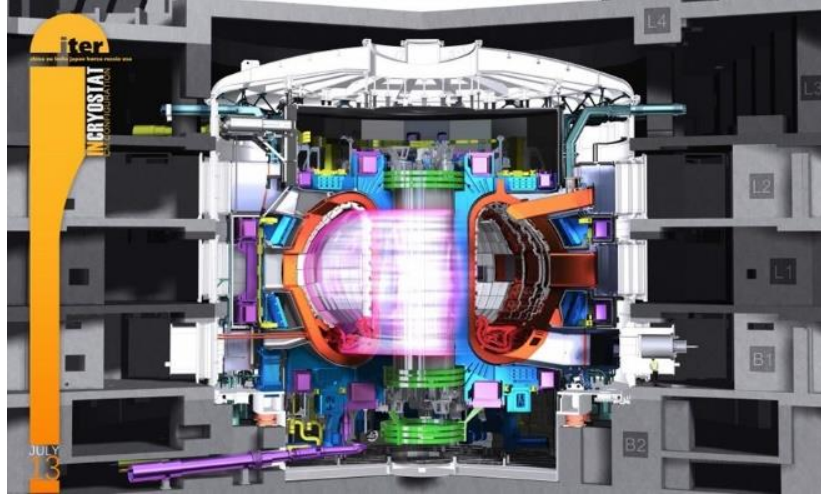
Fig. 1.1 The Schematic view of nuclear fusion reactor ITER.

performance plasma, control of the neutral particle in the peripheral region is very important issue. Reduction of the neutral particle in the peripheral region is very important as an index the efficiency of particle supply. It has been reported that neutral particles in the peripheral region have a sufficient influence on the plasma condition in a core region and transition phenomena of the plasma confinement mode [3, 4].

Fueling control enables the profile control of the core plasma density and reduction in neutral particles in the peripheral area. Pellet injection (PI) can reduce the edge recycling and help to obtain a peak density profile, which is important for obtaining better confinement [5]. PI has become a standard and powerful refueling method, after more than 20 years of enthusiastic effort. Although this system is suitable for device ITER-like tokamaks, the system is complicated and it is not easy to make a pellet small enough for density control in medium or small devices. On the other hand, supersonic molecular beam injection (SMBI) developed by L. Yao et al. [6], is suitable for future ITER-like tokamaks as well as small device like GAMMA 10 [7-11]. SMBI is very simple and economically feasible to develop and maintain. SMBI gives high-speed and high-directive gas injection because of higher plenum pressure compared to the conventional gas puffing and it can inject neutral particles deeper into the core plasma.

1.3 SMBI Experiments in Fusion Devices

Supersonic molecular beam injection (SMBI) experiments has been carried out in many fusion devices in the world and treated as different names like SSGP, SPGI, SGI-U, etc. The SMBI experiments in the famous devices are explained as follows:

● *SMBI in HL-2A*

Supersonic molecular beam injection (SMBI) has been installed on the HL-2A tokamak.

2

Prof. L. Yao who developed the SMBI system first started to develop the supersonic molecular beam injection on HL-1M [12-15]. The arrangements of SMBI in HL-2A tokamak is shown Fig. 1.2. Two types of SMBI system; high field side injection (HFS) and low field side injections (LFS) have been installed in HL-2A tokamak. The valve of LFS SMBI is an electromagnetic valve, which is the same type used for SMBI in GAMMA 10. On the other hand, the valve for HFS SMBI is a pneumatic valve, which is the same type used in tore supra [13]. The distance from the plasma to LFS nozzle is ~1.28 m. The fueling efficiency is defined as the ratio of the increment of the plasma content divided by the number of injected particles. The fueling efficiency is estimated to be 30 ~ 60%. The fueling efficiency of HFS SMBI is higher than that of LFS SMBI. It was also reported that H-mode was triggered by SMBI instead of pellet injection in HL-2A [16]. Recently a conic nozzle with a diameter of 0.5 mm and half angle of 8° is installed on the valve of LFS SMBI [17].
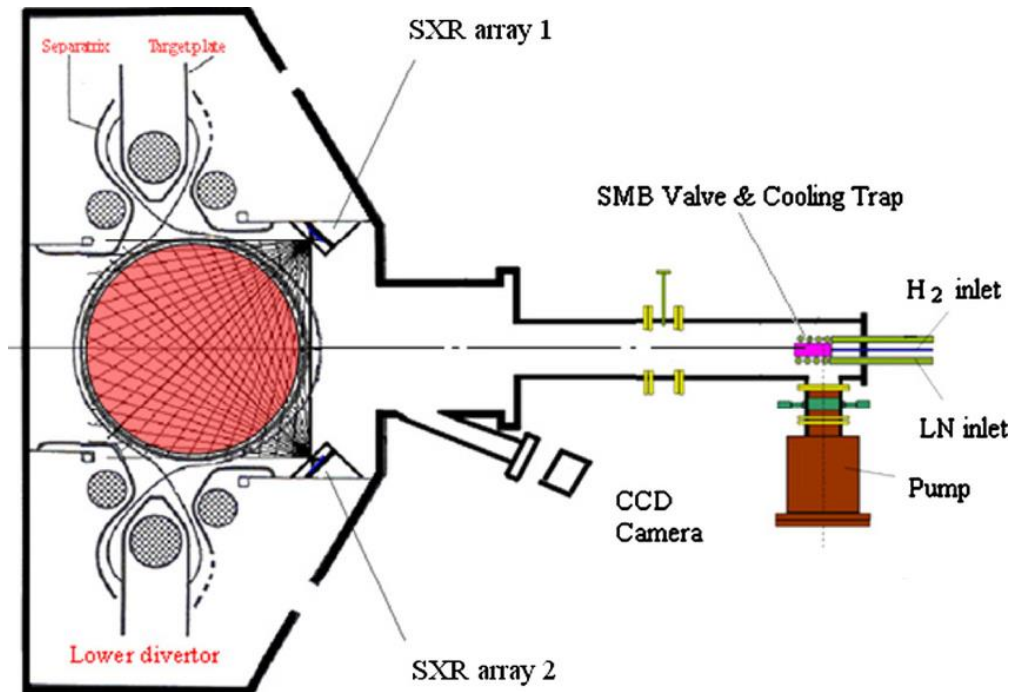
Fig. 1.2 Arrangements for SMBI in the HL-2A [12].

● *SSGP in Large Helical Device (LHD)*

Supersonic gas puffing (SSGP) has been installed in the largest superconducting helical device in the world (LHD) as shown in Fig. 1.3 [9, 18, 19]. The fueling efficiency depends on target plasma density and increases as the plasma density decreases and reported that this is due to the fueling mechanism of SSGP, where the fuel particles are supplied to the edge region of plasma and then transported to the core region by diffusion. The fueling efficiency about ~20% is achieved at low plasma density (1.5×10^{19} cm^{-3}) which is more than two times higher than that of conventional gas puffing at the same density.
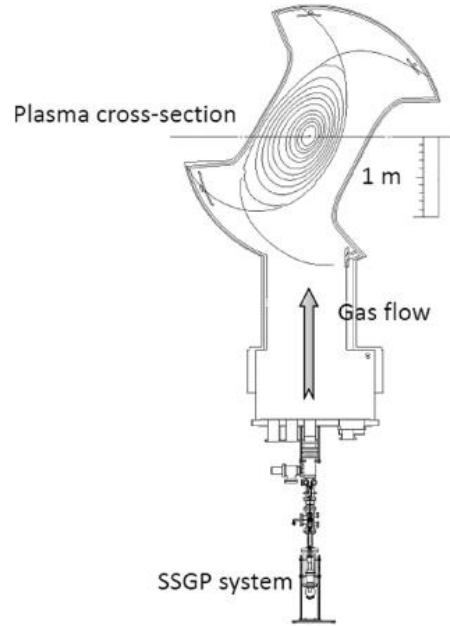
Fig. 1.3 Arrangements for SSGP in the LHD [9]

● *SPGI in Tore Supra*

In Tore Supra tokamak, supersonic pulsed gas injection (SPGI) has been installed [20, 21]. The arrangements of SPGI in Tore Supra is shown Fig. 1.4. Two types of SPGIs have been installed in Tore Supra. The fueling efficiency of SPGI is 30 ~ 60% which is three or four times higher than that of GP. The fueling efficiency from the LFS tends to be better than that from the HFS. The fueling efficiency in the divertor discharges is lower than that in the limiter discharges. The edge cooling effect of SPGI has been observed in Tore Supra. It is revealed that SPGI reduced wall inventory compared to a similar conventional gas puffing in one long pulse discharge.
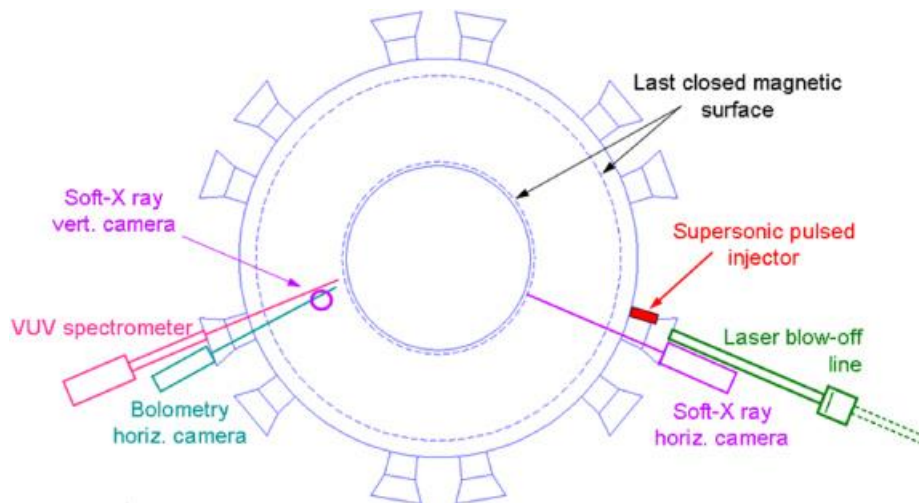
Fig. 1.4 Arrangements for PGI in the Tore Supra [20]

● *SMBI in JT-60U*

In JT-60U tokamak, SMBI has been installed [22, 23]. The SMBI system in JT-60U is the same as

that used in Tore Supra. The arrangements of SMBI in JT-60U is shown Fig. 1.5. The backing pressure is 0.2 ~ 0.6 MPa. The injection frequency is less than 10 Hz and the pulse length of one pulse is ~2 ms. It is revealed that the fueling efficiency of SMBI exhibited a weak dependence on backing pressure and injection direction (high and low field side injections). It is also reported that the fueling efficiency defined as a ratio of increase in the total electron number to the injected electron number is estimated to be ~20% when it is assumed that the density increase uniformly in the whole plasma and ~50% when it is assumed that the density increases only in the peripheral region (r/a = 0.96-1.0). The fueling efficiency of SMBI is higher than that of GP. It is also reported that the plasma response for SMBI is also faster than that for GP.
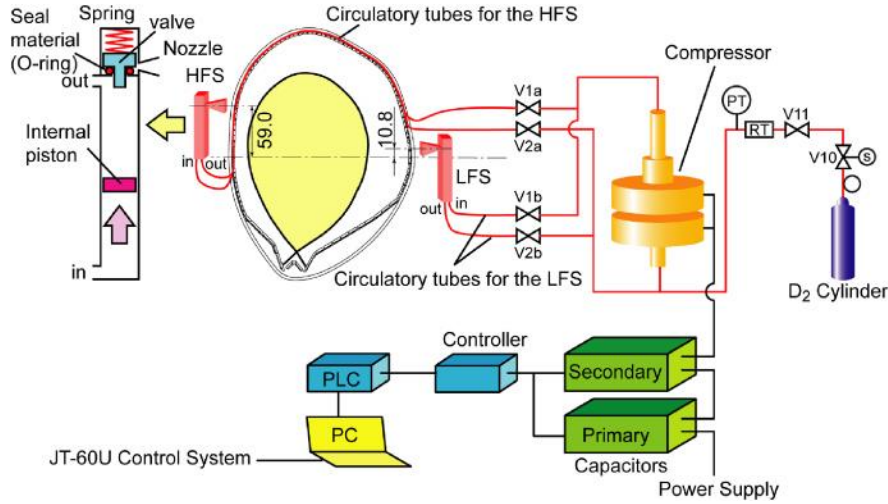
Fig. 1.5 Arrangements for SMBI in the JT-60U [22]

● *SMBI in Heliotron J*

In Heliotron J, SMBI has been installed [24-26]. Heliotron J is a helical type device. The arrangements of SMBI in Heliotron J is shown Fig. 1.6. It is reported that the fueling efficiency is estimated to be about 50 ~ 60% for NBI and 20 ~ 30% for ECH + NBI discharges at n_e ~ 1×10^{19} m^{-3}.
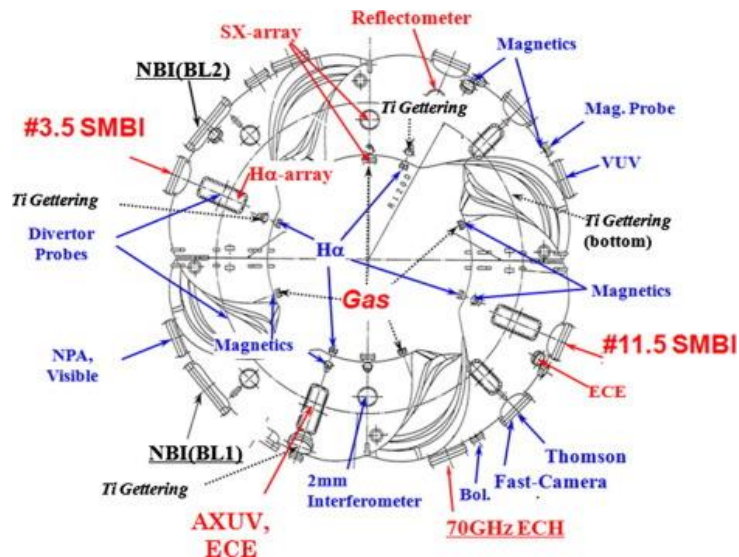
Fig. 1.6 Arrangements for SMBI in the Heliotron J [24]

The stored energy reaches to ~ 4.5 kJ for ECH with both NBI and SMBI fueling, which is about 50% higher than the maximum one achieved so far under the similar heating condition with conventional gas puffing fueling [25].

- *SPGI in ASDEX-U*

In the ASDEX-U tokamak, supersonic pulsed gas injection (SPGI) has been installed. [27]. The SPGI is the same type of SPGI installed in Tore Supra. The fueling efficiency is ~ 30% for L-mode and low density H-mode plasmas. In contrast, the fueling efficiency is reduced to less than 15% in high density H-mode discharge. The possibility of type-I edge localized modes (ELMs) pacing in H-mode plasmas by 2 Hz gas injection is investigated in ASDEX-U.

- *SGI-U in NSTX*

Supersonic gas injector upgrade (SGI-U) has been installed in the NSTX tokamak [28, 29]. The arrangements of SGI-U in NSTX is shown Fig. 1.7. The SGI-U device consists of a small converging diverging graphite Laval nozzle and a piezoelectric gas valve. The backing pressure is up to 5000 Torr (~ 0.7 MPa). The fueling efficiency is estimated to be about 10 ~ 40%, which is defined as the ratio of the total electron inventory N_e differentiated with time to the particles supply by SGI-U.
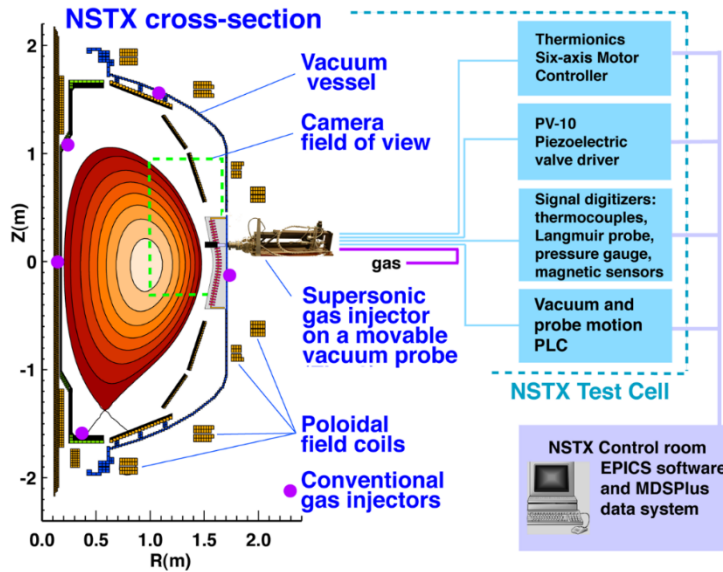
Fig. 1.7 Arrangements for SGI-U in the NSTX [28]

- *SMBI in EAST Tokamak*

Supersonic molecular beam injection (SMBI) has been installed in the EAST tokamak [30]. It is reported that the fueling efficiency of SMBI in EAST tokamak is 15-30%, which is higher than conventional gas puffing and the shorter delay time of SMBI makes it more promptly to feedback control the plasma density.

1.4 SMBI in GAMMA 10

As shown in Sec. 1.3, various famous fusion devices has been performed SMBI experiments and the effectiveness of SMBI has been demonstrated. However, the above tokamak devices are very complicated and difficult to investigate the physical mechanism in high performance plasmas. On the other hand, GAMMA 10 is an open system tandem mirror device which has very simple configuration and have many observation ports to observe the plasma behavior. Consequently, GAMMA 10 is a suitable device of fueling studies. GAMMA 10 is the world largest tandem mirror and an open magnetic plasma-confining device with thermal barrier [31-34]. The detail of the GAMMA 10 tandem mirror will be described in chapter 2. A schematic view of GAMMA 10 tandem mirror is shown in Fig. 1.8.

SMBI experiment in GAMMA 10 has been started several years ago with collaboration research program of Kyoto University [24, 35, 36]. In GAMMA 10, SMBI system has been installed at near the midplane in the central-cell. The central-cell of GAMMA 10 has a simple solenoidal magnetic configuration with ten pancake coils. The first SMBI experimental results with only valve case showed that SMBI achieved higher density plasmas at the core region than the conventional gas puffing [8]. It is also reported that the degree of diffusion of the injected neutral particles decreases with increase of SMBI plenum pressure. In order to improve the directivity of the molecular beam, a straight nozzle has been installed at the top of the SMBI valve. It is reported that the directivity of the molecular beam was improved [10]. In the previous study, SMBI experiments in GAMMA 10 have been performed only ICRF heated plasma by using straight nozzle and only valve case. SMBI experiments with Laval nozzle has also been started. However, the Laval nozzle was broken during the experiments and the detailed characterization of the Laval nozzle had not been performed.

In this study, SMBI experiments by using the Laval nozzle is carried out in the central-cell at the same position in order to investigate the characteristic of the Laval nozzle [7]. In order to study the heating effect during SMBI, electron cyclotron resonance heating (ECRH) is also applied and plasma behavior is investigated.

In GAMMA 10, hot ion mode plasma is produced in the central-cell. The stored energy is reduced during SMBI. Recently, the SMBI experiments is performed another region in GAMMA 10 in order to improve the plasma parameter. In order to carry out this experiments, we searched ports at different region in GAMMA 10. The only available port was at the top of east anchor inner-transition region of east anchor-cell. Therefore, SMBI system with new type short size Laval nozzle is installed in the east-anchor inner-transition region in GAMMA 10 (EA-SMBI) in order to know the fueling characteristics and plasma behavior is investigated by varying plenum pressure and SMBI pulse width.
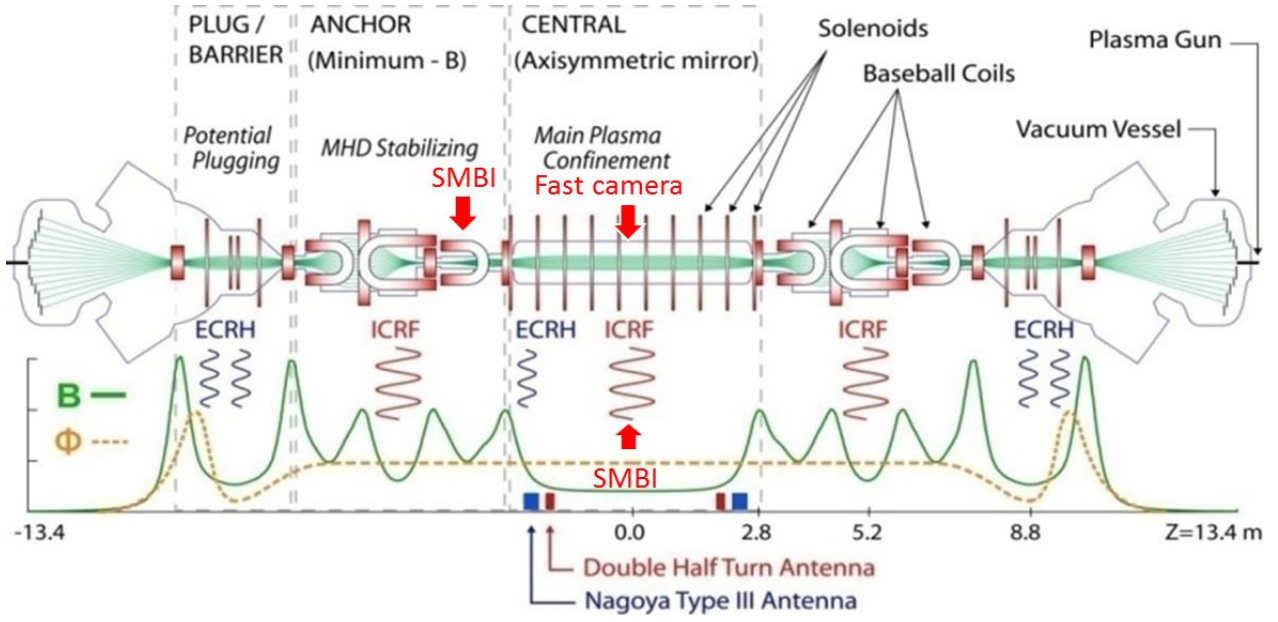
Fig. 1.8 Location of SMBI experiments in GAMMA 10.

1.5 Neutral Transport during SMBI

It is important to study the neutral transport during SMBI for optimizing fueling characteristics to the plasma. Three-dimensional Monte-Carlo code DEGAS is applied to GAMMA 10 in order to investigate precisely the spatial distribution of neutral particle density during SMBI. The DEGAS code is a simulation code which simulates the neutral transport [37, 38]. In this code, Monte-Carlo method is used for the particle tracking analysis. In this model, interior components such as the limiters and antennas for ICRF heating are included in the detailed structure. SMBI injection port and a nozzle for SMBI are newly installed in this mesh model [10]. By the numerical simulation of the neutral particles, the neutral densities are determined in the whole 3-dimensional meshes. Based on the neutral density, Hα emission in the each mesh is calculated on the basis of a collisional-radiative model (CR-model). The calculated Hα emission is compared with calibrated measurement results by the Hα line detectors and the high-speed camera. This coupling method is quite useful for analyzing the complicated neutral behavior.

In order to simulate the molecular beam injected by SMBI, σ_{div} is introduced as an index the divergence angle of the initial particle. If the angular profile of launched particles has a cosine distribution, it is defined to be unity ($\sigma_{div} = 1.0$). The axial and radial profile of neutral transport is investigated for different value of divergence angle index. In the previous simulation study, neutral transport during SMBI is investigated by decreasing the divergence angle index. However, the energy was not conserved when decreasing the divergence angle index. In this simulation study, the code is modified in order to conserve the energy. When the value of divergence angle index is less than unity,

the divergence of the launched particles is reduced. The perpendicular velocity component of the initially injected particle is reduced in the case of $\sigma_{div} < 1.0$. The parallel component of the velocity along the fueling direction is modified to conserve the energy and the results are compared after velocity modification. The simulation results after energy conservation well explains the GAMMA 10 SMBI experimental results with Laval nozzle. The simulation is also performed by changing background plasma parameter.

1.6 Purpose and outline of the thesis

The purpose of this study is to investigate the detailed fueling characteristics by SMBI with Laval nozzle in GAMMA 10 tandem mirror device with simplified configurations in magnetic field. Furthermore, 3-dimentional neutral transport simulation code (DEGAS) is employed in order to clarify the neutral particle behavior during SMBI. These results enable us to contribute the study of neutral particle for the complicated devices such as helical type devices, or tokamak devices as represented by ITER.

Outline of the thesis is as follows; after introducing the first chapter, chapter 2 describes the feature of experimental arrangements and GAMMA 10 with the schematic views. Heating system, pumping system, fueling system, and diagnostic systems is also described. In chapter 3, the analytical method for neutral transport is explained in detail. The measurement principle of Hα emission is mentioned. The analysis method by using CR-model and Monte-Carlo simulation method are also explained. In chapter 4, results of SMBI experiment in the central-cell and anchor-cell is described based on 2-dimentional image captured by high-speed camera and Hα detector. In chapter 5, the neutral particle behavior is investigated during SMBI by using Monte-Carlo simulation code (DEGAS). In simulation results, the spatial distribution of neutral particle behavior on the plasma cross-section is discussed. Finally, in chapter 6 this thesis is concluded.

Chapter 2
Experimental Arrangements

2.1 GAMMA 10 Device

The GAMMA 10 at the University of Tsukuba is an axi-symmetrized tandem mirror device with thermal barrier [31]. It consists of central-cell, anchor-cells, plug/barrier-cells, and end-cells. Midplane of the central-cell is z = 0 cm and west and east sides correspond to plus and minus in z-axis, respectively. The vertical and horizontal direction is considered as x and y axes with these origins at the machine axis. The central-cell is the main region to confine plasma and 6 m in length and the diameter of 1 m. In the standard operation, the magnetic strength in central mid-plane is 0.405 T and the mirror ratio of the central-cell is 5. Mirror-throat regions which exist between the central-cell and each anchor-cell have the first mirror with strong magnetic field for the confining plasma in the central-cell. The anchor-cells are connected to the central-cell via both mirror throat regions. The anchor-cell has non-axisymmetric magnetic structure with minimum-B configuration for the MHD stability. The plug/barrier cells are located at the outside of both anchor-cells. Plug potential, which is produced with electron cyclotron heating, confines the plasma from the central-cell and anchor-cells. In the central cell and plug/barrier cells, the axisymmetric mirror magnetic field is produced by circular coils. The minimum-B field in the anchor cell is produced by the main baseball coil which is bounded two trace-coils and two small baseball coils for recircularization of the magnetic flux tube. Figure 2.1 shows the schematic view of the GAMMA 10 tandem mirror. The vacuum vessel, coil
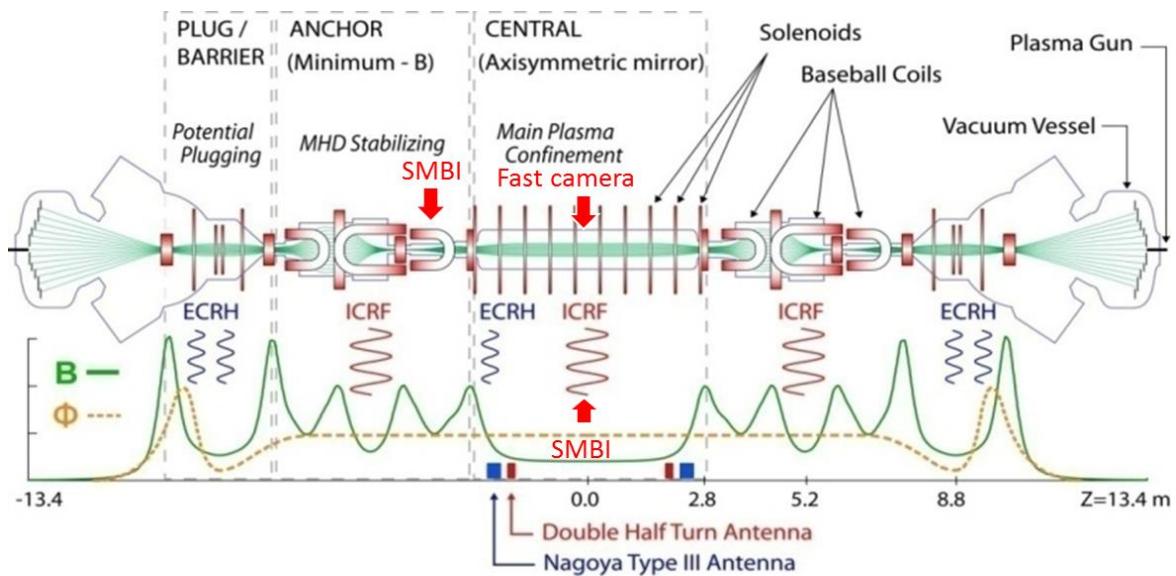

Fig. 2.1 Schematic view of the GAMMA 10 tandem mirror. It shows location of SMBI and heating system, coil arrangement, magnetic field profile and the potential of the plasma.

arrangements, magnetic field profile and the potential of the plasma is shown in the figure. In standard hot-ion mode plasmas, initial plasma is build up by plasma guns located in both ends. Then plasma is sustained by gas puffing coupling with ion cyclotron heating. ECRH and neutral beam injection (NBI) are additionally supplied for the plasma production and heating.

2.2 Plasma Production

For starting up the plasma, two plasma guns using magneto-plasma-dynamic (MPD) jet are installed in both ends of GAMMA 10. In GAMMA 10, the operation gas is hydrogen. The plasmas produced by these guns are injected into the central cell along the magnetic field lines by J×B force. The initial plasma produced by the plasma gun can build up the plasma in the central cell effectively with the gas puffing and heating systems. The pulse length of the arc plasma is usually 1 ms.

2.3 Pumping System

There are three types of pumping systems in GAMMA 10, which are turbo-molecular pumps (TMP), helium cryosorption pump systems (CP), and liquid helium cryopanel (LHP) systems. TMPs are mounted in the central-cell, the anchor-cells, and the end-cells. The TMP in the end-cells and one of the central-cell have the pumping speed of 15,00 l/s, the pumping speed of other TMP are 2,500 l/s. CPs are mounted in the central-cell, end-mirror tanks, east barrier NBI tank, and the end cells. One in the central cell has the pumping speed of 10,000 l/s, and the others have 1,800 l/s for hydrogen gas. LHPs are located on the end-mirror tanks and on the anchor NBI tanks. The LHP consists of stainless steel panels cooled to 3.5 K by the liquid helium. The pumping speeds located on the end-mirror tanks and on the anchor NBI tanks are $9.0×10^5$ l/s, $4.0×10^5$ l/s, respectively.

2.4 Limiters

In the GAMMA 10 central-cell, its plasma boundary is determined by using three limiters. Central limiter is located at z = +30 cm, the other (west and east limiters) are located at z = 100 cm and z = -155 cm, respectively. The central limiter is the fixed type of limiter and 400 (or 360) mm in diameters, while the another (iris limiters) are radially variable type of limiters. The diameter of the limiter can be changed within 340 mm to 400 mm.

2.5 Heating Systems

2.5.1 Ion cyclotron range of frequency (ICRF) systems

In GAMMA 10, ICRF systems are used for the production and heating of the plasmas [39, 40]. Two kinds of ICRF antennas are installed in GAMMA 10 for the standard operation. These antennas are located at the both ends of the central-cell. For the ion heating and plasma production, one is

called RF1 system connected to the NAGOYA TYPE-III antenna, which excite ICRF fast waves (RF1; ~10MHz) for the plasma production and/or ion heating in the anchor-cells. For the ion heating in the central-cell, RF2 heating system is used with double-half-turn antenna by using ICRF slow wave (RF2; 6.36 MHz) which corresponds to the ion cyclotron resonance frequency (ω_{ci}) near the central-cell midplane.

2.5.2 Electron cyclotron resonance heating (ECRH) system

ECRH system has been installed in the GAMMA 10 tandem mirror device [33, 41]. ECRH systems with four 28 GHz gyrotrons are applied to create the confining potentials in the plug/barrier-cells. The axial-confining potentials for ion are formed by plug ECRH (P-ECRH) at a position where the magnetic field strength is 1 T. The heating point has a steep slope of the magnetic field. Barrier ECRH (B-ECRH) systems are used at the barrier midplane so as to form a negative potential relative to the central-cell. The central-cell ECRH (C-ECRH) system consists of a gyrotron with the frequency of 28 GHz. The aim of this system is the heating of the electron in the central-cell in order to suppress the ion energy loss caused by electron drag.

2.5.3 Neutral beam injection (NBI) systems

Three NBI systems are used for the ion heating or sustaining the potential in the both barrier regions to produce sloshing ion (sloshing NBI). The sloshing ions contribute to the sustainment of the potential dip of thermal barrier. The NBI systems in the anchor-cell are used for the fueling and heating and MHD stabilization by injecting 25 keV neutral hydrogen beams into the anchor-cell midplane. The other NBI system is installed in the central-cell for ion heating and fueling.

2.6 Fueling System

2.6.1 Conventional gas puffing

The conventional gas puff system has been used since early fusion plasma experiments. Fuel gas is injected into the vacuum vessel and supplied to the edge plasma. Piezo electric valves are often used in this system. This system has a drawback of low fueling efficiency. Especially in high performance plasma, most of the particles supplied by gas puffer are ionized in peripheral region of the plasma. Main gas puffer has been installed at the both of the central cell in GAMMA 10.

2.6.2 Pellet injection

The ice pellet injection system is considered as a favorable method to refuel magnetically confined plasma. Hydrogen gas is cooled by a refrigerator to ~10 K to create ice pellets. The advantage of this system is high fueling efficiency reaching 100 %. The density of the core plasma effectively can be increased by ice pellet injection. In the previous experiments, fueling by using pellet injection system was carried out in GAMMA 10 [42-45]. This system consists of a pipe-gun type pneumatic pellet

injector system made by the Oak Ridge National Laboratory and modified by Plasma Research Center of the University of Tsukuba [46]. The eight barrels are mounted into the injector and inner diameters of the barrels are 0.39, 0.58, 0.79 and 0.99. The pellet was injected from under the midplane of the central cell through the 6 m length of Teflon tube with the 1/4 inch inner diameter.

2.6.3 Supersonic molecular beam injection

Supersonic molecular beam injection (SMBI) system has been developed as a new fueling method that can combine both advantage of the conventional gas puffer and the pellet injection [6]. SMBI provides high-speed and high-directive gas injection by using a plenum pressure higher than that is used in the conventional gas puffing, so that the neutral particles can be injected deeper into the core plasma. In this system, high pressure gas is injected by using fast solenoid valve. SMBI is considered especially effective for small and relatively low-density devices such as GAMMA 10. SMBI system has been installed at the midplane of the central-cell in GAMMA 10 [7, 8].

Figure 2.2(a) shows the schematic view of SMBI system in the central-cell. The SMBI system consists of a fast solenoid valve with a magnetic shield and the top of the valve is connected with a nozzle. A fast solenoid valve of Parker-Hannifin Pulse Valves Series 9 is used for SMBI as shown in right side of Fig. 2.2(a). Prior to the experiment, the magnetic shielding vessel for the SMBI valve is modified by additional shielding and improved to prevent the effect of the external magnetic field to the operation of the valve as shown in Fig. 2.2(b). The Laval nozzle is widely used to design in modern aerospace and rocketry applications. This nozzle has three sections, one is the inlet section, another section is throat section, and the other is exhaust expansion section. Figure 2.3(a) shows the configuration of the Laval nozzle which is installed in the central-cell. The characteristic of Laval nozzle is that the temperature and pressure of gas decreasing as Mach number of exhaust gas increasing. In Fig. 2.3(b), the total view of the Laval nozzle is shown. The total length of the Laval nozzle is 363 mm and the diameter of throat and exit sections are 0.6 mm and 24 mm, respectively. The Laval nozzle is made of aluminum covered with a stainless steel plate to prevent the heat load onto the nozzle by the edge plasma, which is set close to the plasma boundary. In GAMMA 10, SMBI system with Laval nozzle is installed at the bottom of central-cell midplane at Z = -14.5 cm as shown in Fig. 2.4. The conventional gas puffing fueling system is also located in the central-cell at Z = +11.6 cm. The gas puffing experiment is also performed to compare with SMBI experimental results.

Recently, we develop a new type short size Laval nozzle in order to do SMBI experiment other than central-cell in GAMMA 10. This system is installed at the top of east anchor inner-transition region in GAMMA 10 in order to improve the plasma parameter. The new Laval nozzle is made of aluminum. The photograph of new Laval nozzle and after installation at the east anchor inner-transition are shown in Fig. 2.5(a) and Fig. 2.5(b), respectively. The diameter of throat and exit sections are 0.6 mm and 19 mm, respectively. The length between throat and exit of the nozzle is 157 mm and Mach number is 11.5. The theory of supersonic gas flow and design of new Laval nozzle is given in the appendix A [47-50].

(a)

GAMMA 10
Central-cell

High-speed
solenoid valve

Magnetic shield

Regulator

Power supply for pulse control

H₂
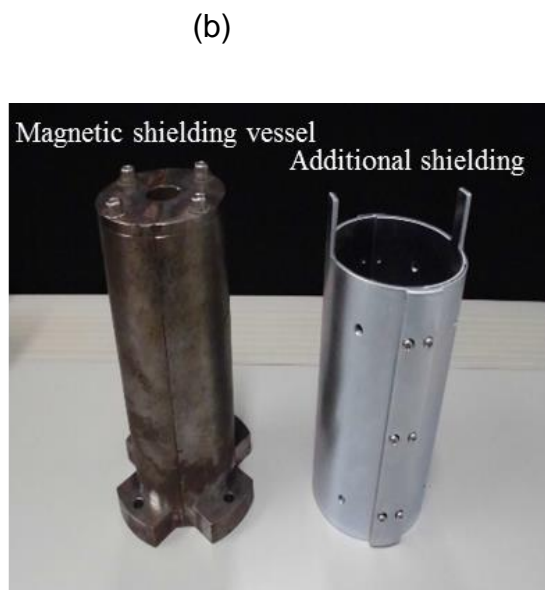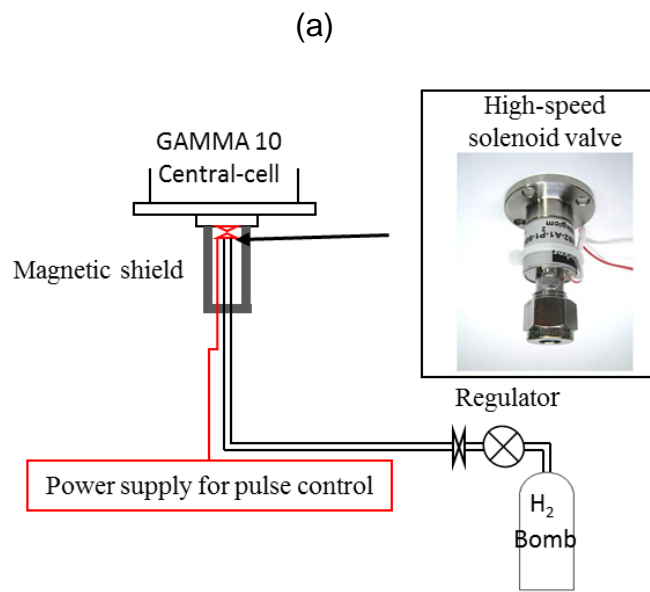Bomb

(b)

Magnetic shielding vessel
Additional shielding

Fig. 2.2 (a) Schematic view of SMBI system, (b) Magnetic shielding vessel and additional shielding,

(a)

Inlet section   Throat section   Exhaust expansion section
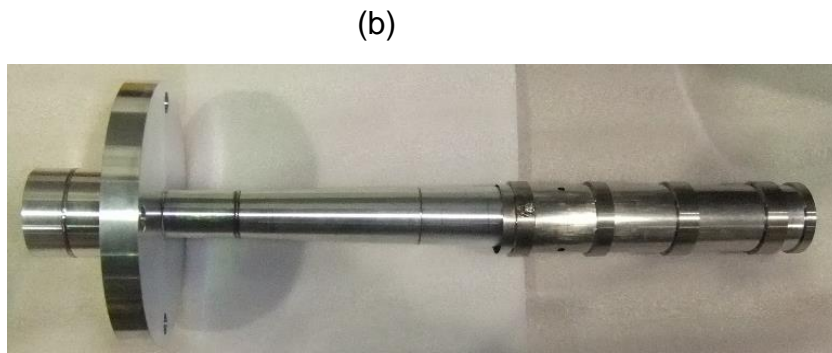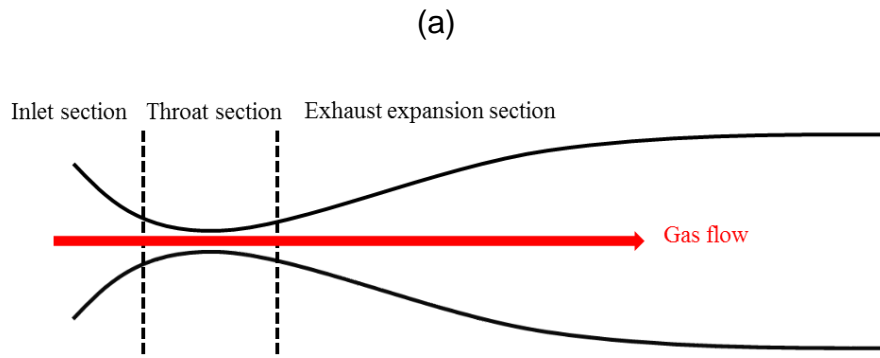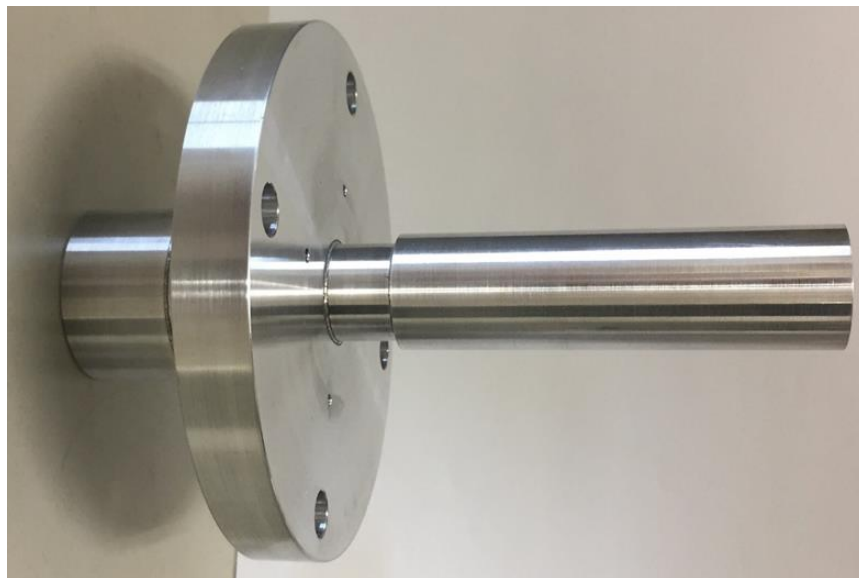
Gas flow

(b)

Fig. 2.3 (a) The configuration of the Laval nozzle (b) Photograph of the Laval nozzle.

Laval nozzle

Fig. 2.4 SMBI system installed at the bottom of central-cell mid-plane.

(a)

(b)

Fig. 2.5 (a) Photograph of the Laval nozzle, (b) New type SMBI system
installed at the top of east anchor inner transition region.

16

2.7 Diagnostics

2.7.1 Plasma pressure measurement

Diamagnetic loop are installed in the central cell to measure the central plasma pressure and anisotropy. Diamagnetic loop consists of the inner loop and the outer loop. The amount of diamagnetism is proportional to the product of the plasma density and temperature. The concentric loop can cancel the noise signal caused by the ripple of the magnetic field. In standard operation, it has been found that the ion temperature has been much higher than that of the electron.

2.7.2 Ion and electron temperature measurements

Radial profile of the ion temperature in the central cell midplane is measured by the charge-exchange neutral particle analyzer (CX-NPA). The power balance is investigated by using the results of the CX-NPA. Thomson scattering (TS) system is installed in the central cell for measuring the electron temperature [51]. TS system consists of laser, incident optics, light-collection optics, signal-detection electronics, and data recording system.

2.7.3 Plasma particle density measurements

The plasma line density is measured by micro wave interferometer systems. Microwave interferometers are installed in each cell of GAMMA 10 in order to measure the axial distribution of the line density. By using an Abel inversion technique with a radial scan measurement, the radial profile of the electron density at the central cell midplane can be determined. TS system is also used for measuring the electron density at the central cell.

2.7.4 End-loss ion energy analyzer

The end-loss ion energy analyzer is the device to measure the current density and the parallel ion energy of the end-loss flux [52, 53]. In GAMMA 10, arrays of ELIEA devices are installed in order to measure the end-loss ions with different positions along x-axis and y-axis. There are ten ELIEA devices in the east end region and twenty devices in the west end region. In one array of ELIEA, the locations of devices in radial distance (converted to the distance in central-cell) are set as: ch.1 = 2.59 cm, ch.2 = 5.26 cm, ch.3 = 8.25 cm, ch.4 = 11.19 cm and ch.5 = 14.64 cm.

2.7.5 Neutral particle measurement

Balmer-line emission measurement is often utilized for investigating neutral hydrogen behavior in many magnetically plasma confinement devices [54]. Hα line emission detector consists of the Hα interference filter, a lens, an optical fiber and photomultiplier. The emission selected by the interference filter is obtained and is transferred to the photomultiplier with optical fiber. The optical signal is converted to the electronic signal in photomultiplier. In order to measure the axial distribution of the neutral particles, a number of Hα detectors are installed at z =+100 cm, -1 cm, -71

cm, -141 cm -240 cm, -305 cm and -370 cm, etc. as shown in Fig. 2.6.

High-speed camera is also used for the estimation of the neutral particles in the plasma [55-57]. High-speed camera gives us the information of the edge plasma behavior because camera can captures the 2-dimensional images which help us instantly understand the plasma behavior. This advantage is useful for control the plasma position and fluctuation, and so on. High-speed camera captures the emission with visible light range. Spectroscopic measurement can perform by using high-speed camera with interference filter. The neutral particle behavior in the central-cell is investigated based on 2-dimentional image captured by high-speed camera. Figure 2.7 shows a cross-section of the GAMMA 10 central-cell, location of the SMBI system, and the optical arrangement for the high-speed camera. A high-speed camera is installed at central-cell to observe the plasma near the central limiter. The high-speed camera observes the two-dimensional (2-D; i.e., x-z, or y-z) response of the plasma to SMBI and is sufficiently capable of measuring visible-light emission. The photograph of high-speed camera system is shown in Fig. 2.8. By using dual blanch optical fiber bundles, the camera system has a line of sight in the horizontal direction and one in the vertical direction of the plasma cross-section. The expansion of the molecular beam injected by SMBI in the axial (z) direction and its penetration depth into the plasma can be estimated from the 2-D image in two directions.
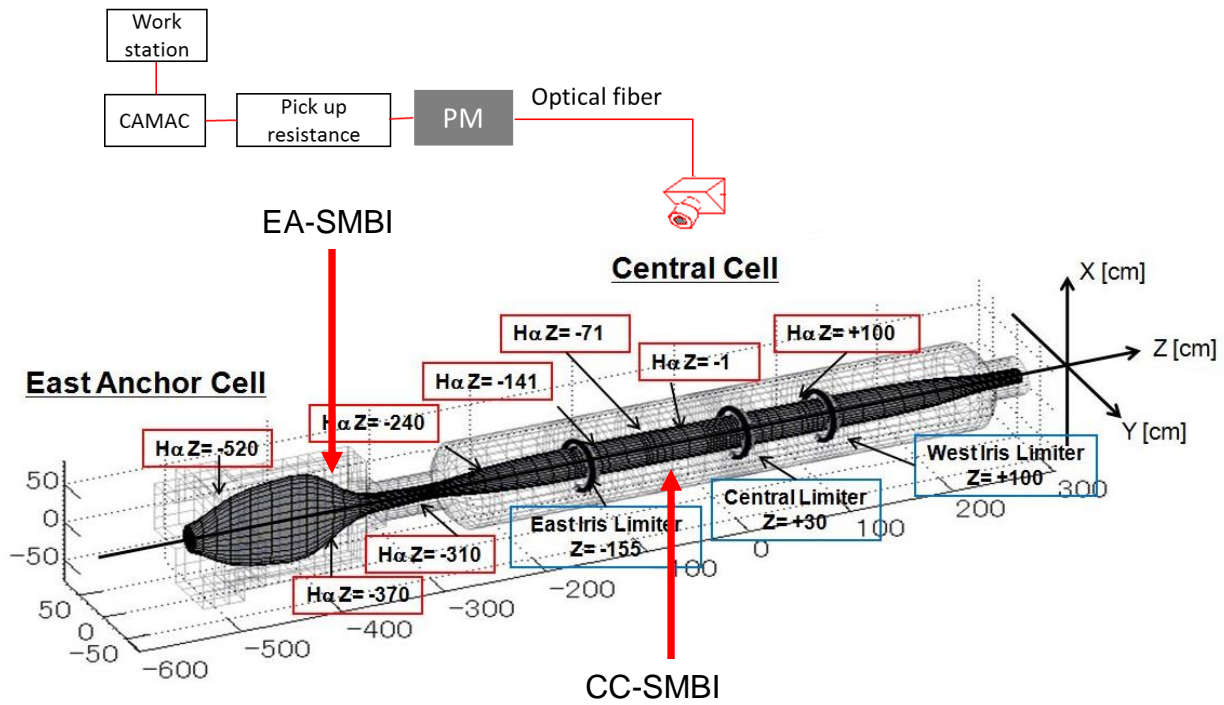

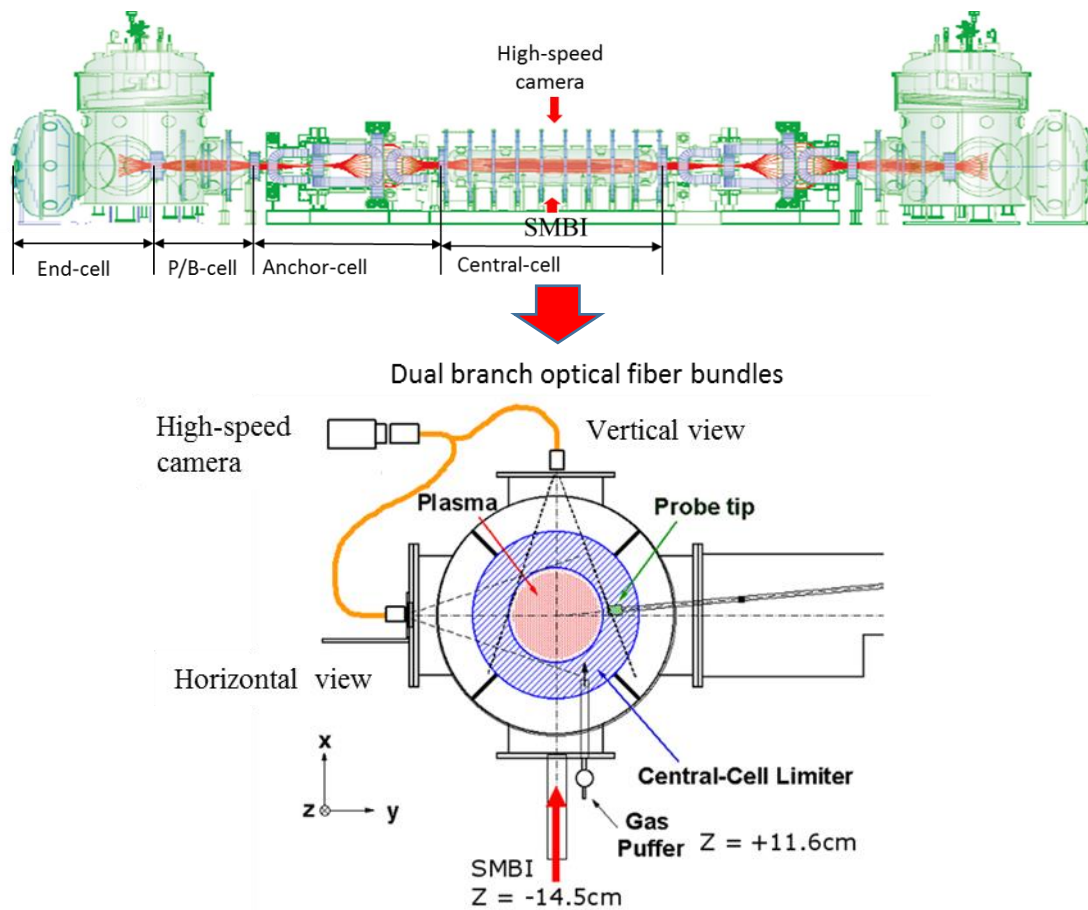Fig. 2.6 Location of Hα detector in GAMMA 10.

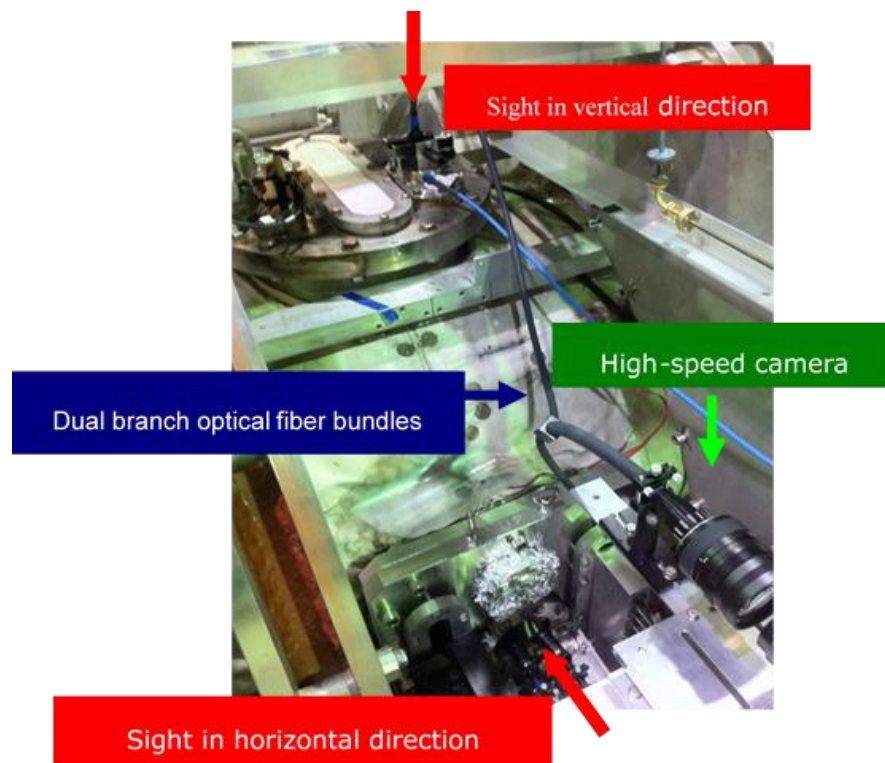Fig. 2.7 Cross-sectional view of the central-cell, locations of SMBI system and high-speed camera.

Fig. 2.8 Photograph of high-speed camera installed in the central-cell.

Chapter 3
Analytical Method for Neutral Particle Transport

In this chapter, the neutral transport analysis methods are explained in detail. Analysis method is to couple the measured Balmer-line intensity with the simulation result by the Monte-Carlo method in this study. In consideration of the plasma parameter of the GAMMA 10 plasma, Collisional-Radiative (CR) model is employed in order to carry out this analysis. Information of spatial profile of emissivity is determined by using a Monte-Carlo simulation.

3.1 Hα Measurements

In order to study behavior of neutral particles in plasma confinement devices, the diagnostics of Balmer-line emission is a useful method [54]. We employed Hα line emission whose quantum number is n=3-2, and wavelength is 656.3 nm, because this line is in visible light, easy to measure and the model for the plasma spectroscopy has been developed for estimating the neutral hydrogen density. Balmer-line is visible light, which enable us to easily measure the emission. The plasma is assumed to be optically thin enough. In consideration of the plasma parameter region of the GAMMA 10 plasma, this assumption is appropriate. The Hα emission $E\ (r)$ can be written by the next relation with the number density of level 3, $n_3(r)$ and transition probability A_{32} as follows,

$$E\ (r) = \frac{hc}{\lambda_{H_\alpha}}\ n_3(r)A_{32}\ , \qquad\qquad (3.1)$$

where the h, c and λ_{H_α} are the Planck's constant, the speed of light and the wavelength of the Hα line, respectively. If $E\ (r)$ is measured, $n_3(r)$ can be obtained. Finally, the neutral density which is the number density of the ground state can be estimated by using the CR model [58-60].

In order to measure the axial distribution of the neutral particles, five Hα detectors are installed at z =+100 cm, -1 cm, -71 cm, -141 cm -240 cm, -305 cm and -370 cm. The axial distribution of Hα is affected by the interior components. Therefore the detector at z = +100 cm monitors the Hα emission near the west iris limiter, the detectors at z = -1 cm and -71 cm monitor that near the midplane in the central cell, the detector at z = -141 cm monitors that near the east iris limiter, the detector at z = -305 cm monitors that near the gas puffer which is mainly used for particle supply.

3.2 Collisional-Radiative (CR) Model

In this model, the number density of level p is determined from the electron temperature, density and number density of the ground state. The processes of radiative-transition, recombination, electron impact excitation, ionization and three-body collisional recombination are considered as atomic processes. The schematic drawing of the atomic processes used in the CR model is shown in Fig. 3.1. The number density of level p of the atomic hydrogen n_p is represented by the following rate equation.

$$\frac{d}{dt}n_p = -n_p n_e S(T_e, p) - n_p n_e \sum_{p \neq q} X(T_e, p, q)$$
$$- n_p \sum_{q<p} A_{pq} + n_e \sum_{p \neq q} n_q X(T_e, p, q) \qquad (3.2)$$
$$+ n_i n_e \alpha(T_e, p) + n_e \sum_{q>p} n_q A_{pq} + n_i n_e \beta(T_e, p).$$

where n_i, n_e and T_e are the hydrogen ion density, electron density and electron temperature, respectively. $S(T_e, p)$, $X(T_e, p, q)$, $\alpha(T_e, p)$ and $\beta(T_e, p)$ are the rate coefficients for the ionization, collisional excitation, three-body recombination and radiative-recombination, respectively. In a level of $p \gg 1$, where a local thermal equilibrium can be assumed, the relationship among n_i, n_e and n_p can be rewritten by the following Saha's ionization equation.

$$n_p = n_p^E, \qquad (3.3)$$

$$\frac{n_i n_e}{n_p^E} = \frac{2g_+}{g_p} \frac{(2\pi m_e \kappa T_e)^{3/2}}{h^8} exp(\frac{E_p}{\kappa T_e}), \qquad (3.4)$$

where g_+, g_p, κ and m_e, are the multiplicity of ion and level p, Boltzmann constant and mass of electron, respectively. Moreover, by solving the simultaneous equations of $p - 1$ unknowns, n_p can be rewritten as follows,

$$n_p = R_0(p)n_i n_e + R_1(p)n_H n_e. \qquad (3.5)$$

The first and the second terms of the right hand side of the above equation are the recombination process between ion and electron with rate coefficient $R_0(p)$ and excitation of hydrogen atom with $R_1(p)$, respectively. n_H is the hydrogen atom density. Since the electron temperature in GAMMA 10 is obtained to be higher than 10 eV, the recombination term in Eq. 3.5 can be neglected. Moreover, the effect of the direct dissociative excitation reaction of hydrogen molecule is not negligible when the density of hydrogen atoms in excited levels is estimated, since the electron density in GAMMA 10 is lower than $10^{19} m^{-3}$ [54]. Eq. 3.5 is, then, rewritten by using a rate coefficient for the

dissociative excitation of hydrogen molecule $R_2(p)$ and its density n_{H_2} as,

$$n_p = R_1(p)n_H n_e + R_2(p)n_{H_2} n_e. \tag{3.6}$$

If the plasma density and the electron temperature are obtained, R_1 and R_2 are derived from this equation. In order to determine the neutral hydrogen density, Monte-Carlo simulation is carried out.
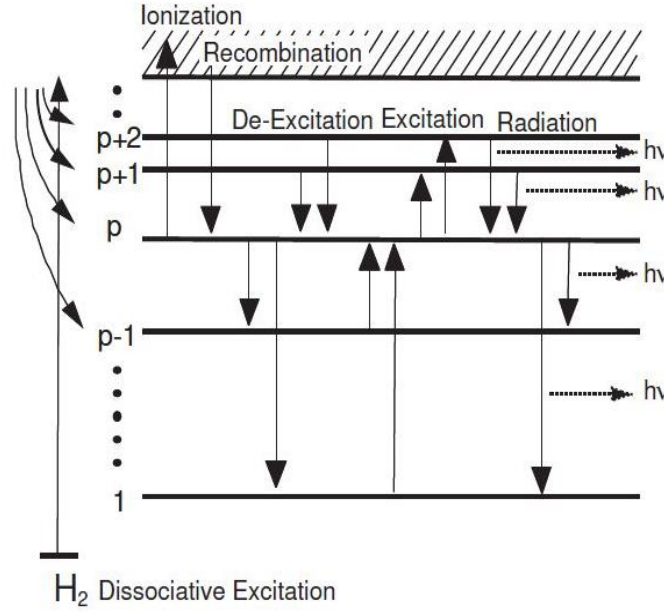

Fig. 3.1 Schematic view of CR-model process.

3.3 Numerical Simulation Code (DEGAS)

The DEGAS code is a numerical calculation code that simulates the transport of multiple species neutral particles in three-dimensional plasma by using a Monte-Carlo technique [37, 38]. The numerical process follows on Boltzmann equation. This code was originally developed at the Princeton Plasma Physics Laboratory (PPPL) and has widely been used for the estimation of the profiles of the density and temperature of the neutral particles in many magnetic confinement devices.

A neutral particle transport code (DEGAS) is used for analysis of neutral particle density in the GAMMA 10 plasma. The version 35 of DEGAS code (DEGAS35) was firstly developed for neutral transport simulation in the central cell [61]. The meshes for this code are constructed as a 2-dimensional axis. Mesh configurations and plasma parameters in the cell of simulation space are assumed to be axi-symmetric. The schematic image of mesh for DEGAS35 is shown in Fig. 3.2. However the DEGAS code has been developed for the simulation of the high plasma density region such as tokamak plasmas. Therefore, it was reported that the density profile of neutral hydrogen atoms calculated by the DEGAS code was significantly different from the experimental results in the case that the plasma density was less than $10^{19} \mathrm{m}^{-3}$ [54]. This discrepancy was attributable to the

production of hydrogen atoms at excited levels by the direct-dissociation of hydrogen molecules upon electron impact. The effect of dissociative-excitation reactions of neutral hydrogen molecules are additionally included so as to calculate low density plasma in the plasma edge region for applying the DEGAS code to the GAMMA 10 plasma [61, 62]. In order to investigate the neutral transport due to the non-axisymmetric structure of the wall geometry and plasma parameter, and the non-uniform distribution of the neutral sources, the version 63 of DEGAS code (DEGAS63) was successfully utilized [61-70]. The schematic image of mesh for DEGAS35 is shown in Fig. 3.3. The DEGAS code has been applied in 3-D simulation of neutral transport in a part of central-cell and anchor-cell. 3-D simulation mesh model are expanded in order to evaluate the amount of the generated particles in the central cell. Finally, the fully 3-dimentional mesh model in a whole area of central cell and a part of anchor cell is accomplished. The intensity of Balmer-line emission is determined with use of the calculated neutral density and CR-model, and then is normalized with the experimental results obtained by the Hα detector. If Balmer-line emission is absolutely calibrated the absolute value of the neutral density is also obtained from this method. In the measurement of the detector, only the information of the Hα emission near the sight line of the detector is obtained. By the combination of Hα emission measurement and Mote-Carlo simulation, the ionization rate of the neutral particles and the hydrogen recycling is determined in the whole area of central cell. From the analysis, the radial and axial profile of the neutral density is estimated. It is noted that such analysis method become a more useful method according to the recent development of computer performance. In the Monte-Carlo technique, the Boltzmann equation describing the neutral particle distribution is time-independently solved. This indicates that the static-condition is assumed for the Monte-Carlo calculation. The physical process and the computational technique on DEGAS are shown in Appendix B.
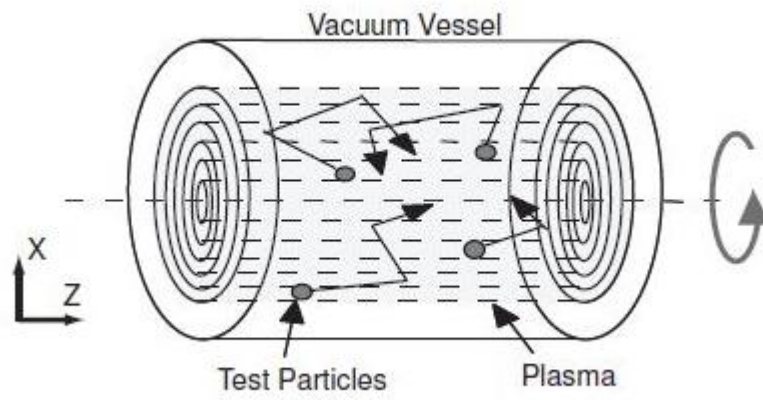
Fig. 3.2 Schematic view of plasma mesh model used in DEGAS ver. 35 simulation.
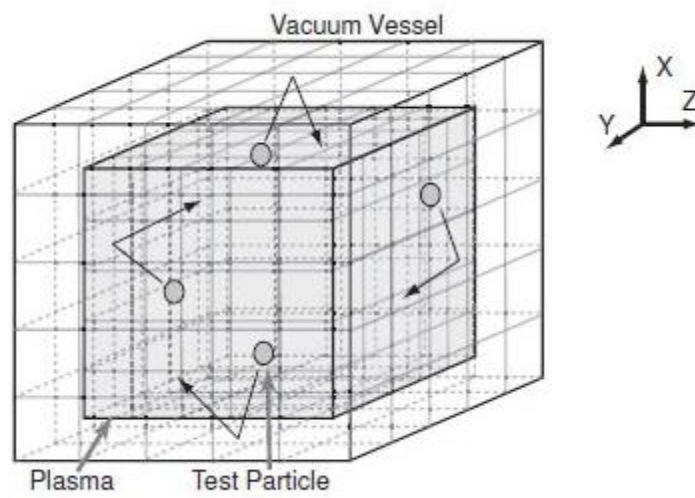

Fig. 3.3 Schematic view of plasma mesh model used in DEGAS ver. 63 simulation.

Chapter 4
Experimental Results and Discussion

In this chapter, the plasma parameters behavior is investigated during SMBI injection with ECRH and ICRF heated plasma in the central-cell and east-anchor transition region.

4.1 SMBI Experiments with ICRF Heated Plasma in the Central-cell

In GAMMA 10, SMBI with Laval nozzle experiment is carried out in the central-ell. At first SMBI experiment is performed only ICRF heated plasma. Figure 4.1(a) shows the schematic view of SMBI system in the central-cell. The magnetic shielding vessel for the SMBI valve is modified prior to the experiment by additional shielding in order to prevent the effect of the external magnetic field during the operation of the valve. SMBI system with Laval nozzle is installed at $Z = -14.5$ cm at the bottom of central-cell mid-plane. The conventional gas puffing fueling system is also located at $Z = +11.6$ cm in the central-cell. The gas puffing experiment is also carried out on only ICRF heated plasma in order to compare with SMBI experimental results.
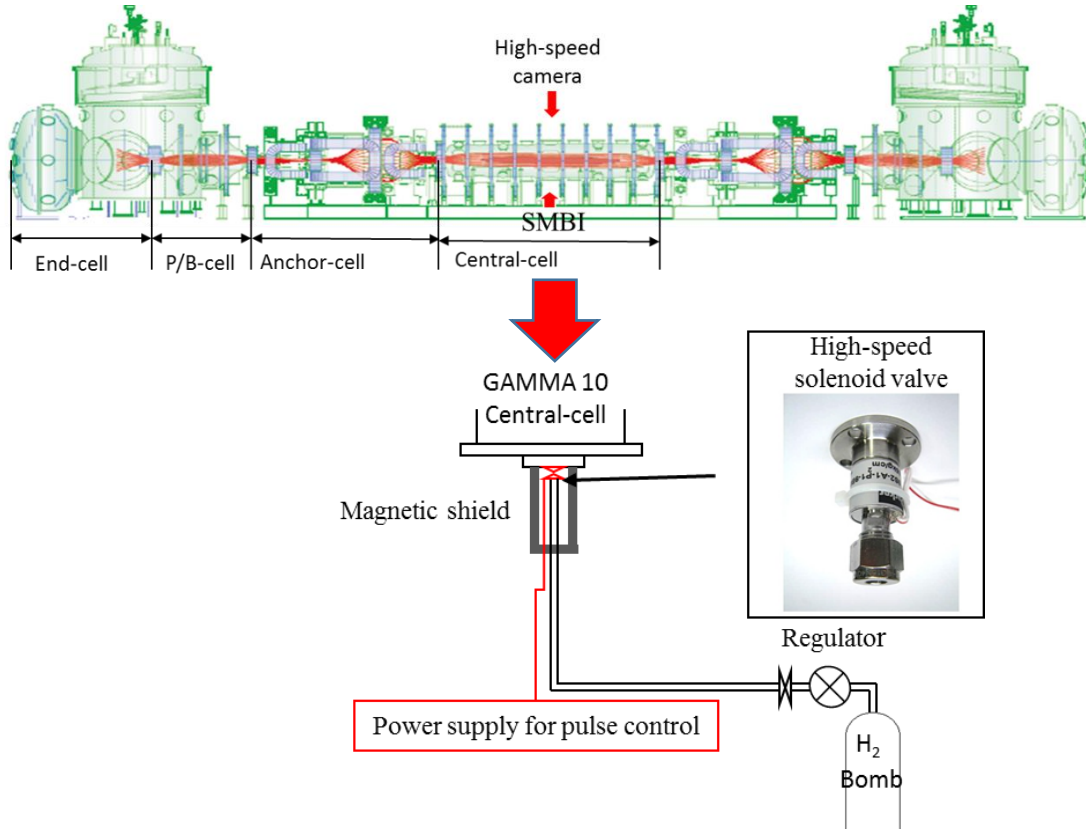

Fig. 4.1 (a) Schematic view of SMBI system and location in the GAMMA 10.

4.1.1 Time evolution of plasma parameter during SMBI

In the experiment, SMBI pulses were injected using the Laval nozzle into the typical plasmas heated by only ICRF (RF1 and RF2). The SMBI pulse is injected at 150 ms and the pulse width is 0.5 ms. The response of the gas fueling by SMBI to the electron density (NLcc) and diamagnetism (DMcc) is measured by microwave interferometer system and diamagnetic loop, respectively. Figure 4.2 shows the time evolution of line-integrated electron density and diamagnetism during SMBI on ICRF heated plasma at a plenum pressure of 2.0 MPa. From this figure we observe that the electron line-density is increased during the SMBI. However, the diamagnetism is decreased. The reduction of stored energy after SMBI may be occurred due to the charge-exchange (CX) loss of the hot ions produced by ICRF.

The axial distribution of Hα-line emission intensity is measured by Hα-detectors at $Z = -1$ cm, -71 cm and -141 cm. Figure 4.3 shows Hα emission intensity during SMBI at the plenum pressure of 2.0 MPa. From this figure a steep peak emission intensity is observed at $Z = -1$ cm, since the Hα detector at $Z = -1$ cm is close to the SMBI injection port at $Z = -14.5$ cm. The response of Hα emission intensity during SMBI is decreased with the increasing distance from the SMBI injection position as shown in Fig 4.3(b) and Fig. 4.3(c). It implies that the particles injected at this pressure become localized and therefore low emission intensity is observed at $Z = -71$ cm and $Z-141$ cm.
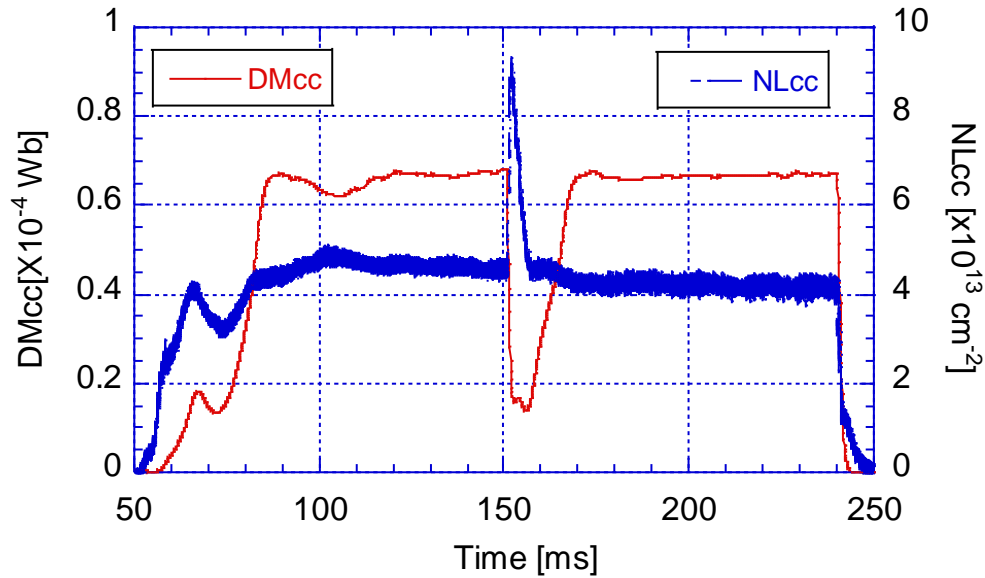

Fig. 4.2 Time evolution of line-integrated electron density (Nlcc) and diamagnetism (DMcc) during SMBI in the central-cell.
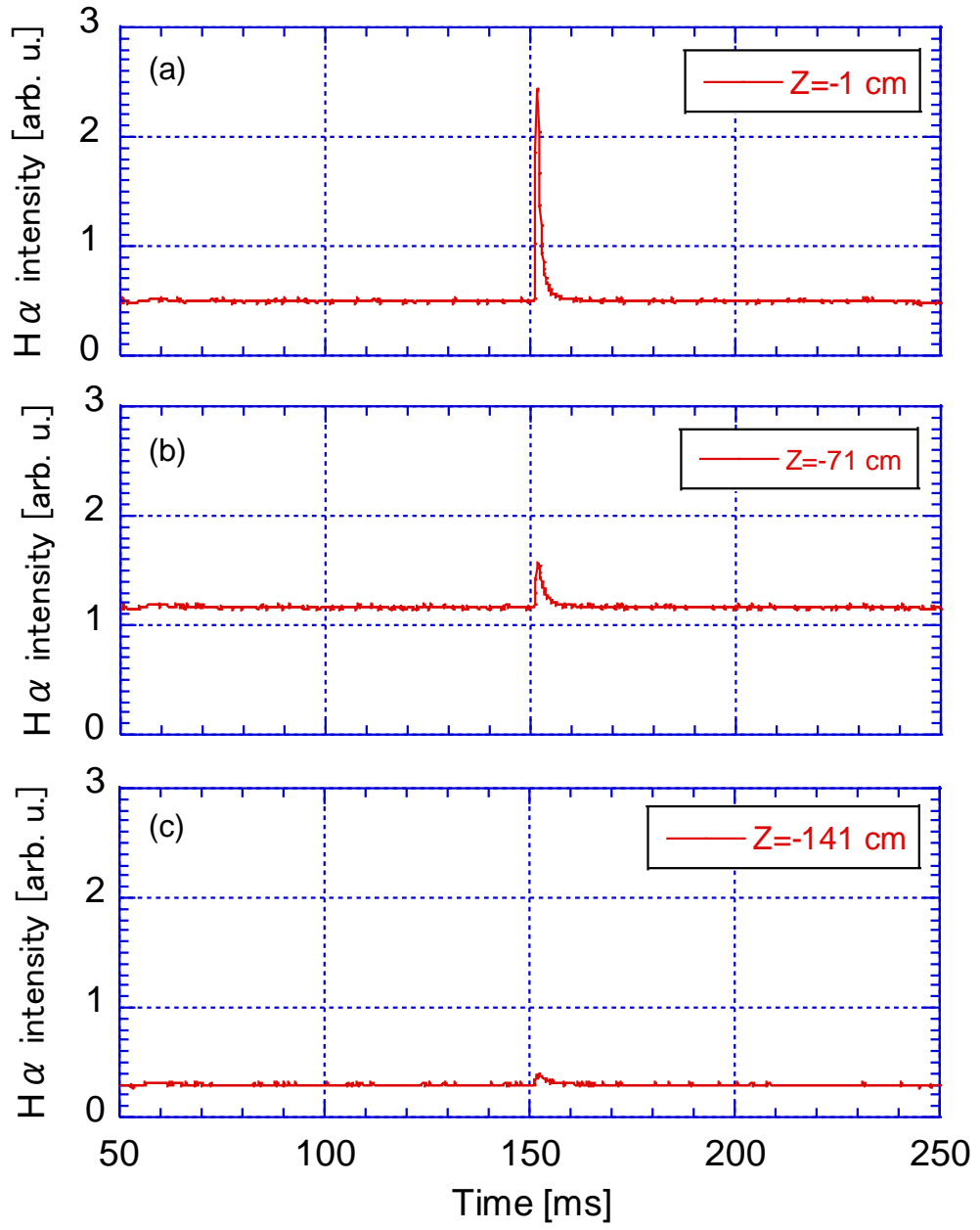
Fig. 4.3 Time evolution of Hα-line emission intensity during SMBI measured by axially located Hα-detectors (a) Z=-1 cm, (b) Z=-71 cm, and (c) Z=-141 cm.

4.1.2 Plenum pressure dependence of plasma parameter during SMBI

The time evolution of the plasma parameter at different plenum pressure is shown in Fig. 4.4. From this Fig. 4.4(a) it is observed that at a plenum pressure of 0.3 MPa, the electron line-density is slightly increased. However, the diamagnetism is decreased much more about 70%. Before injecting SMBI, the value of DMcc almost 6.8×10^{-5} Wb. During SMBI at a plenum pressure of 0.3 MPa it reduces to 1.9×10^{-5} Wb. The diamagnetism is considered to be reduced due to CX loss of hot ions. The electron line-density increases with increase of plenum pressure as shown in Fig. 4.4(a) to Fig. 4.4(f). However, when we increase the plenum pressure up to 2.0 MPa the bottom value of DMcc is not remarkably changed.

Figure 4.5 shows the time evolution of Hα-line emission at Z = -1 cm for different SMBI plenum pressure. From this figure it is observed that Hα emission intensity increases with the increase of SMBI plenum pressure. It is also observed that the peak value of Hα emission intensity during SMBI shifts early with increase of plenum pressure. It implies that the response of SMBI become very quick at high plenum pressure. The plenum pressure dependence of the change in electron line-density ($\Delta Nlcc$) is shown in Fig. 4.6(a). From this figure it is observed that the variation of change in electron line-density increases linearly with plenum pressure. Figure 4.6(b) shows the plenum pressure dependence of change in Hα emission intensity ($\Delta I_{H\alpha}$). From this figure it also observed that the variation of change in Hα emission intensity increases linearly with increase of plenum pressure. Since both $\Delta NLcc$ and $\Delta I_{H\alpha}$ increase with the SMBI plenum pressure, the particle fueling rate by SMBI is proportional to the plenum pressure in this operation range.
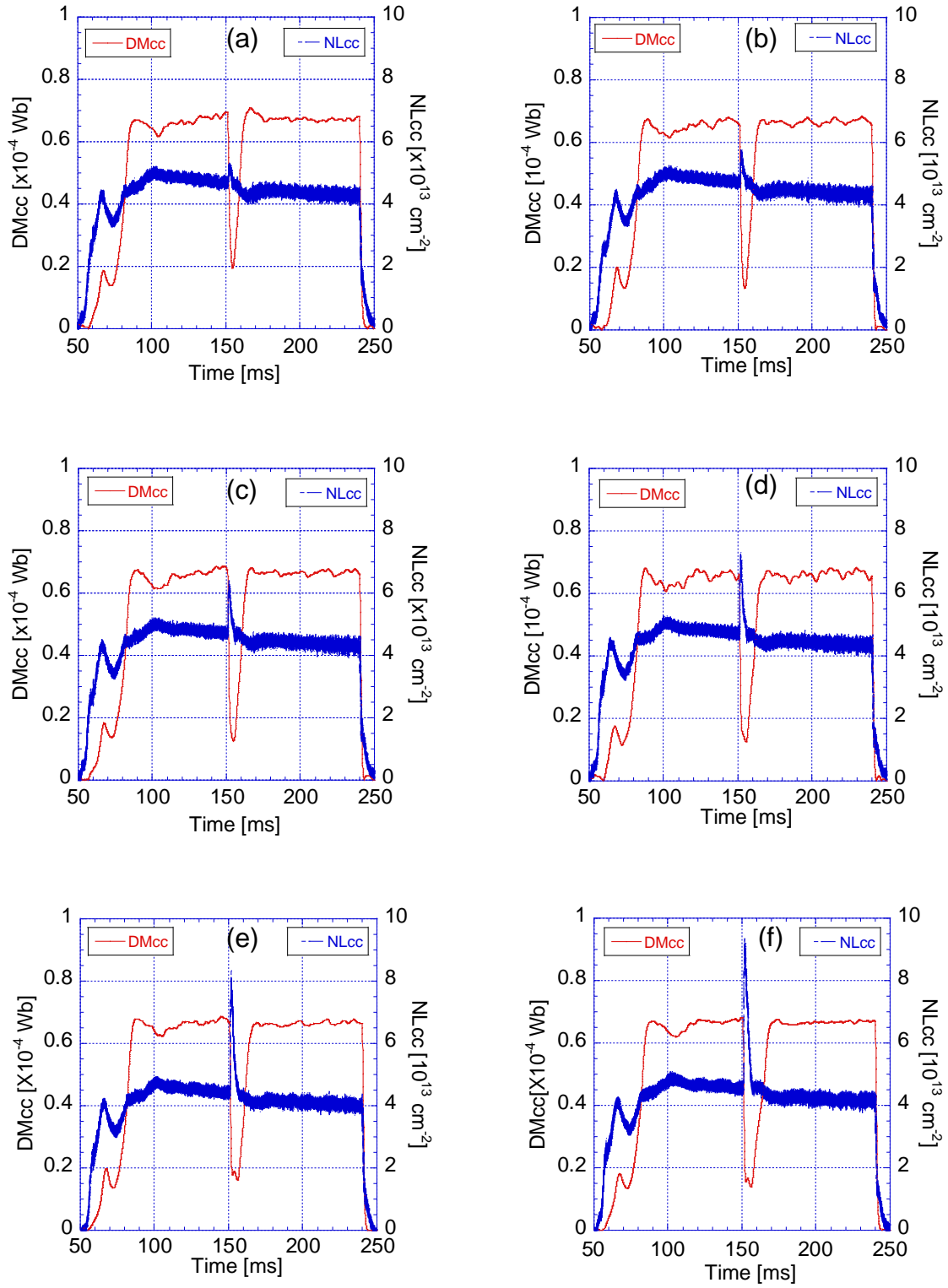
Fig. 4.4 Time evolution of Plasma parameter during SMBI at different plenum pressure;
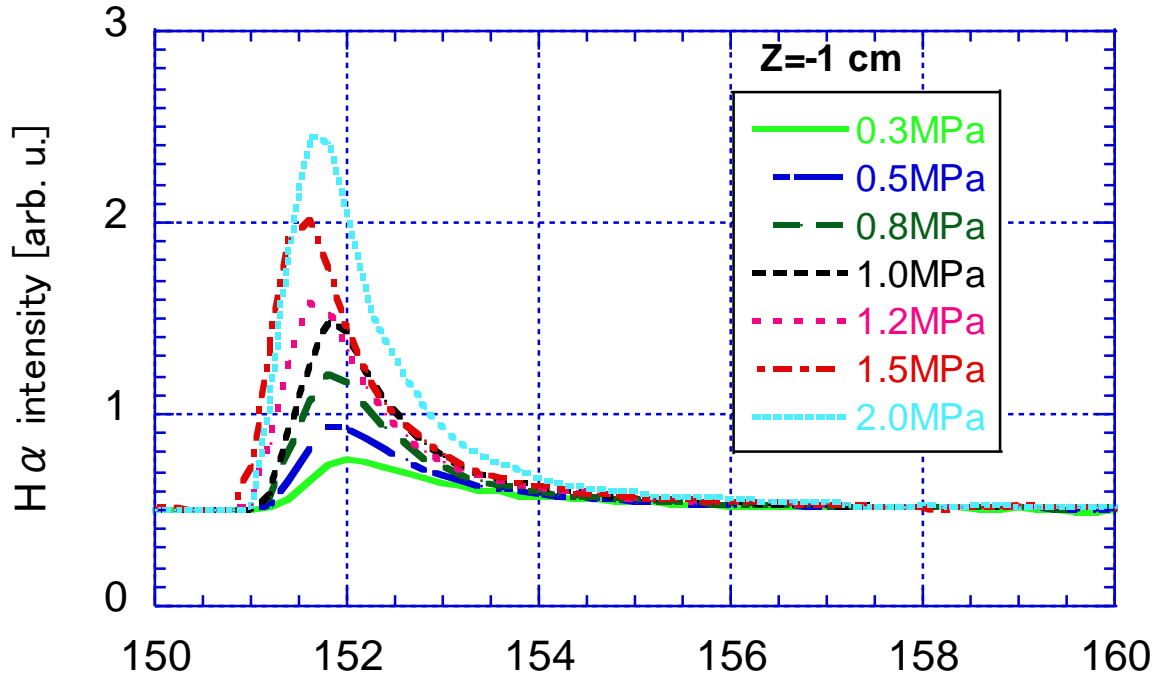(a) 0.3 MPa, (b) 0.5 MPa, (c) 0.8 MPa, (d) 1.0 MPa, (e) 1.5 MPa and (f) 2.0 MPa

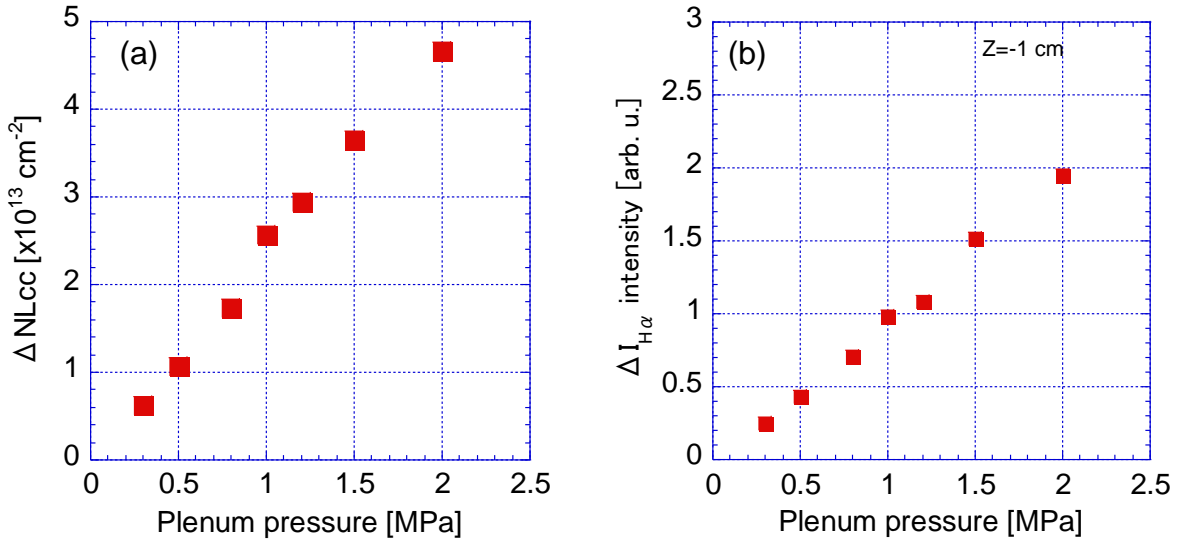Fig. 4.5 Time evolution of Hα-line emission intensity during SMBI for different plenum pressure.

Fig. 4.6 SMBI plenum pressure dependence of (a) change in electron line-density and (b) change in Hα emission intensity during SMBI.

4.1.3 Neutral transport analysis during SMBI by using high-speed camera

The 2-D images captured by the high-speed camera of visible emission during SMBI with Laval nozzle from the plasma is shown in Fig. 4.7. From this figure we observe that it takes 1.2 ms to achieve the peak intensity after the SMBI. However, it took 2 ms in the case of SMBI with straight nozzle [10]. It indicates that SMBI with Laval nozzle is faster than that with straight nozzle. Figure 4.8 shows the peak emission intensity of 2-D image during SMBI. The left side of Fig. 4.8 shows 2-D images of the intensity emitted in the horizontal direction and the right side shows the intensity emitted in the vertical direction. The 2-D image viewing from the horizontal port is more widely spread than the diameter of the nozzle exit (24 mm). The injected molecules are dissociated with Frank-Condon energy (~ 3eV) much higher than molecular velocity (thermal energy). It is considered that the dissociated hydrogen atoms spread out as isotropic and resultant emission profile becomes much wider than that of original beam. In order to evaluate the axial profile of neutral transport, the directivity of the molecular beam injected by SMBI is investigated based on vertical direction image. We also studied the distribution of emission intensity at the broken line on the right side of Fig. 4.8. Figure 4.9 shows the distribution of emission intensity at the broken line as obtained from the 2-D vertical image. We used the full width at half maximum (FWHM) of the distribution of the emission intensity at the broken line on the right side of Fig. 4.8 as an index of the axial neutral transport. As the intensity profile generally does not change as the intensity increase, the best signal-to-noise ratio is obtained at the peak emission intensity. Using the Laval nozzle we analyzed the FWHM for each SMBI plenum pressure and is compared with the FWHM obtained by straight nozzle and only valve cases. All experimental conditions except for the SMBI plenum pressure were fixed.

Figure 4.10 shows the relationship between FWHM and the plenum pressure for only valve, straight nozzle and Laval nozzle cases. It is found for the first time that the remarkable reduction of FWHM is achieved using Laval nozzle. The FWHM value is also lower than compared with straight nozzle. Moreover, in all plenum pressure FWHM is lower than the diameter of plasma in the case with Laval nozzle. Accordingly, the effect of the Laval nozzle reduces the spreading of the neutral particle from SMBI in the peripheral region. In the low plenum pressure range (< 1.0 MPa), the FWHM value decreases with increasing the SMBI plenum pressure in both straight nozzle and Laval nozzle cases. This behavior indicates that the dispersion of molecular beam is varied with the plenum pressure, which shows that the flow of molecular beam is thought to be not supersonic in low plenum pressure. The FWHM decrease with increasing plenum pressure up to 1.0MPa and then the flow become supersonic. In higher plenum pressure range (1.0 MPa or higher) FWHM is become constant, which implies that the optimization of molecular beam attained. Note that in the case of straight and Laval nozzle, the minimum FWHM value are about 70% and 55% of the plasma diameter, respectively. This means that the Laval nozzle has more capability to improve the directivity of the particle fueling by SMBI.
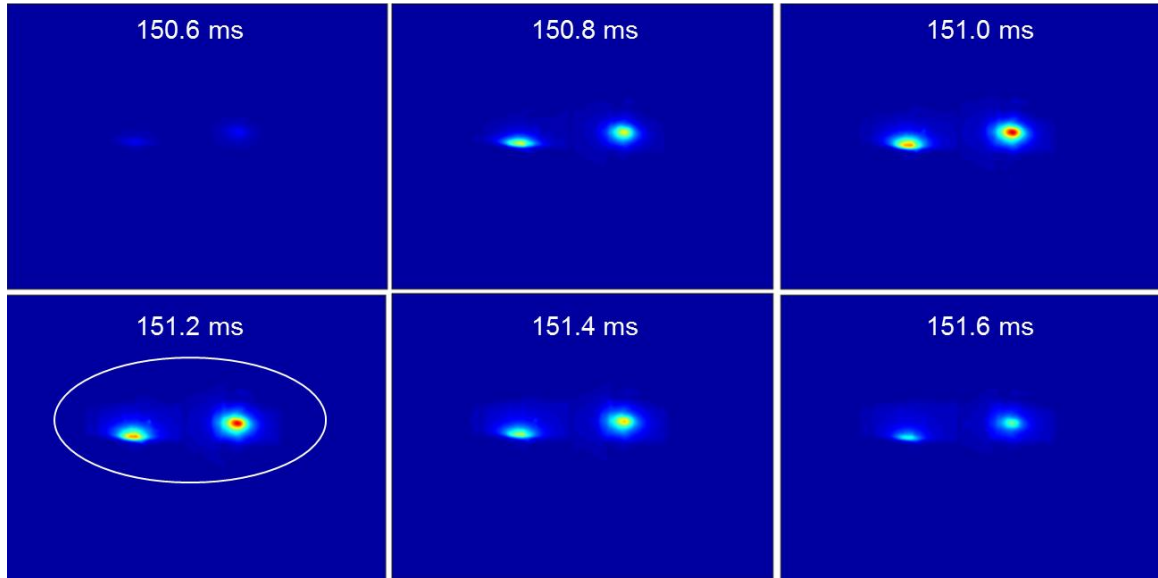
Fig. 4.7 Time behavior of 2-D image during SMBI captured by high-speed camera.
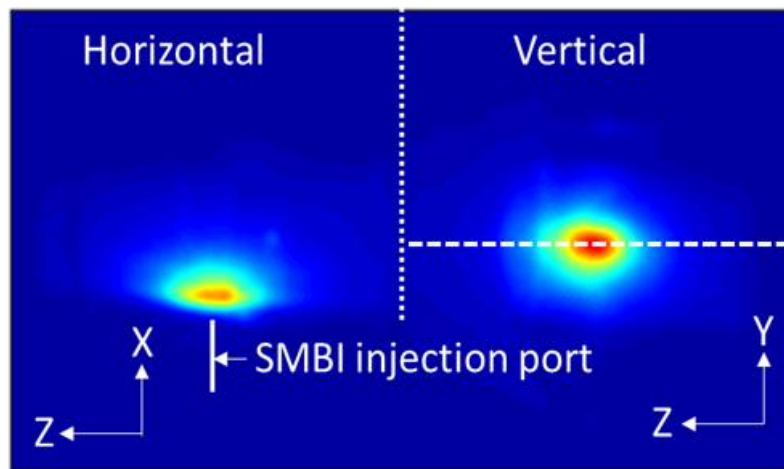

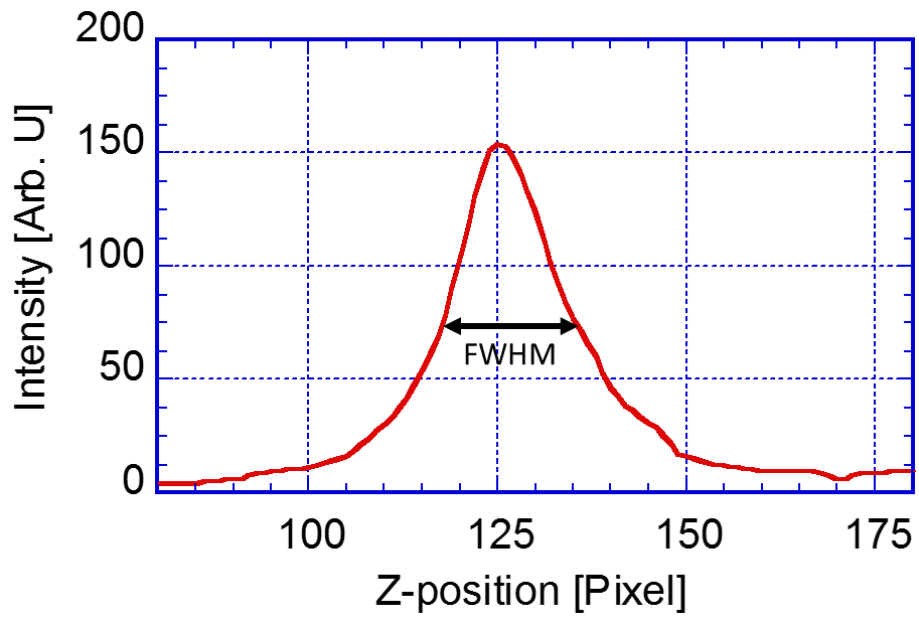Fig. 4.8 The peak emission intensity of 2-D image during SMBI.

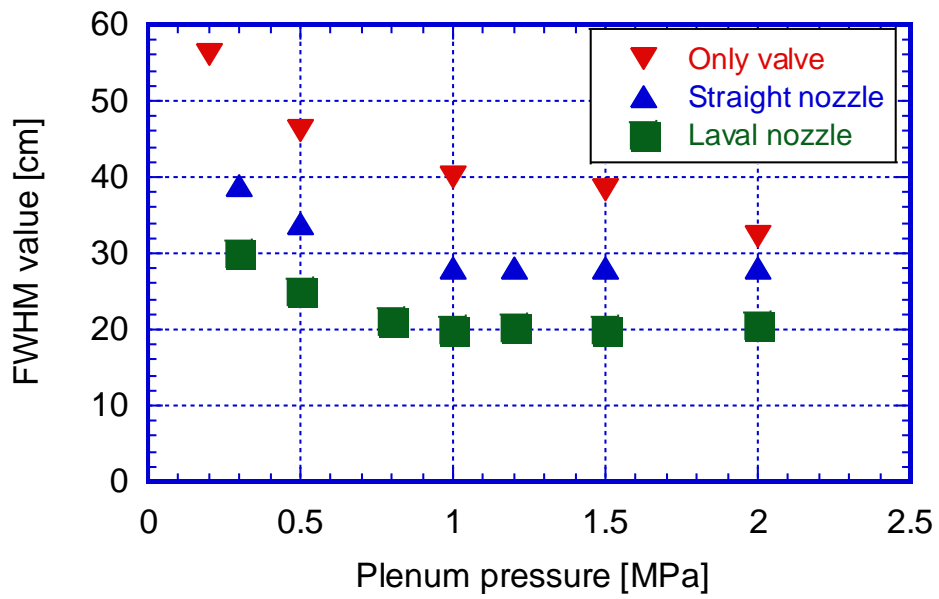Fig. 4.9 The distribution of vertical emission intensity.

Fig. 4.10 Variation of FWHM value with SMBI plenum pressure for two cases.

4.1.4 Comparison between SMBI and Gas Puff

   The results of comparison between conventional gas puffing (GP) and SMBI are shown in Figs. 4.11(a) and 4.11(b). GP and SMBI are injected at 120 ms and 170 ms, durations are 4 ms and 1 ms, and pressures are 66.66 kPa and 1.0 MPa, respectively. Increased portion of NLcc is higher during SMBI than that of gas puffing. On the other hand, the peak value of the Hα intensity measured from the same detector at Z = -1 cm, is lower and the time width become narrower during SMBI than gas puffing. It qualitatively shows that SMBI with Laval nozzle is more efficient than gas puffing.

   In GAMMA 10, multi-channel microwave interferometer has been installed at the central-cell to observe the radial profile of line-integrated density at core and peripheral region. The radial profile of electron density for fueling and before fueling as shown in Fig. 4.12. Both fueling system are effective at core and peripheral region. It is found that the electron density is slightly higher in the case of SMBI than gas puffing.
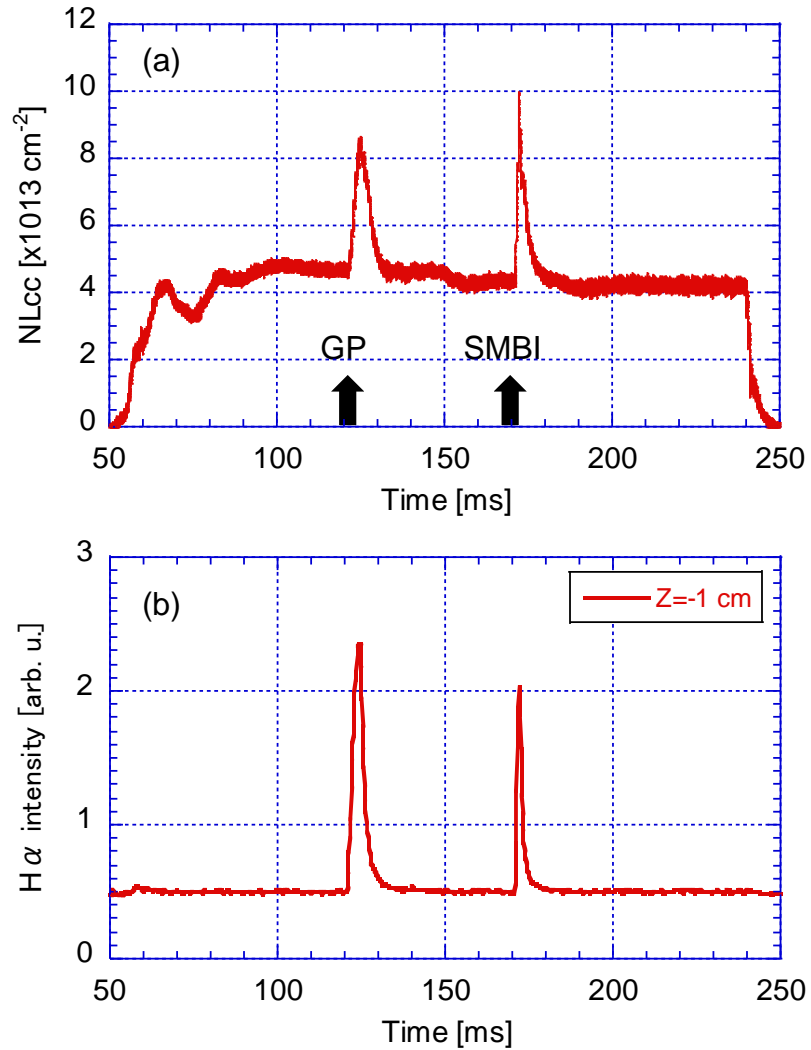
Fig. 4.11 Time evolution of (a) electron line-density and (b)Hα-line emission
intensity, during GP from 120-124 ms and SMBI from at 170-171 ms.
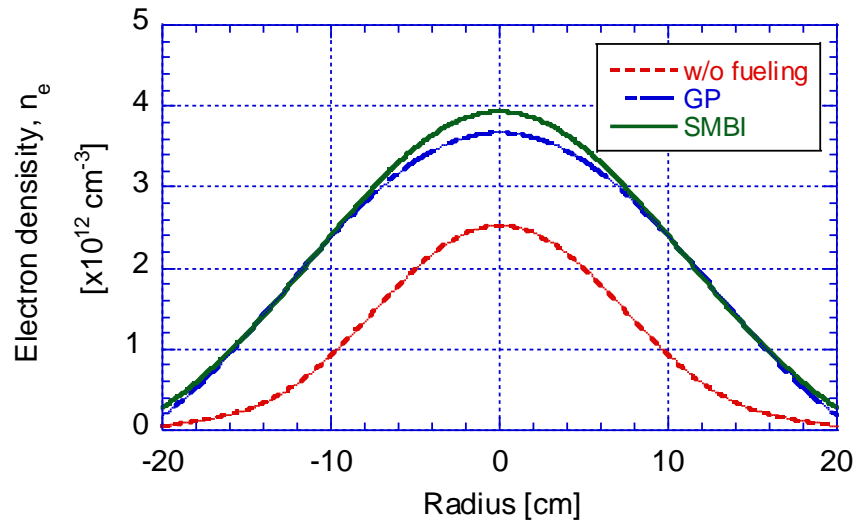
Fig. 4.12 Radial profile of electron density during GP and SMBI.

4.2 SMBI Experiments with ECRH and ICRF Heated Plasma in the Central-cell

In order to evaluate the effect of additional plasma heating, SMBI pulses were injected into the typical plasmas heated by ICRF and ECRH [71]. To plug the axially escaping plasma, the axially confining potential is produced by P/B-ECRH in the plug/barrier-cells. P-ECRH produces the positive potential which is called plug potential in order to plug the axial escaping ion and B-ECRH produces the negative potential which is called thermal-barrier potential in order to plug the axial escaping electron [33]. P/B-ECRH injected at 145 ms and duration is 20 ms and SMBI is injected in the period of the ECRH injection. P-ECRH and B-ECRH power are 150 kW and 100 kW, respectively. SMBI pulse is injected at 150 ms and the pulse width is 0.5 ms.

4.2.1 Time evolution of plasma parameter during SMBI

The time evolution of line-integrated electron density and diamagnetism during SMBI with ECRH at a plenum pressure of 2.0 MPa is shown in Fig.4.13. From this figure it is observed that the electron line-density is increased during SMBI with P/B-ECRH. The electron line-density during SMBI with ECRH as shown in Fig. 4.13 is higher compared to without P/B-ECRH as shown in Fig. 4.2. It implies that the particles are confined due to potential formation by P/B-ECRH injection in the plug/barrier region. However, the reduction of diamagnetism during SMBI is almost same.

The axial distribution of Hα-line emission intensity in the central-cell during SMBI with ECRH is measured by Hα-detectors at Z = -1 cm, -71 cm and -141 cm. Figure 4.14 shows Hα emission intensity during SMBI at the plenum pressure of 2.0 MPa. From this figure it is observed that at same plenum pressure, the Hα emission intensity is higher during SMBI with ECRH compared to without ECRH as shown in Fig. 4.3. It may be due to the enhancement ionization during SMBI with ECRH injection.
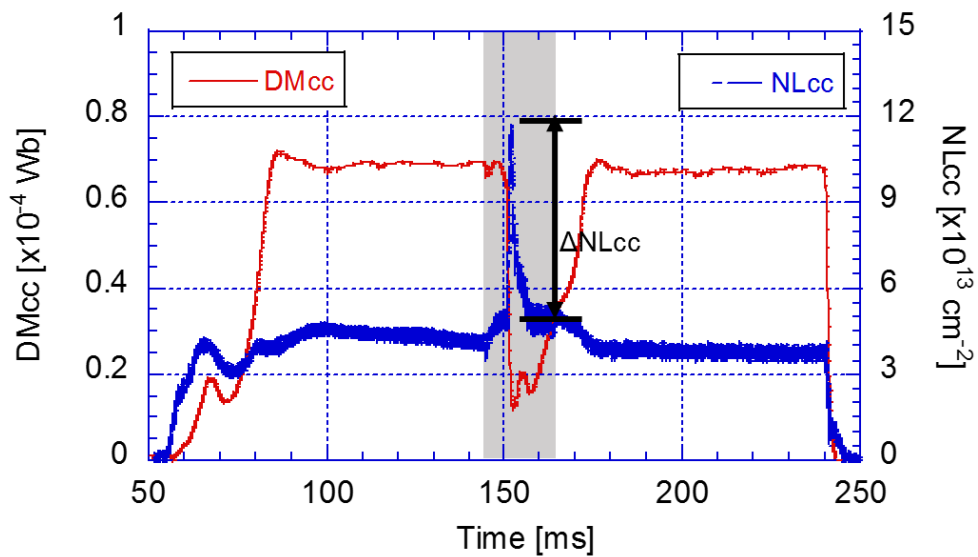

Fig. 4.13 Time evolution of line-integrated electron density (Nlcc) and diamagnetism (DMcc) during SMBI with ECRH in the central-cell.
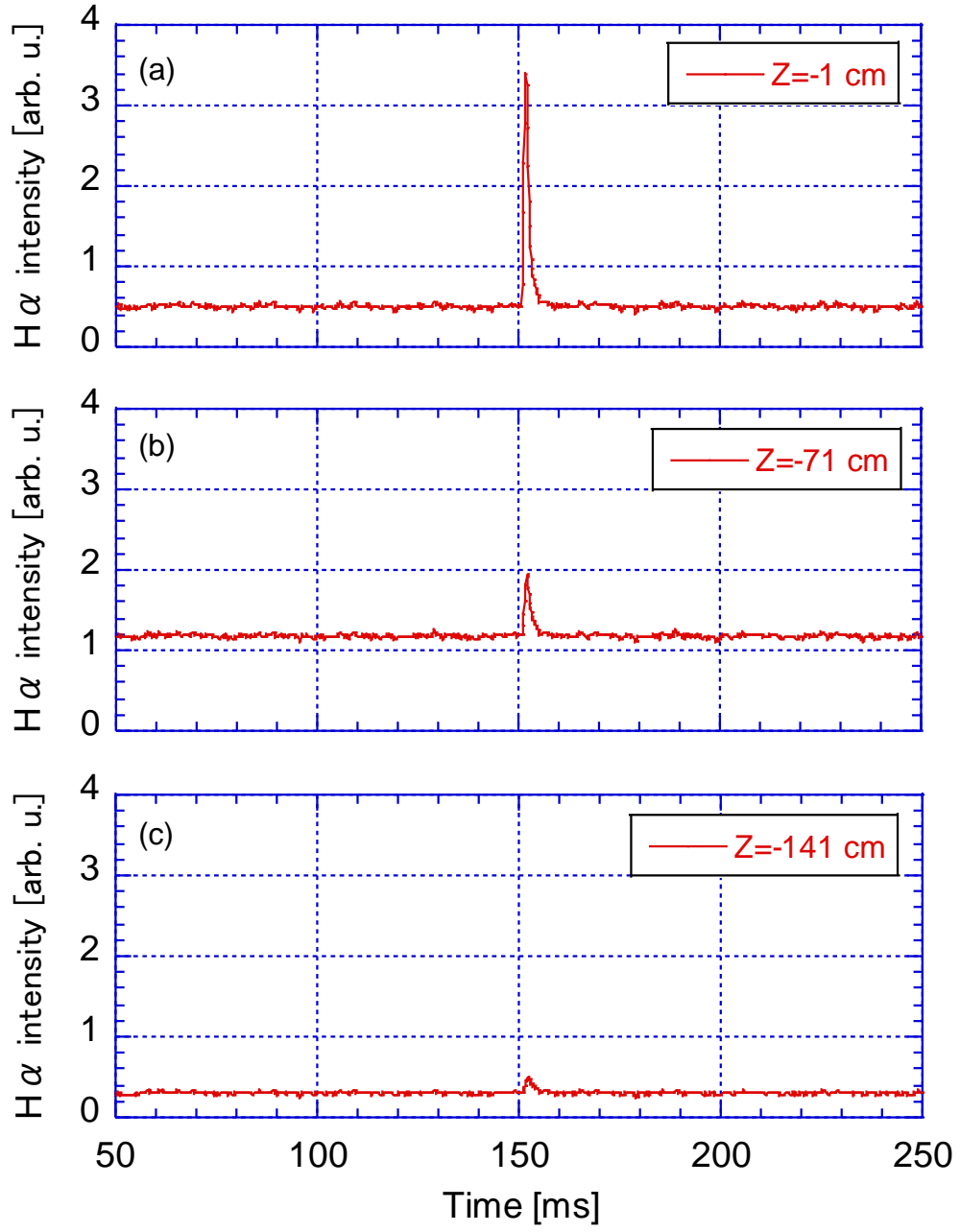
Fig. 4.14 Time evolution of Hα-line emission intensity during SMBI with ECRH measured by axially located Hα-detectors (a) Z=-1 cm, (b) Z=-71 cm, and (c) Z=-141 cm.

4.2.2 Plenum pressure dependence of plasma parameter during SMBI

Figure 4.15 shows the time evolution of Hα-line emission intensity measured by Hα-detector at Z = -1 cm for different plenum pressure during SMBI with ECRH injection. From this figure it is observed that Hα emission intensity increases with the increase of plenum pressure. The peak value of Hα emission intensity during SMBI shifts early with increase of plenum pressure as like as only ICRF heated plasma.

The change in electron line-density and Hα emission intensity during SMBI with ECRH and only ICRF heated plasma as shown in Fig. 4.16. From Fig. 4.16(a) it is observed that in both the ICRF and ICRF/ ECRH plasmas, the change in the electron line-density in the central-cell increases almost linearly to the plenum pressure. From the previous results, it has been obtained that the directivity of the SMBI gas improved when the plenum pressure was up to 1.0 MPa and it saturated more than 1.0 MPa. In such the case, the change in the electron line-density is almost proportional to the change in the Hα intensity whose sightline observes the SMBI gas. These results indicate that the particle source produced by SMBI has a contribution to the increase in the electron density without saturation under the present experimental condition. Note that, in all plenum pressure cases, the change in electron line density is higher in the case of ECRH injection than the ICRF heated plasma. It implies that the particles are confined in the central-cell due to P/B-ECRH injection in the plug/barrier region. The comparison of the change in $I_{Hα}$ between ICRF and ICRF/ECRH plasma is shown in Fig. 4.16(b). It shows that Hα emission intensity is high compared with without ECRH case. It implies that Hα emission intensity is increased due to the enhancement of ionization during ECRH injection.

The radial profile of electron temperature is measured at 152 ms by Thomson scattering system as shown in Fig. 4.17(a). From this figure it is observed that the electron temperature increases during ECRH injection. Therefore, higher Hα emission intensity is observed due to enhancement of ionization during SMBI. Figure 4.17(b) shows the radial profile of electron density during SMBI and ECRH with SMBI cases. The electron density is higher in the case of ECRH injection. It implies that the particles are confined due to potential formation by the ECRH injection in the plug/barrier-cells.

Figure 4.18 shows the comparison of the bottom value of DMcc between ICRF and ICRF/ECRH heated plasma. In low SMBI plenum pressure DMcc is slightly improved in the case of ECRH injection. However, at high SMBI plenum pressure DMcc is not improved.
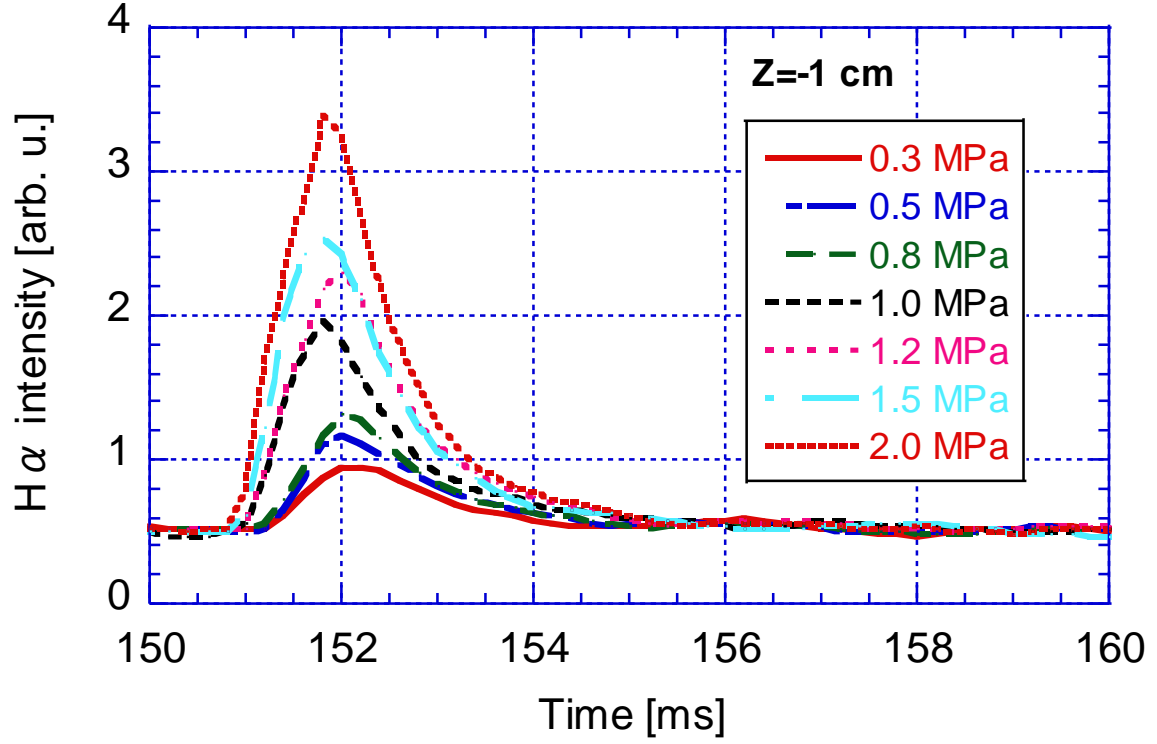
Fig. 4.15 Time evolution of Hα-line emission intensity at Z = -1 cm during SMBI with ECRH for different plenum pressure.
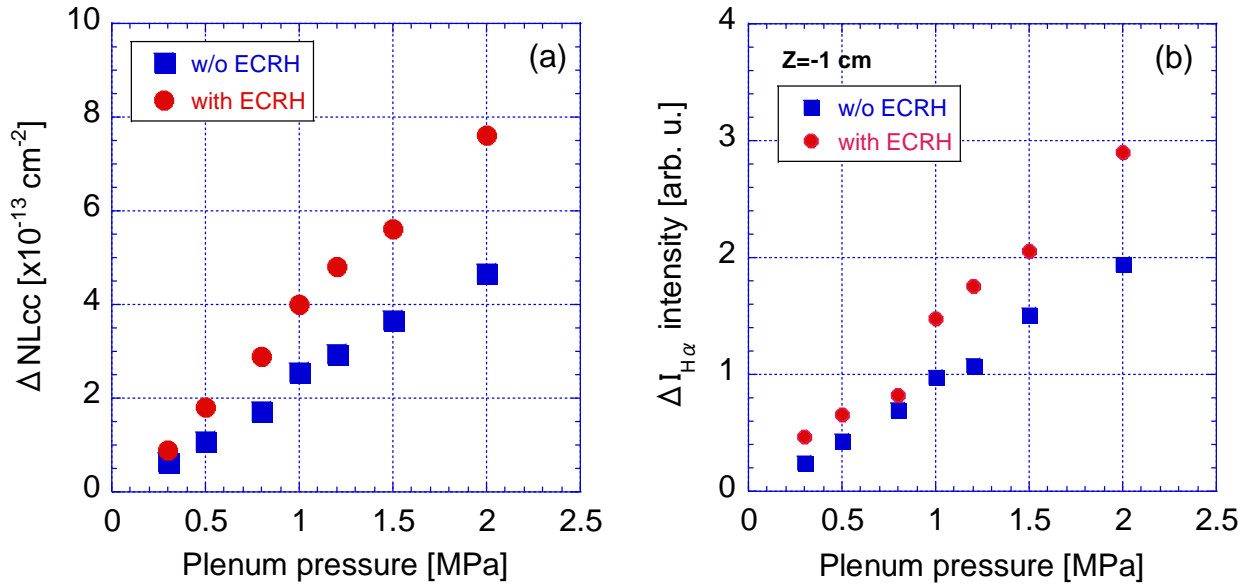

Fig. 4.16 SMBI plenum pressure dependence of (a) change in electron line-density and (b) change in Hα emission intensity during SMBI with ECRH.
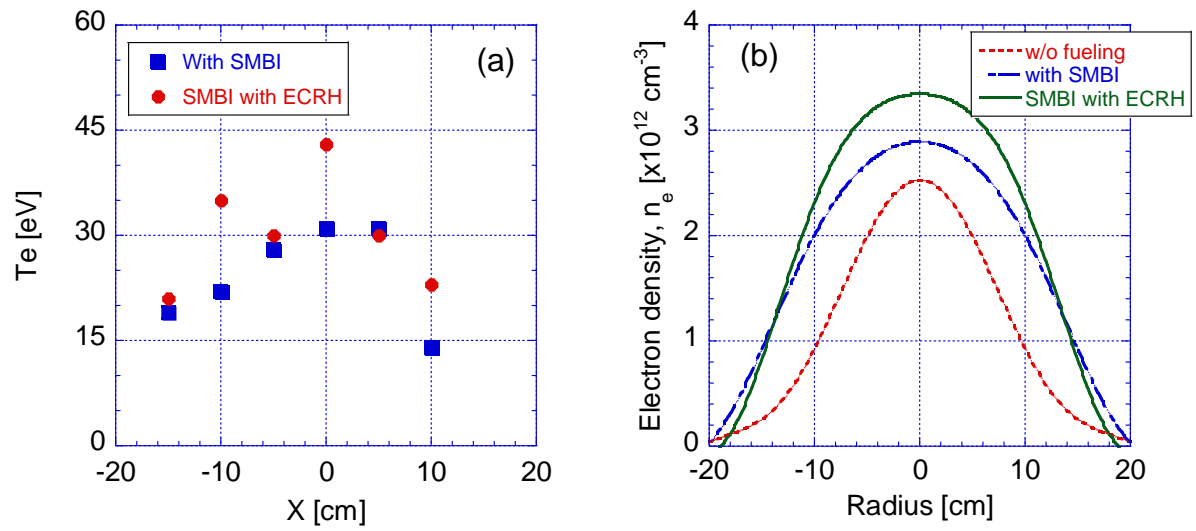
Fig. 4.17 Comparison of radial profile of (a) electron temperature and (b) electron density during SMBI with ECRH and without ECRH.
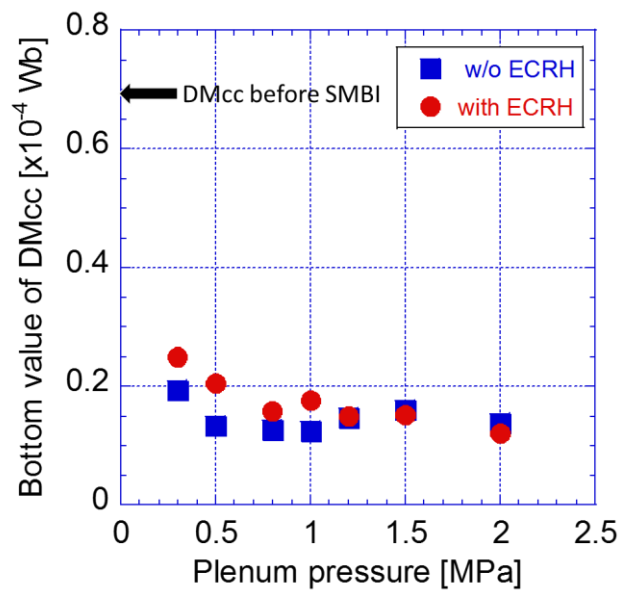

Fig. 4.18 Comparison of SMBI plenum pressure dependence of the bottom value of diamagnetism.

4.2.3 Neutral transport analysis during SMBI by using high-speed camera

The 2-D images captured by the high-speed camera of visible emission during SMBI with ECRH from the plasma is shown in Fig. 4.19. It shows the peak emission intensity of 2-D image during SMBI with ECRH. The left side of Fig. 4.19 shows the intensity emitted in the vertical direction and the right side shows the intensity emitted in the horizontal direction. To evaluate the axial profile of neutral transport, the directivity of the molecular beam injected by SMBI with ECRH is investigated based on vertical direction image. Figure 4.20 shows the axial distribution of emission intensity during SMBI with only ICRF heated plasma and with additional ECRH plasma as obtained from the 2-D vertical image. We used the full width at half maximum (FWHM) of the distribution of the emission intensity at the broken line on the left side of Fig. 4.19. The value is examined as an index of the axial neutral transport as we evaluated only ICRF heated plasmas. Figure 4.21 shows the relationship between FWHM and the plenum pressure for ECRH and without ECRH cases. From this figure it is found that the FWHM value is reduced in the case of ECRH injection. The electron temperature is increased due to ECRH injection. It implies that the FWHM value is reduced due to enhancement of ionization during ECRH.
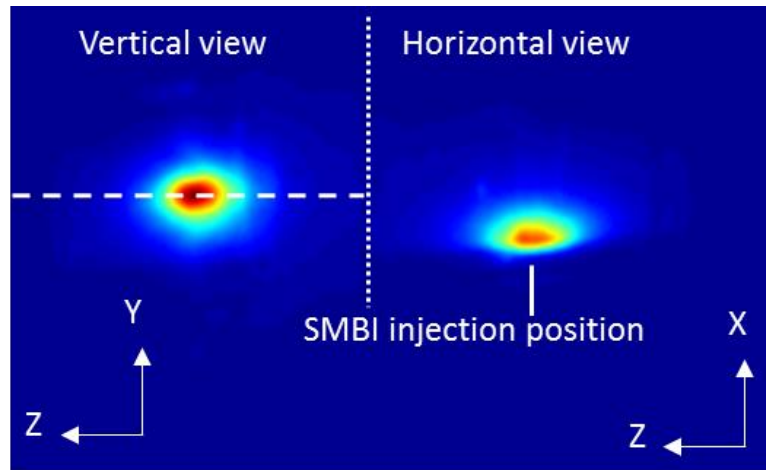

Fig. 4.19 The peak emission intensity of 2-D image during SMBI with ECRH captured by high-speed camera.
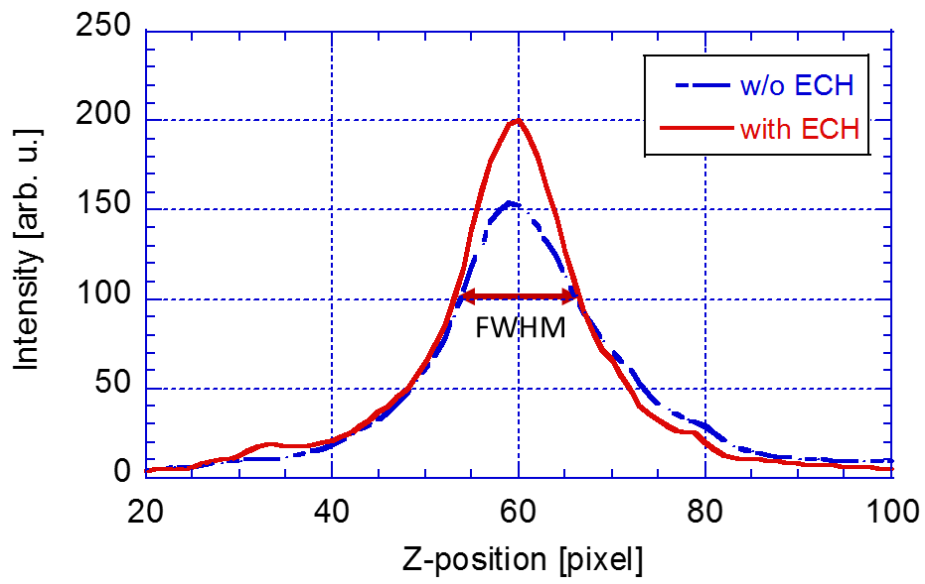
Fig. 4.20 The distribution of vertical emission intensity during SMBI with ECRH and without ECRH.
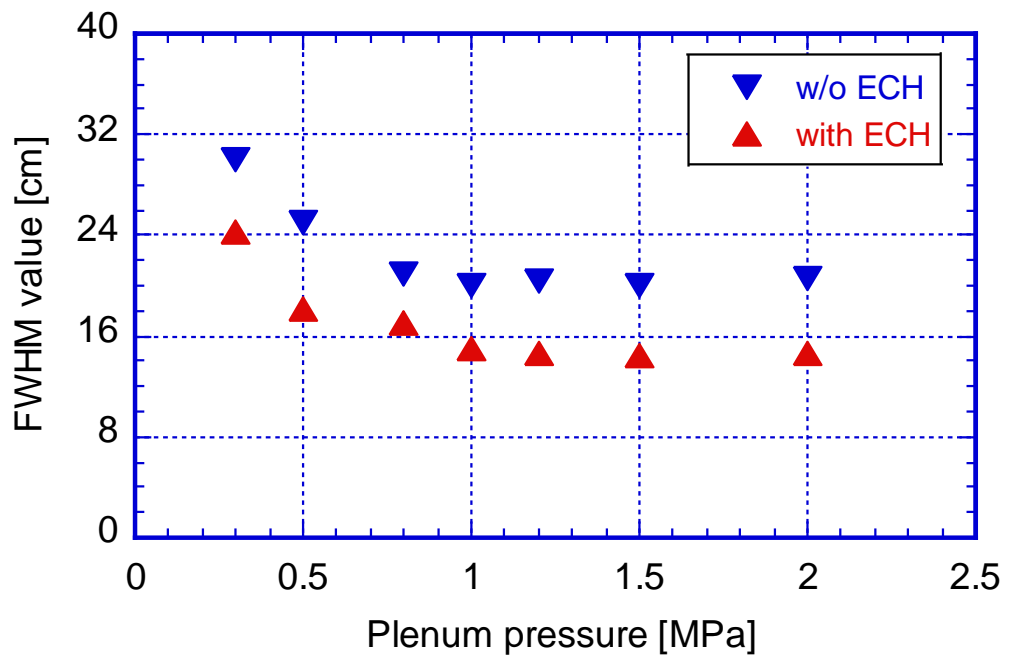

Fig. 4.21 Comparison of FWHM value with plenum pressure for two cases during SMBI.

4.2.4 End-loss ion current measurement during SMBI by ELIEA

In order to measure the end-loss ion current, ELIEA is installed on both end sides in GAMMA 10. The end loss ion current is measured by using sweep repeller voltage. Figure 4.22 shows that the end-loss ion current is increased during SMBI at plenum pressure 1.0 MPa. SMBI inputs a large amount of gas within a short period of time. The plasma density increases in the central-cell due to the increase in the amount of gas. Therefore, more ion flow into the end-cells, and the ion current density is increased during SMBI. In order to plug the particles escaped from central-cell to end-cells, P/B-ECRH is applied to ICRF heated plasma. P/B-ECRH is injected at 145 ms and duration is 20 ms. SMBI is injected in the period of the ECRH injection at 150 ms and the pulse width is 0.5 ms. P-ECRH and B-ECRH power are 150 kW and 100 kW, respectively. Therefore, the end-loss ion current is reduced and increases the plasma density in the central-cell during SMBI at plenum pressure of 1.0 MPa as shown in figure 4.23(a). It might be due to the formation of plug and thermal barrier potential by P/B-ECRH in the plug/barrier region. However, SMBI at high plenum pressure (~2.0 MPa), the P/B-ECRH could not suppressed the end loss current remarkably as shown in Figs. 4.23(b) and (c). It may be speculated that the plug/barrier potential is reduced due to a large amount of gas injected at high plenum pressure in the central-cell.
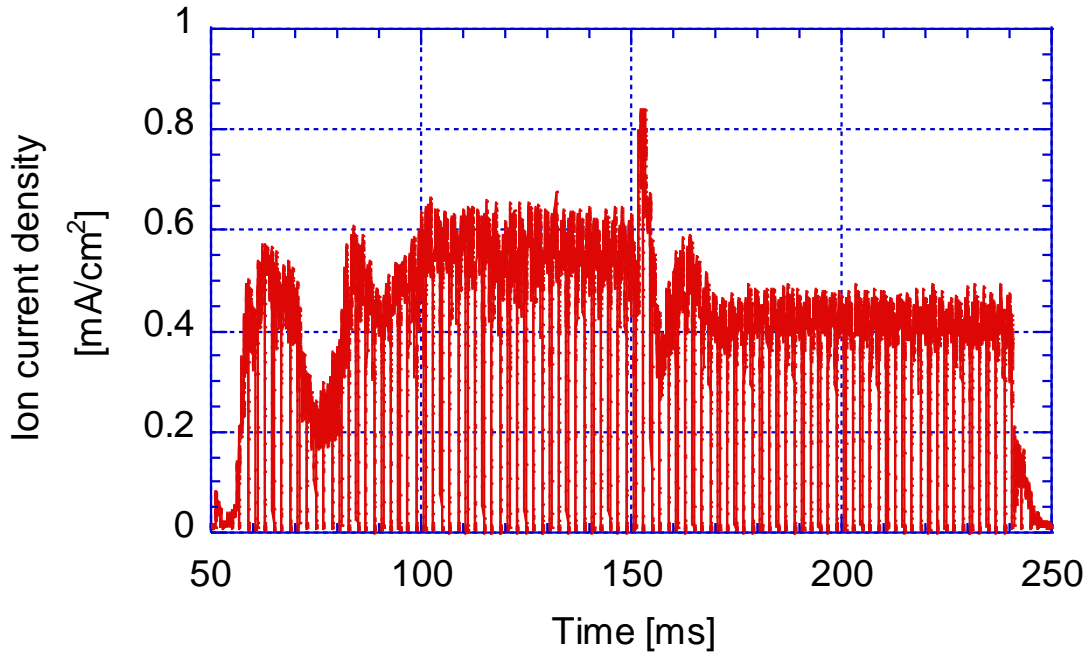

Fig. 4.22 Time evolution of end-loss ion current during SMBI with ICRF heated plasma.
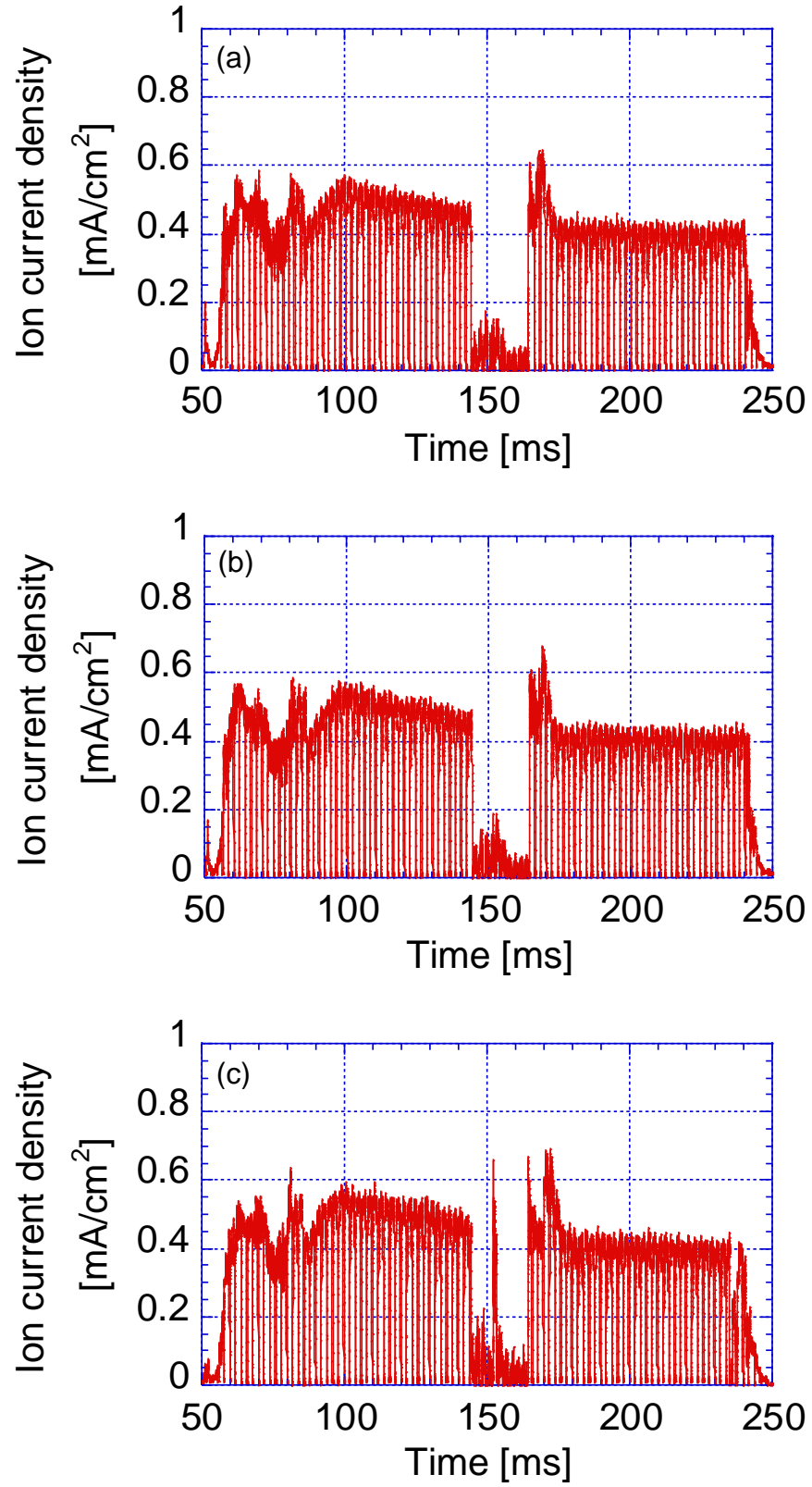
Fig. 4.23 Time evolution of end-loss ion current during SMBI with fixed P/B- ECRH for different plenum pressure, (a) 1.0 MPa, (b) 1.5 MPa, and (c) 2.0 MPa.

4.3 SMBI Experiments in the East Anchor Inner-transition Region

So far, SMBI experiment has been performed in central-cell mid-plane in GAMMA 10. In GAMMA 10, hot ion mode plasma is produced in the central-cell. The line density is increased during SMBI, however the stored energy is reduced due to the charge-exchange energy loss. Recently, the SMBI experiments is performed another region in GAMMA 10 in order to improve the plasma parameter. In order to do this experiments, we searched ports at different region in GAMMA 10. The only available port was at the top of east anchor inner-transition region of east anchor-cell. Therefore, SMBI system with new type short Laval nozzle is installed at top of the east anchor transition region in order to know the fueling characteristics and the plasma behavior is investigated by varying plenum pressure and SMBI pulse with. The photograph and location of EA-SMBI system is shown in Fig. 4.24.
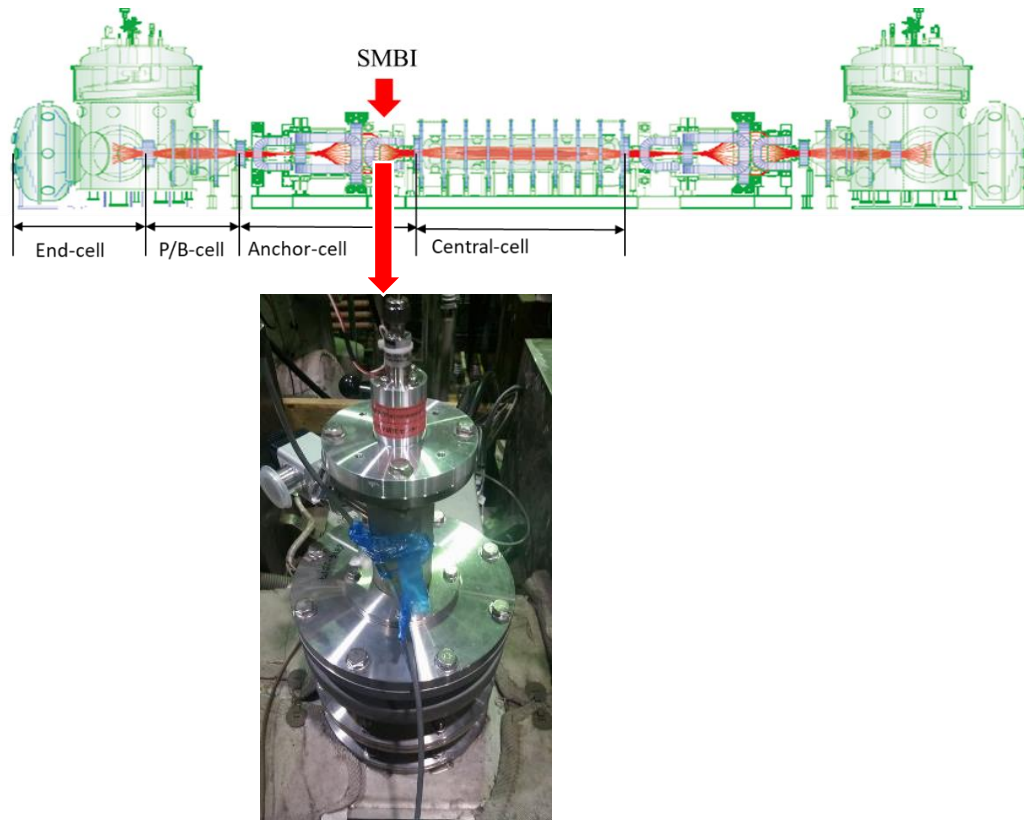

Fig. 4.24 Photograph of EA-SMBI system installed in east-anchor inner-transition region of east-anchor cell.

4.3.1 EA-SMBI plenum pressure dependence of plasma parameter

In the EA-SMBI experiments, SMBI pulses is injected using new Laval nozzle into the typical plasmas heated by only ICRF (RF1 and RF2). The SMBI pulse is injected at 150 ms and pulse width is 0.5 ms. In order to know the plenum pressure dependence of plasma behavior with fixed pluse width 05 ms, the plenum pressure is varied from 0.3 MPa to 2.0 MPa. By changing the SMBI plenum pressure, the response of the gas fueling by SMBI to the electron density (NLcc) and diamagnetism (DMcc) is investigated by microwave interferometer and diamagnetic loop in the central-cell.

Figure 4.25(a) shows the time evolution of line-integrated electron density and diamagnetism during SMBI at a plenum pressure of 2.0 MPa. From this figure it is observed that the electron line-density is increased after the SMBI and the diamagnetism is decreased. However, the diamagnetism is slightly improved compared with CC-SMBI as shown in Fig. 4.2 at the pressure of 2.0 MPa and 0.5 ms pulse width. Before injecting SMBI, the value of DMcc almost 4.8×10^{-5} Wb. During SMBI at the plenum pressure of 0.3 MPa it reduces to 4.4×10^{-5} Wb. However, when we increase the plenum pressure up to 2.0 MPa the bottom value of DMcc is gradually reduced. The response of EA-SMBI to electron line-density in the east anchor and west anchor is shown in Figs. 4.25(b) and Fig. 4.25(c), respectively. From these figure we observe that the electron line-density in the east anchor-cell is higher compared to electron line-density in the west anchor-cell. Since EA-SMBI is installed in the east anchor inner-transition region, the electron line-density is high in the east anchor-cell.

The Hα-line emission intensity is measured by the Hα-detector at Z = -370 cm, where the EA-SMBI is installed. Figure 4.26 shows the time evolution of Hα-line emission intensity at Z = -370 cm during SMBI for different plenum pressure. The SMBI pulse width is 0.5 ms and it is fixed for all plenum pressure case. From Fig. 4.26 it is observed that the emission intensity increases with the increase of the plenum pressure. Since the number of injected particles increase with the increase of plenum pressure, the Hα emission intensity is increased at high plenum pressure. The plenum pressure is varied from 0.3 MPa to 2.0 MPa. The peak value of Hα intensity shifts early according to the increase of the plenum pressure. However, the peak value of CC-SMBI is faster than compared with EA-SMBI. In the east anchor SMBI, the system is far away from the plasma, therefore it takes time to achieve peak value of Hα emission intensity. On the other hand, in the central-cell SMBI, the system is very close to the plasma and the peak value of Hα emission intensity become faster.

The variation of electron line-density in the central-cell (ΔNLcc) and east anchor-cell (ΔNLea) during EA-SMBI is shown in Fig. 4.27(a). Both ΔNLcc and ΔNLea increase in the increase of the plenum pressure. At high plenum pressure, the electron line density in the central-cell is slightly higher compared with east anchor-cell. The change in Hα emission intensity ($\Delta I_{H\alpha}$) with plenum pressure during SMBI is shown in Fig. 4.27(b). From this figure it is observed that the change in Hα emission intensity increases linearly with increase of plenum pressure. Since both ΔNLcc and $\Delta I_{H\alpha}$ as shown in Fig. 4.27(a) and Fig. 4.27(b) increase to SMBI plenum pressure, the particle fueling rate by EA-SMBI is proportional to the plenum pressure in this operation range.
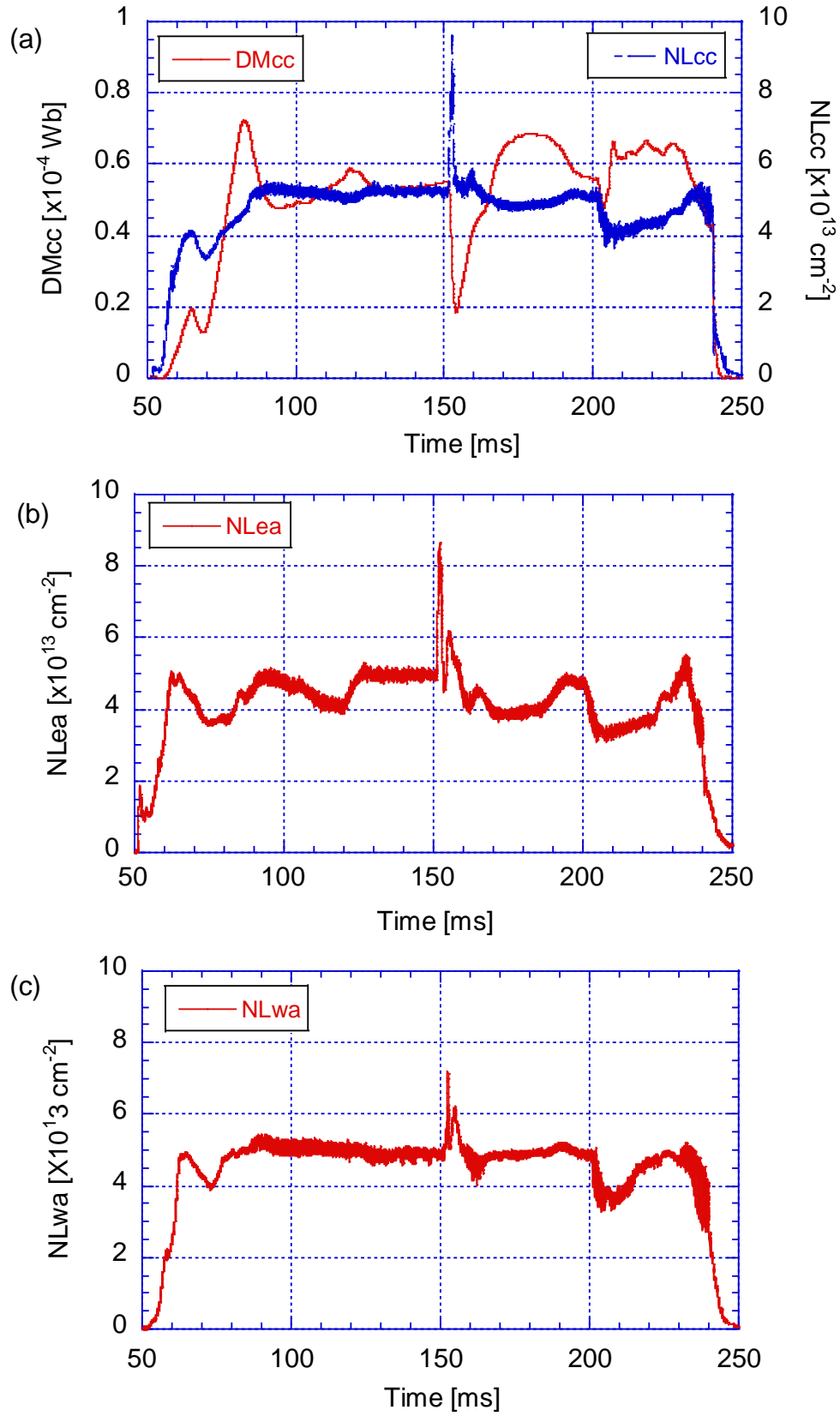
Fig. 4.25 Time evolution of line-integrated electron density during EA-SMBI with fixed pulse width 0.5 ms (a) in the central-cell, (b) in the east anchor-cell and (c) in the west anchor-cell.
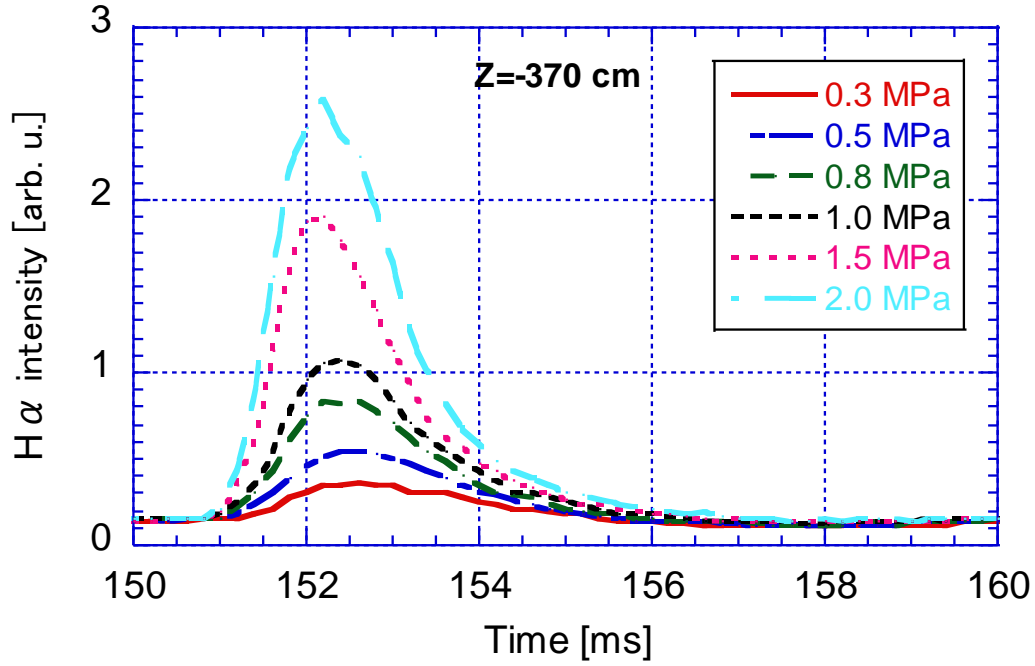
Fig. 4.26 Time evolution of Hα-line emission intensity at Z=-370 cm during EA-SMBI with fixed pulse width 0.5 ms for different plenum pressure.
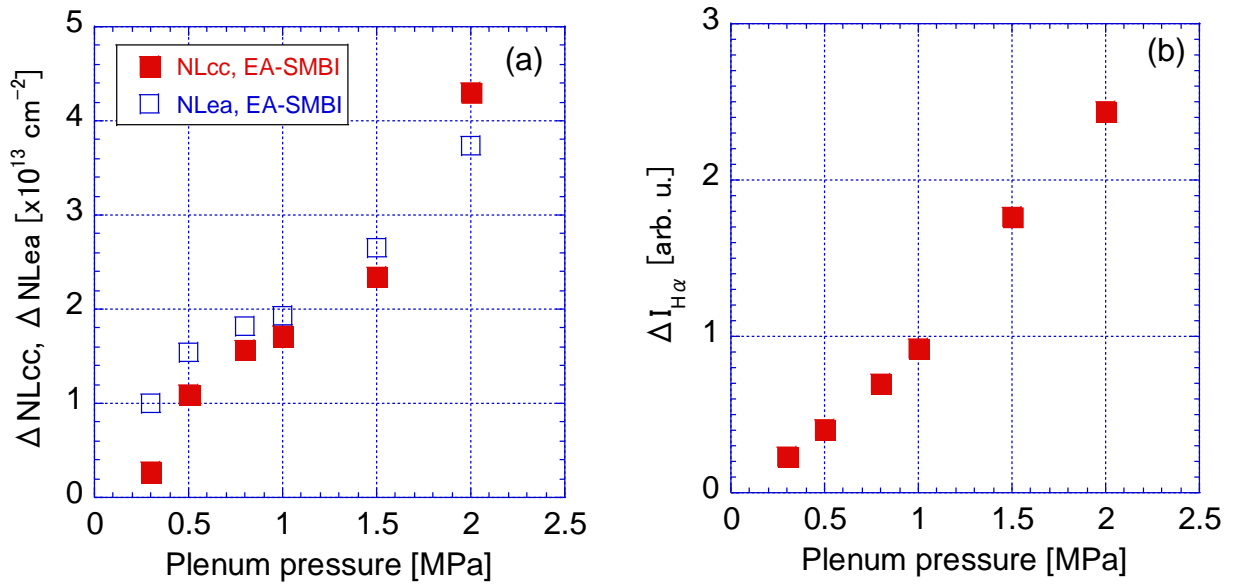

Fig. 4.27 EA-SMBI plenum pressure dependence of (a) change in electron line-density in the central-cell and east anchor-cell and (b) change in Hα emission intensity at Z=-370 cm with fixed pulse width 0.5 ms.

4.3.2 EA-SMBI pulse width dependence of plasma parameter

In the pulse width dependence of EA-SMBI experiment, SMBI pulses is injected using new Laval nozzle into the typical plasmas heated by only ICRF with fixed plenum pressure 1.0 MPa. By changing the SMBI pulse width from 0.3 ms to 2.0 ms, the response of the gas fueling by SMBI to the electron density (NLcc) and diamagnetism (DMcc) is investigated. Figure 4.28(a) shows the time evolution of line-integrated electron density and diamagnetism during EA-SMBI on ICRF heated plasma at pulse width 2.0 ms. From this figure it is observed that the electron line-density is increased during SMBI and the diamagnetism is decreased due to charge-exchange loss of hot ions. The response of EA-SMBI to electron line-density in the east anchor is shown in Fig. 4.28(b). The change in electron line-density during EA-SMBI in the central-cell and anchor-cell is almost the same. The increase in electron line-density in the west anchor-cell is shown in Fig. 4.28 (c). From this figure it is observed that the electron line-density is increased during SMBI. However, the increase in electron line-density in the west anchor-cell less than the east anchor-cell. Since EA-SMBI system is situated in the east anchor-cell, the increase in east anchor-cell electron line-density is higher compared with east anchor.

The response of EA-SMBI to Hα emission intensity is measured by the Hα-detector at Z = -370 cm. Figure 4.29 shows the time evolution of Hα-line emission intensity during EA-SMBI for different pulse width with the fixed plenum pressure of 1.0 MPa. The pulse width is varied from 0.3 ms to 2.0 ms. From this figure it is observed that the Hα emission intensity increases with the increase of the pulse width. The peak value of Hα emission intensity is delayed with increase of pulse width. At longer pulse operation the peak value of Hα emission intensity become saturated and the time evolution become broad.

The pulse width dependence of the change in electron line-density in the central-cell (ΔNLcc) and east anchor-cell (ΔNLea) during EA-SMBI is shown in Fig. 4.30(a). From this figure it is observed that both ΔNLcc and ΔNLea during EA-SMBI are increased with the increase of the pulse width in the short pulse range. However at the longer pulse width, both ΔNLcc and ΔNLea become saturated during EA-SMBI. The change in the Hα emission intensity ($\Delta I_{H\alpha}$) with the SMBI pulse width is shown in Fig. 4.30(b). The change in the Hα emission intensity ($\Delta I_{H\alpha}$) initially increases with increase of pulse width and then it is saturated as like the change in electron line-density. Since both ΔNLcc and $\Delta I_{H\alpha}$ as shown in Fig. 4.30(a) and Fig. 4.30(b) are shows same behavior to SMBI pulse width, the particle fueling rate by EA-SMBI is proportional to the SMBI pulse width in this operation range.
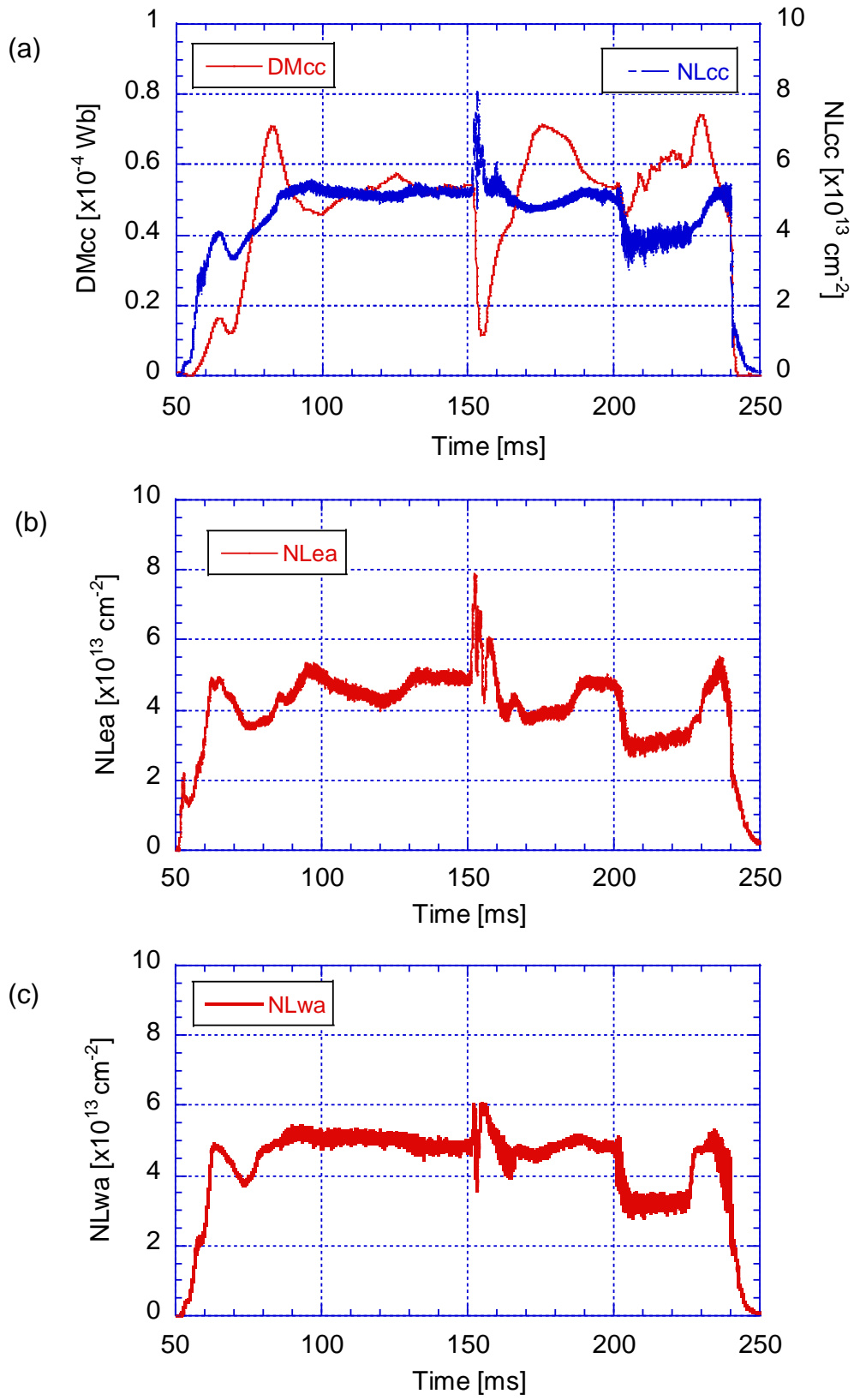
Fig. 4.28 Time evolution of line-integrated electron density during EA-SMBI with fixed plenum pressure 1.0 MPa (a) in the central-cell, (b) in the east anchor-cell and (c) in the west anchor-cell.
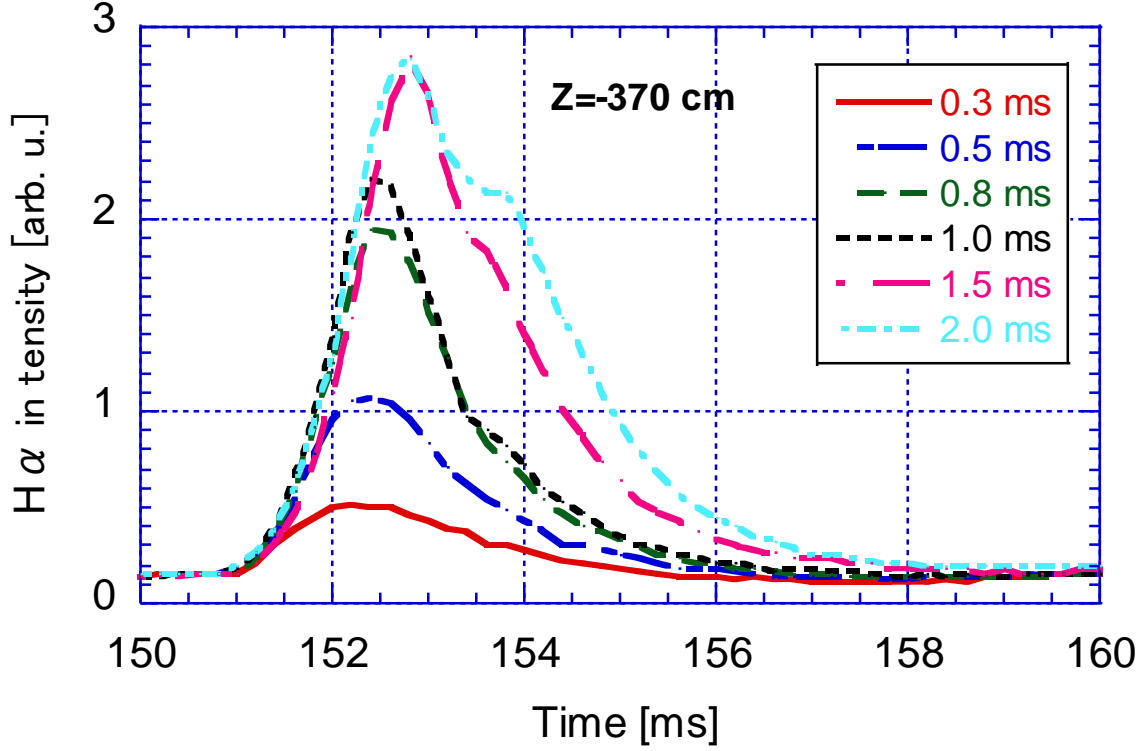
Fig. 4.29 Time evolution of Hα-line emission intensity at Z=-370 cm during EA-SMBI with fixed plenum pressure 1.0 MPa for different SMBI pulse width.
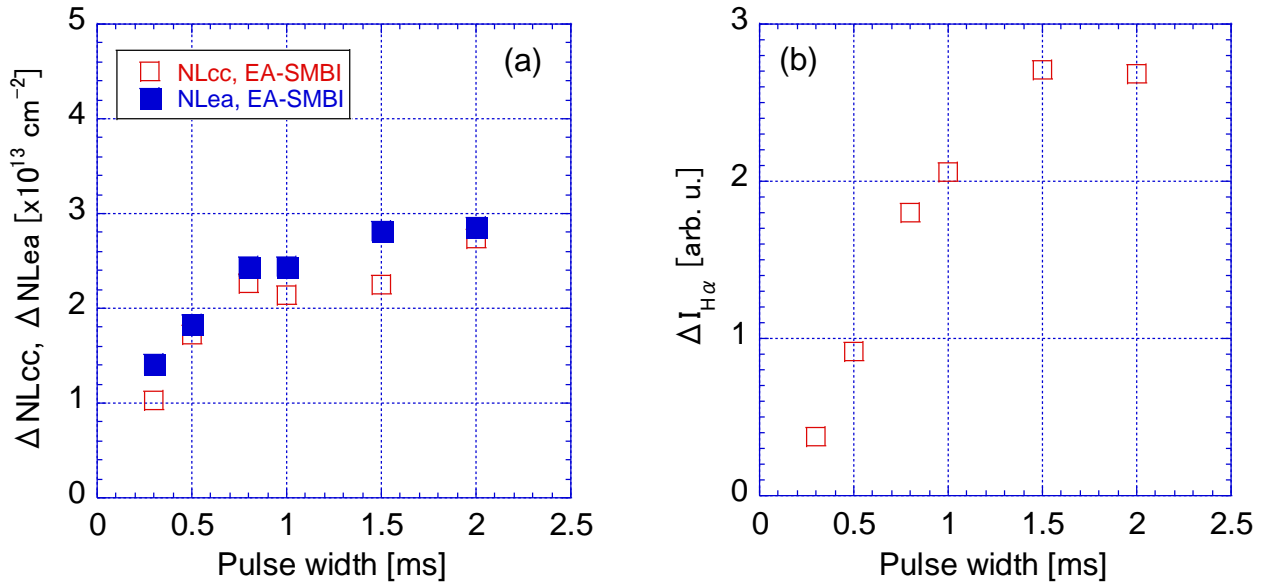

Fig. 4.30 EA-SMBI pulse width dependence of (a) change in electron line-density in the central-cell and east anchor-cell and (b) change in Hα emission intensity at Z=-370 cm with fixed SMBI plenum pressure 1.0MPa.

4.4 Plenum Pressure Dependence of CC-SMBI and EA-SMBI Results Comparison

In order to compare the SMBI experimental results in both regions, SMBI pulse is injected at 150 ms and pulse width is 0.5 ms. The plenum pressure is varied from 0.3 MPa to 2.0 MPa. The comparison of SMBI plenum pressure dependence of change in electron line-density during CC-SMBI and EA-SMBI as shown in Fig. 4.31 (a). From this figure it is observed that the change in electron line-density is slightly higher in the case of CC-SMBI at high plenum pressure. Figure 4.31(b) shows the change in Hα-line emission intensity during CC-SMBI and EA-SMBI which are measured at Z = -1 cm and Z = -370 cm, respectively. The Hα-detector at Z = -1 cm is close to the CC-SMBI location and Z = -370 cm is close to the EA-SMBI location. In both cases the change in Hα emission intensity increases linearly with increase of plenum pressure. Both electron line density ($\Delta NLcc$) and Hα-line emission ($\Delta I_{H\alpha}$) increases almost linearly with the increase of SMBI plenum pressure during SMBI in both region. Since both $\Delta NLcc$ and $\Delta I_{H\alpha}$ shows same fashion to SMBI plenum pressure, the particle fueling rate by SMBI is proportional to the plenum pressure in this operation range in both regions.

Figure 4.32 shows the DMcc behavior during SMBI in the central-cell and east anchor inner-transition region at plenum pressure of 1.0 MPa and pulse 0.5 ms. In both regions the DMcc is reduced during SMBI. The plenum pressure and pulse width dependence of the bottom value of diamagnetism during EA-SMBI is shown in Fig. 4.33(a) and Fig. 4.33(b). From the Fig. 4.33(a) it is observed that the bottom value of DMcc decreases gradually with the increase of the plenum pressure. The bottom value of DMcc is also decreased gradually with the increase of the pulse width as shown in Fig. 4.33(b). However, at the longer pulse operation, the bottom value of DMcc is low compare with the higher plenum pressure. On the other hand, the increase of the electron line-density is high in the case of high plenum pressure compared with long pulse width as shown in Figs. 4.25(a) and 4.28(a) for 2.0 MPa and 2ms, respectively. It implies that SMBI with high plenum pressure is more effective than longer pulse width.

Figure 4.34 shows the comparison of the plenum pressure dependence of the bottom value of diamagnetism during CC-SMBI and EA-SMBI with fixed pulse width of 0.5 ms. In the case of CC-SMBI, the value is almost the same in the plenum pressure range from 0.3 MPa to 2.0 MPa. The reduction of DMcc in the CC-SMBI is due to the increase in the CX loss of the hot ions produced by ICRF that could be confirmed by the axial distribution of Hα-line emission intensity in the central-cell as shown in Figs. 4.35(a)-(c). However, the reduction of DMcc in the case of EA-SMBI may not be due to the CX loss. The response of Hα-line emission intensity in the central-cell is not remarkably observed during EA-SMBI as shown in Figs. 4.36(a)-(c). It may be speculated that the reduction of DMcc in the EA-SMBI is due to the degradation of the ICRF heating efficiency.
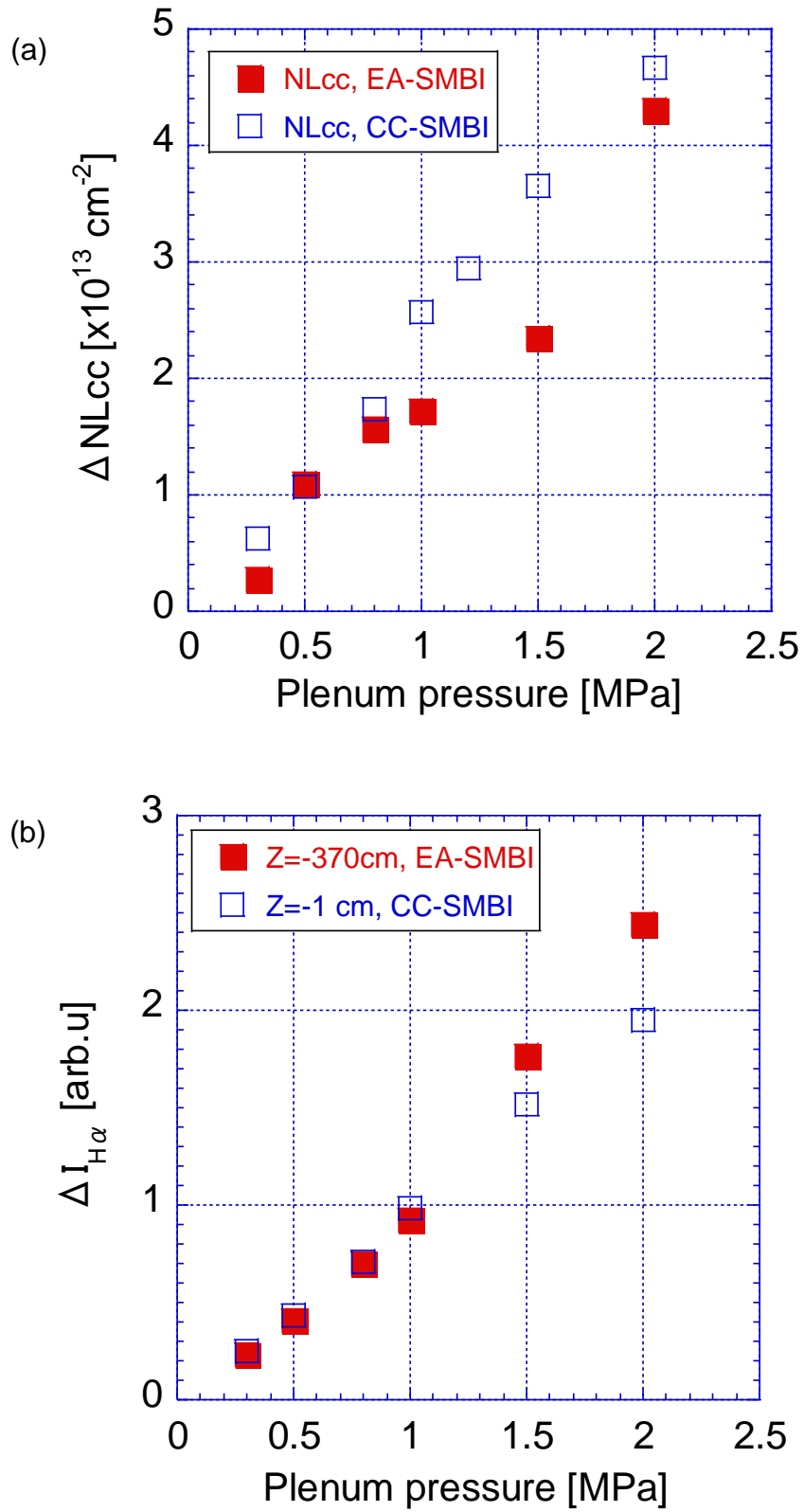
Fig. 4.31 Comparison of SMBI plenum pressure dependence of (a) change in electron line-density and (b) change in Hα emission intensity during CC-SMBI and EA-SMBI.
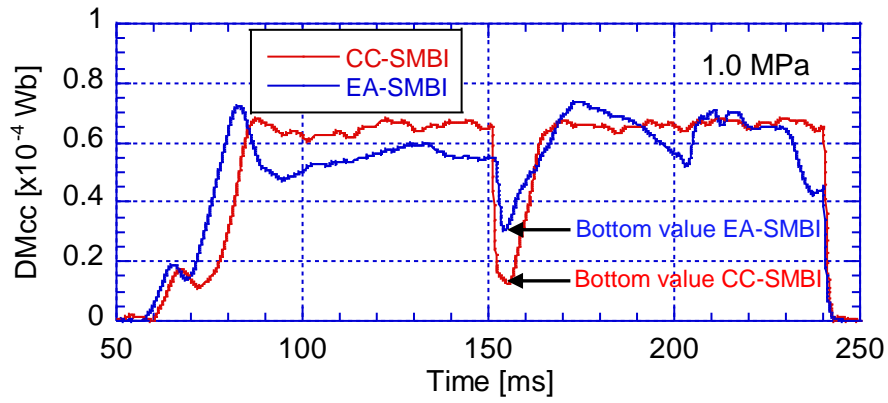
Fig. 4.32 Time evolution of DMcc during SMBI at 1.0 MPa and pulse width 0.5 ms.

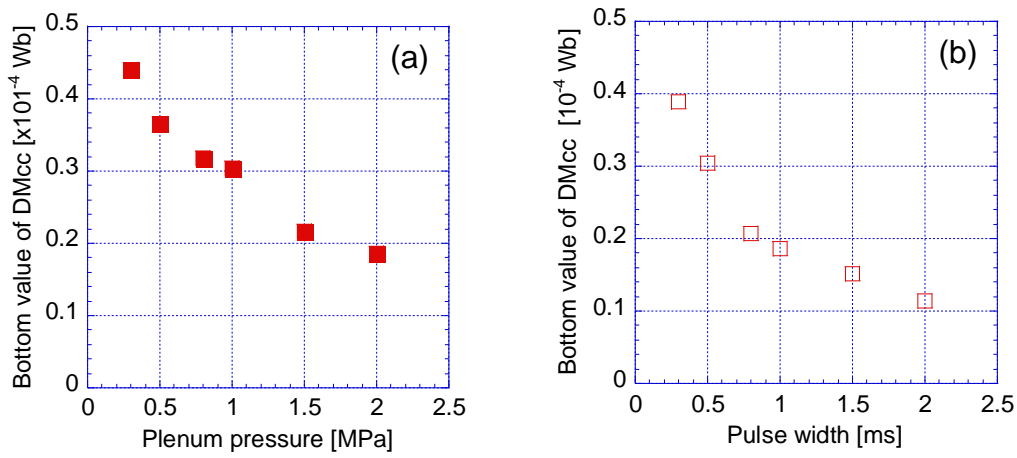Fig. 4.33 Comparison of SMBI plenum pressure and pulse width dependence of the bottom value of diamagnetism during EA-SMBI.
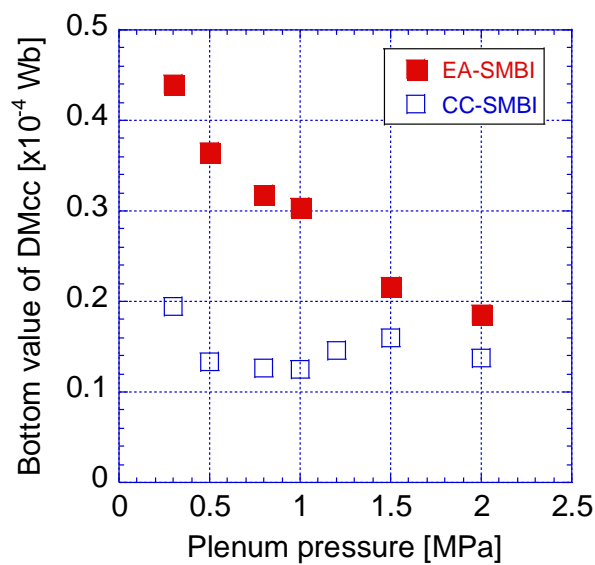

Fig. 4.34 Comparison of SMBI plenum pressure dependence of the bottom value of diamagnetism during CC-SMBI and EA-SMBI.
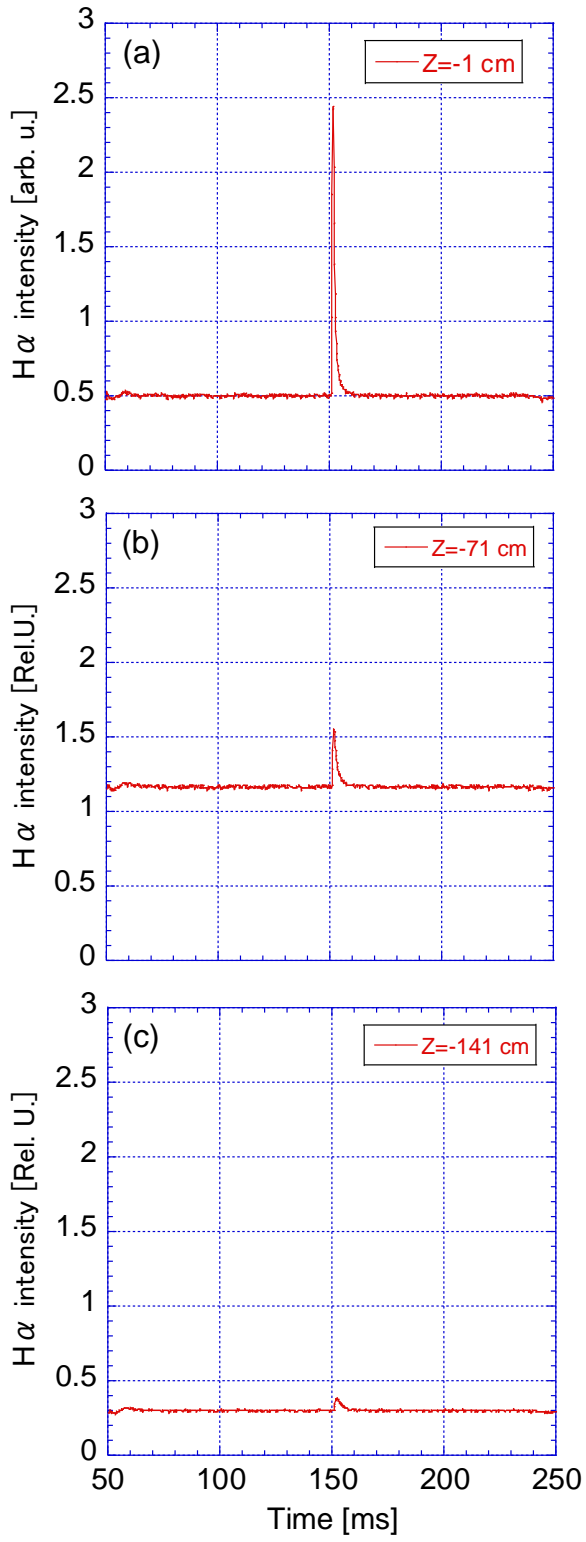
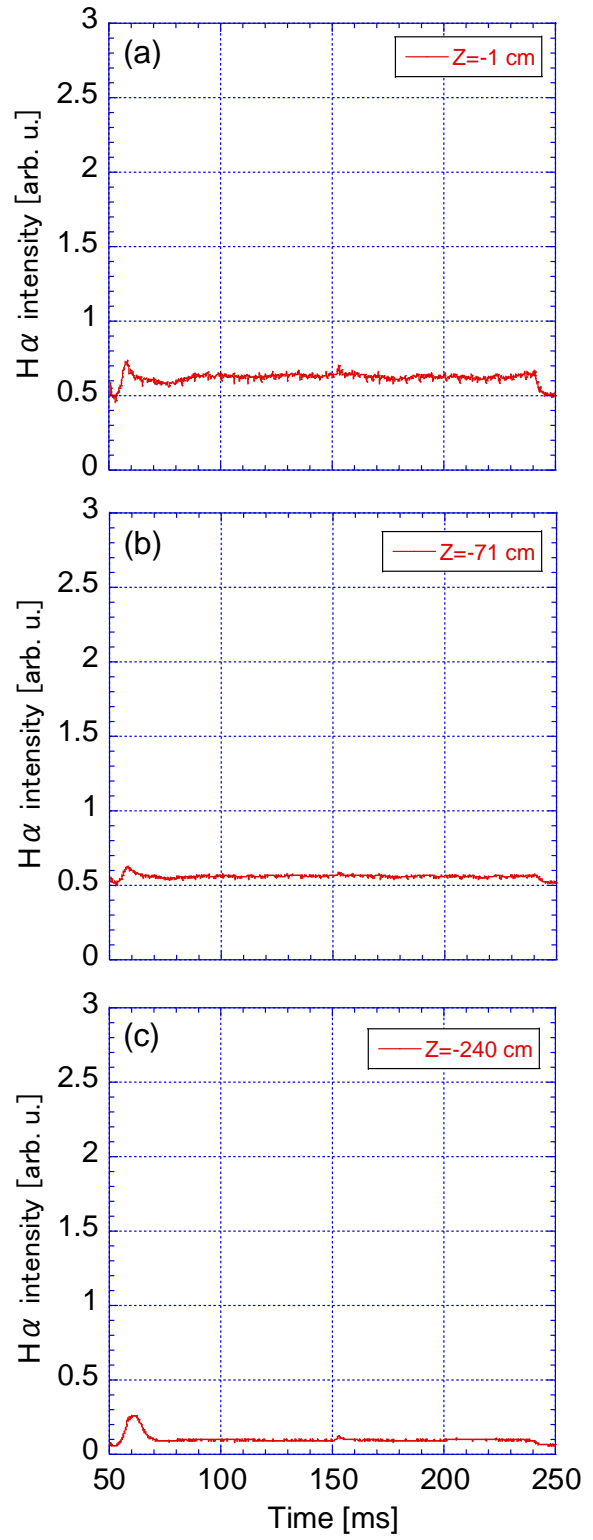Fig. 4.35 Axial distribution Hα emission intensity in the central-cell during CC-SMBI.

Fig. 4.36 Axial distribution Hα emission intensity in the central-cell during EA-SMBI.

4.5 Estimation of Fueling Efficiency

The fueling efficiency during SMBI experiments is defined as the ratio of the increase in plasma electron contents to the injected particles by SMBI. In order to evaluate the injected particles by SMBI in GAMMA 10, the pressure difference, ΔP between the chamber is measured just before SMBI and that measured after SMBI under the condition that all pumping systems are closed. ΔP is measured for different SMBI plenum pressure (0.5 MPa, 1.0 MPa, 1.5 MPa and 2.0 MPa) with fixed pulse width of 0.5 ms. Accordingly, ΔP is also measured for different pulse width (1.0ms, 2. ms and 4.0 ms) by changing SMBI plenum pressure. All processes are performed without plasma discharge in order to evaluate the injected particles. Figure 4.37 shows the variation ΔP with SMBI plenum pressure for different pulse width. From this figure it is observed that the ΔP increases with increase of SMBI plenum pressure as well as pulse width. The value of ΔP for each pulse width is reduced to 0.5 ms. Fig. 4.38 shows the variation of ΔP with SMBI plenum pressure for reduced pulse width of 0.5 ms. From this figure ΔP is evaluated to be 1.9×10^{-5} Pa corresponding to plenum pressure 1.0 MPa. Then the number particles is calculated by considering the whole volume of GAMMA 10 for the plenum pressure of 1.0 MPa. The volume of GAMMA 10 is calculated to be 150 m^3. The increase in plasma electron contents for plenum pressure 1.0 MPa and pulse width 0.5 ms is measured by microwave interferometer as shown in Fig. 4.17(b). The peak value of electron density is shown in this figure. Then we calculate total number of electrons in the central-cell ($Lcc = 6$ m) by the following formula,

$$N_p = \int_0^{20} 2\pi r n_e(r) dr \times L_{cc}.$$

By using the above formula, the number of electrons in the central-cell is calculated without SMBI and after the SMBI. The number of electrons is also calculated during SMBI with ECRH. The fueling efficiency, η during SMBI is about 23% and SMBI with ECRH is about 31%. These values are given in Table 4.1. The electron temperature is increased during ECRH injection and high Hα emission intensity is observed during SMBI due to the enhancement of ionization. It is also observed that the electron line-density in the central-cell is higher in the case of ECRH injection due to potential formation by ECRH. Therefore, the fueling efficiency is increased during SMBI with ECRH. In this calculation considerable ambiguities is remaining. However the obtained fueling efficiency in GAMMA 10 is almost near to the value of other devices like LHD, JT-60U, Tore Supra, ASDEX-U, EAST tokamak, etc.

Table 4.1: Fueling efficiency at SMBI plenum pressure 1.0MPa and 0.5 ms pulse width.

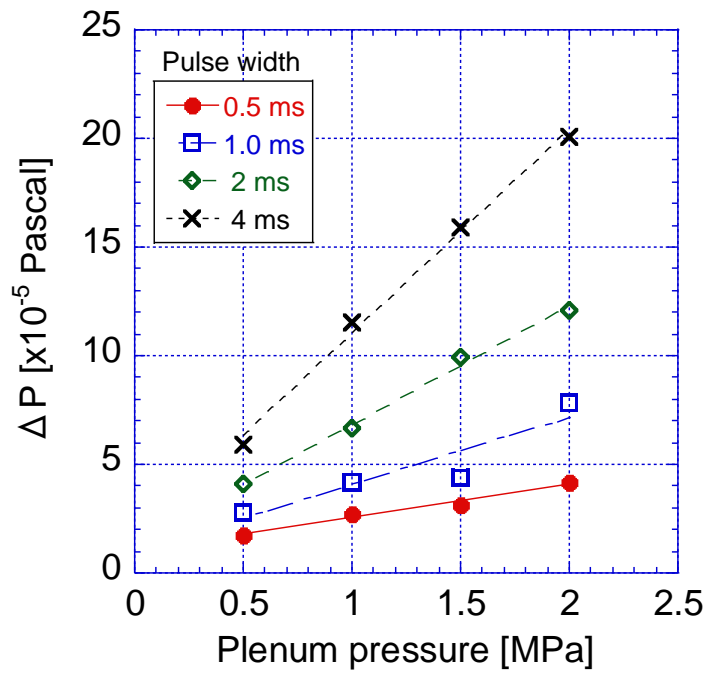| Fueling system	ΔP ($\times 10^{-5}$ Pascal)	N_{SMBI} ($\times 10^{17}$ particles)	ΔN_p ($\times 10^{17}$ electrons)	η
SMBI	1.9	7.5	1.7	23%
SMBI+ECRH	1.9	7.5	2.3	31%

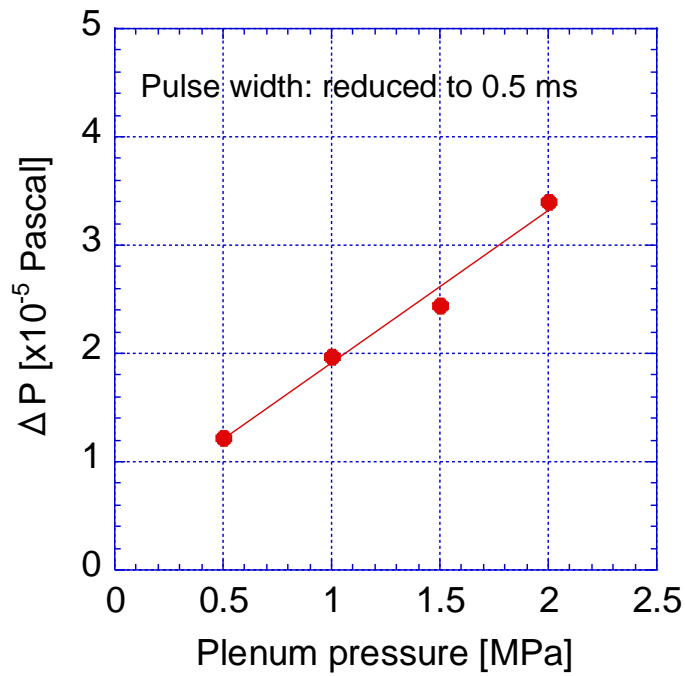Fig. 4.37 SMBI plenum pressure dependence of ΔP for different pulse width.

Fig. 4.38 SMBI plenum pressure dependence of ΔP for reduced pulse width 0.5 ms.

Chapter 5

Numerical Study by Monte-Carlo Simulation

In this chapter, we describes the neutral particle behavior during supersonic molecular beam injection (SMBI) fueling by a numerical simulation performed in the GAMMA 10 tandem mirror. Three-dimensional Monte-Carlo code DEGAS is applied to GAMMA 10 in order to investigate precisely the spatial distribution of neutral particle density during SMBI. In the GAMMA 10 tandem mirror, the neutral transport code DEGAS [37, 38] has been applied and the simulation study has been performed [61-70]. Based on the experimental measurements, the detailed neutral distribution is predicted by using Monte-Carlo simulation.

5.1 Modeling of Mesh, Plasma Parameter and Particle Source

5.1.1 Mesh model for the DEGAS code

The three-dimensional neutral transport simulation has been carried out by using the DEGAS of version 63 (DEGAS ver.63) Monte-Carlo code [38]. This code is developed for the simulation of the high plasma density region. However, the density of GAMMA 10 is less than 10^{19} m^{-3}. This discrepancy is attributed to the production of hydrogen atoms at excited levels by the direct-dissociation of hydrogen molecules upon electron impact. The dissociative-excitation reactions of neutral hydrogen molecules are additionally included so as to calculate low density plasma in the plasma edge region for applying the DEGAS code to the GAMMA 10 plasma [54]. Figure 5.1(a) shows the fully three-dimensional mesh model applied to the central-cell. In this model, the simulation space is divided into 11 segments radially and 32 segments circularly. In the axial direction, 83 segments are defined in the central-cell of length 6 m (Z = +3 m and Z = -3 m). In simulation model, the limiter and ICRF antennas are precisely implemented in a realistic configuration. Moreover, this mesh model is improved for modeling SMBI experiments with Laval nozzle which is expanded around the SMBI port. This new mesh is added in a realistic configurations about the SMBI valve with Laval nozzle. The schematic view of the vicinity of the Laval nozzle is shown in Fig. 5.1(b).
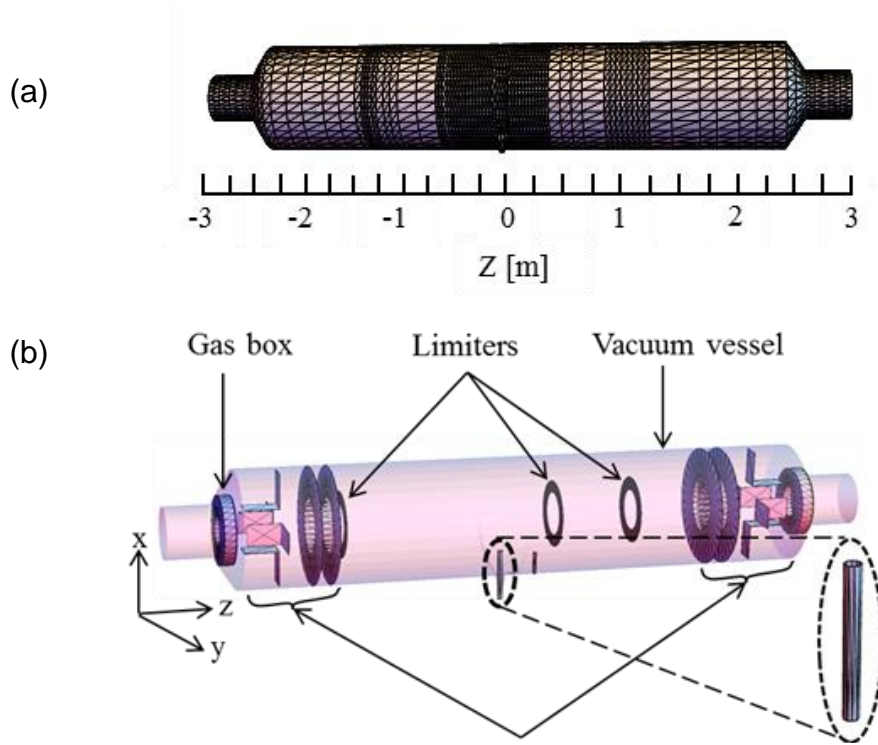
Fig.5.1 Mesh model used for the 3-D DEGAS simulation, (a) surface structure of the vessel, (b) structure of second wall and vicinity of Laval nozzle.

5.1.2 Modeling of plasma parameter and particle source

Plasma parameter model as assumed in the simulation is shown in Fig. 5.2. In the density model, the conservation of particle flux of the flowing plasma is assumed along the axial direction. Then the density profile is determined on the basis of the measured data at the central-cell as shown in Fig. 5.2(c). The parallel component of ion velocity is determined from the $T_{i//}$ measured with the end-loss ion energy analyzer. Figure 5.2(a) shows the ion temperature profile. The radial profile is determined using the charge-exchange neutral particle analyzer, and its axial variation is obtained from axial profile of the diamagnetic signals in the central-cell. The electron temperature distribution is taken to be constant along the magnetic flux tube based on the soft x-ray measurements as shown in Fig. 5.2(b). In the present simulation, SMBI is performed only in the central-cell. The background plasma parameters on each mesh is given based on the experimental data as shown in Fig. 5.2. The axial and radial distribution of Hα emission is evaluated to investigate the neutral transport during SMBI.

In the DEGAS simulation in GAMMA 10, velocity profile of the neutral source is given in a cosine distribution. However, the neutral source from SMBI makes different profile from the conventional process such as gas puffer and recycling phenomena according to the experimental results. Hence, the neutral source is modified for the neutral source of SMBI. A parameter σ_{div} is introduced to simulate the molecular beam injected by SMBI to index the divergence angle of the initial particles. In the case of $\sigma_{div} = 1.0$, the angular profile of launched particles follows a cosine distribution. If $\sigma_{div} = 0.5$, the horizontal component (y or z) of the velocity vector in the cosine distribution is

reduced to half. Figures 5.3(a), (b), (c) and (d) show the schematic view of the distribution of launched particles with $\sigma_{div} = 1.0$, $\sigma_{div} = 0.5$, $\sigma_{div} = 0.33$ and $\sigma_{div} = 0.25$, respectively.
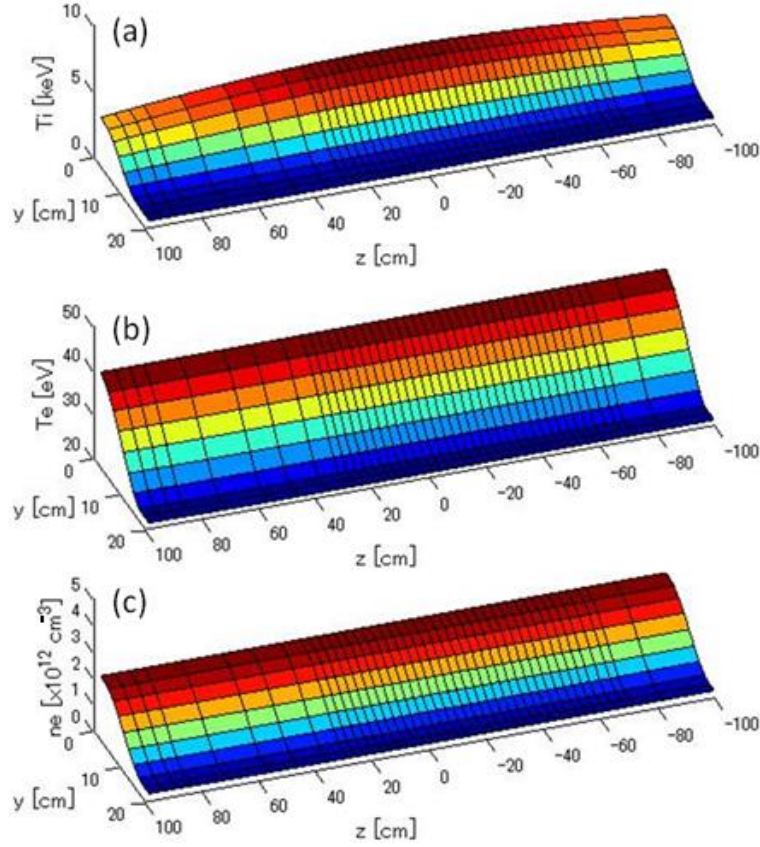

Fig.5.2 Input plasma parameters applied to DEGAS simulation (a) ion temperature, (b) electron temperature and (c) electron density.
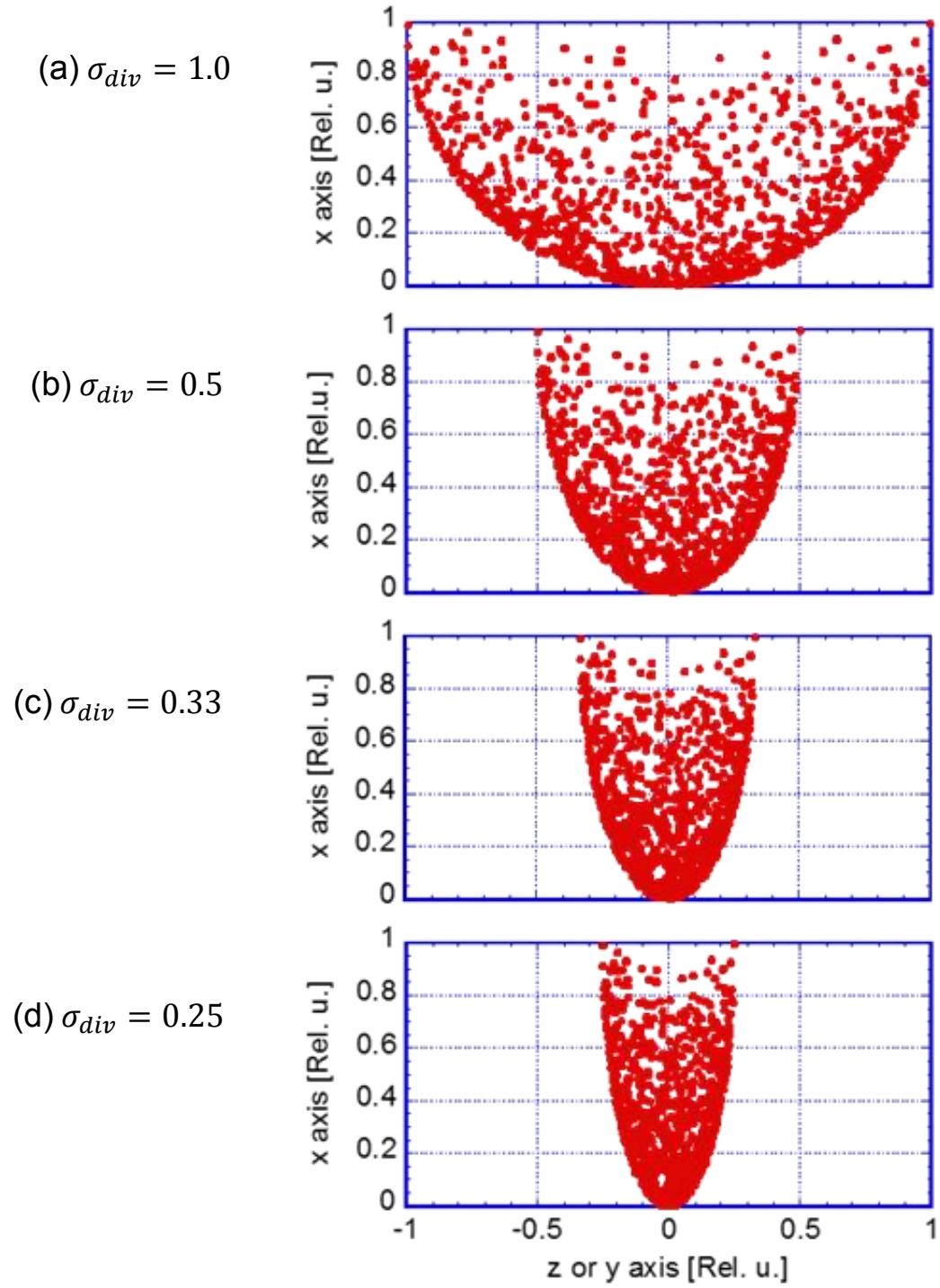
(a) $\sigma_{div} = 1.0$

(b) $\sigma_{div} = 0.5$

(c) $\sigma_{div} = 0.33$

(d) $\sigma_{div} = 0.25$

Fig.5.3 Distribution of launched particles with different divergence angle index.

5.1.3 Improved model in the simulation

In the simulation, divergence angle index of initial particle σ_{div}, is introduced to simulate the molecular beam injected by SMBI. The angular profile of launched particles has a cosine distribution in the case of $\sigma_{div} = 1.0$. The particle become convergent by reducing the value of divergence angle index along y and z-direction. The velocity component along y and z-direction decreases due to $\sigma_{div} < 1.0$. Therefore, the velocity component along fueling direction i.e. x-direction is modified to compensate the velocity component.

If v is the velocity of the initial particle,

$$v^2 = v_x^2 + v_y^2 + v_z^2.$$

If we change the y and z-component of the velocity to half of cosine distribution as shown in Fig. 5.3(b) i.e. $\sigma_{div} = 0.5$, then the velocity reduces to

$$v_1^2 = (v_x^2 + \sigma_{div}^2 v_y^2 + \sigma_{div}^2 v_z^2),$$

where, $\sigma_{div} < 1$ and $v^2 > v_1^2$.

Therefore, we modified the vertical component *i.e.* the x-component of the velocity to conserve the energy and introduced another parameter β, which is define as

$$\beta^2 = \frac{v^2}{v_1^2}$$

Therefore, the new velocity after modified the x-component is

$$v_{1new}^2 = (\beta^2 v_x^2 + \sigma_{div}^2 v_y^2 + \sigma_{div}^2 v_z^2).$$

The value of β^2 for different value of σ_{div} is given in Table 1. The value of β^2 increases with decrease of divergence angle index, σ_{div} as shown in Fig. 5.4.

Table 1: value of σ_{div} and β^2

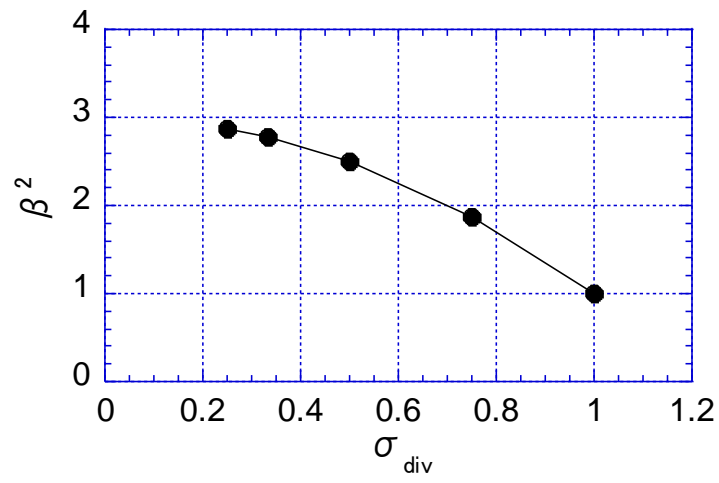| σ_{div}	1.0	0.75	0.5	0.33	0.25
β^2	1.0	1.875	2.5	2.778	2.875

Fig.5.4 Variation of β^2 with divergence angle index, σ_{div}.

5.2 Simulation Results and Discussion

5.2.1 Spatial profile of neutral hydrogen density

The cross-sectional profiles of molecular hydrogen density is obtained from the simulation are shown in Fig. 5.5 at Z = -14.5 cm, -17.5 cm, -20.5 cm, -23.5 cm, -26.5 cm and -29.5 cm with divergence angle index σ_{div} = 1.0. The particles are injected from the bottom at Z = -14.5 cm in the central-cell. In the case of cosine distribution σ_{div} = 1.0, the molecules are diffused in the peripheral region and localized at the very bottom of the plasma. In Fig. 5.6, the molecular density profiles are compared at different divergence angle index, σ_{div} = 0.5, 0.33 and 0.25. In the case with σ_{div} = 0.5, the divergence of the distribution of molecule on the cross-section is reduced than that of σ_{div} = 1.0. In the case with σ_{div} = 0.33, the molecules are localized at the bottom of the plasma. In addition, expansion of neutral particles to the peripheral region are suppressed. In the case σ_{div} = 0.25, the molecules are localized at the injection point and reduces the dispersion of neutral particles to edge region compared with other cases of divergence angle index. The spatial distribution of molecular particles after velocity modification is shown in Fig. 5.7 with different divergence angle index. From this figure we observed that the molecules become more convergent compared with before modification of velocity in all divergence angle index cases. According to the reduction of σ_{div}, the molecules are localized along the z-direction and penetration increases along x-direction. The dispersion of the particle in the peripheral region is also reduced due to the reduction of divergence angle index σ_{div}. This simulation results indicated that the molecular density can be controlled by the directivity of the injected particle.
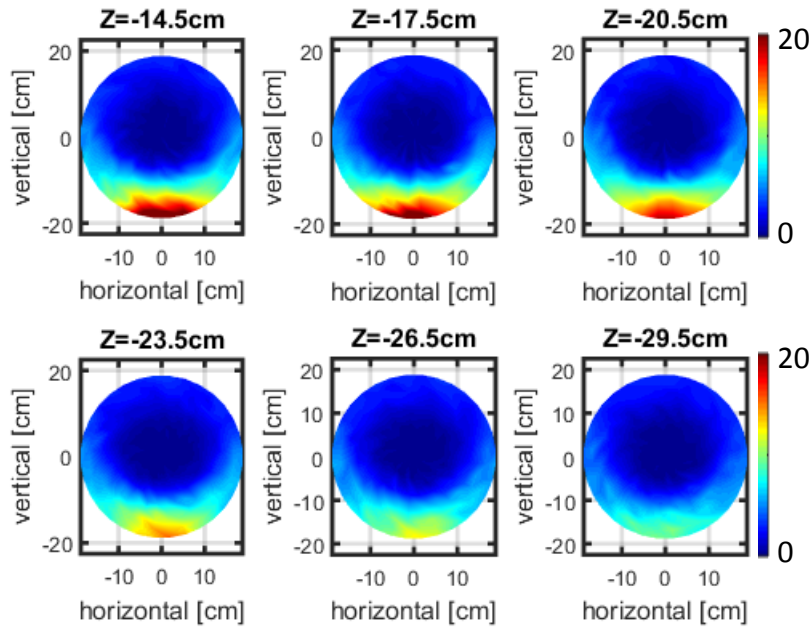

Fig.5.5 Results of 3D-DEGAS simulation in the case of $\sigma_{div} = 1.0$: cross-sectional molecular hydrogen density profile at different distance from SMBI injection position in the central-cell.
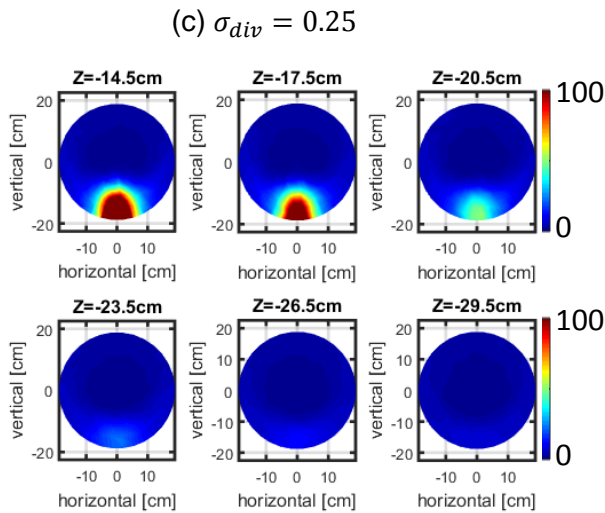
Fig.5.6 simulation results in the case of $\sigma_{div} = 0.5, 0.33$ and 0.25 before energy conservation: cross-sectional molecular hydrogen density profile at different distance from SMBI injection position.
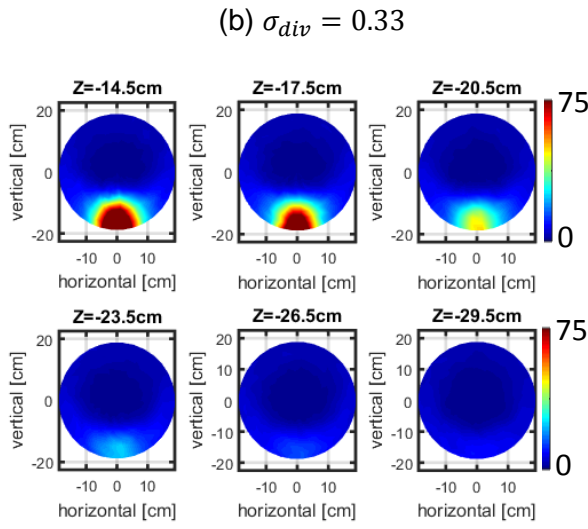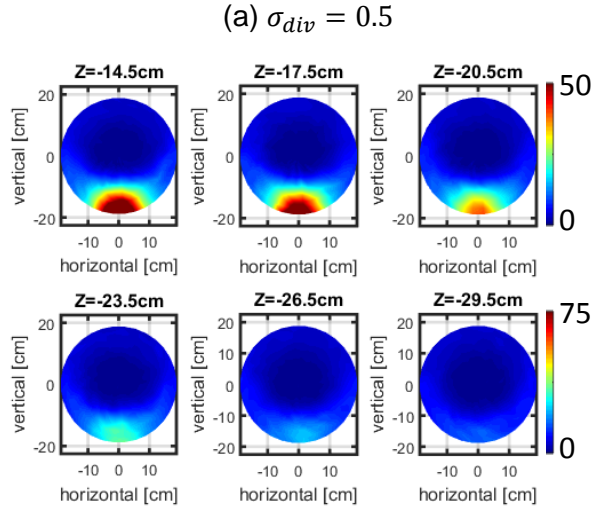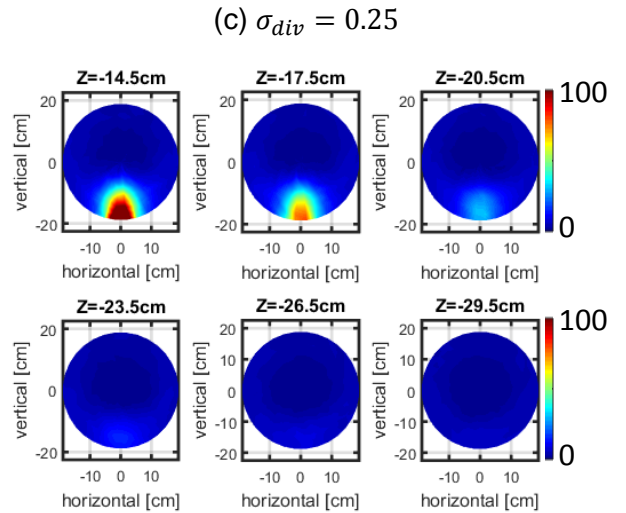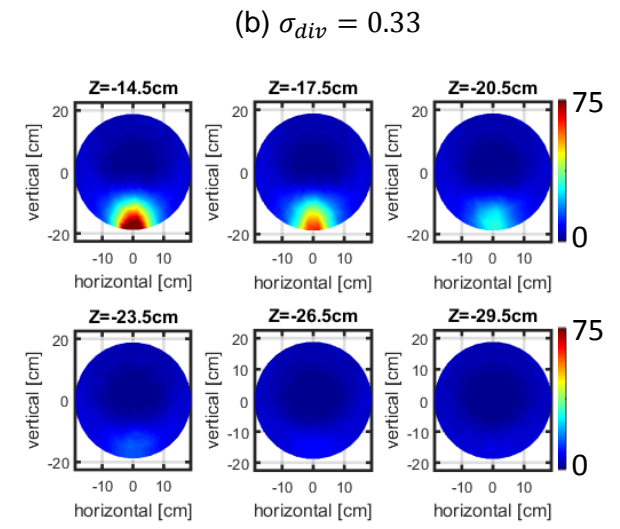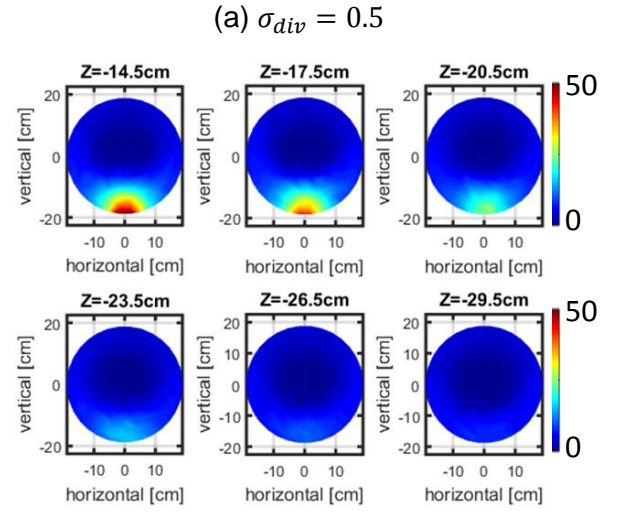
Fig.5.7 Simulation results in the case of $\sigma_{div} = 0.5, 0.33$ and 0.25 after energy conservation: cross-sectional molecular hydrogen density profile at different distance from SMBI injection position.

5.2.2 Cross-sectional profile of Hα intensity

Figure 5.8 shows the simulation results of the Hα emissivity on the plasma cross-section with σ_{div} = 1.0 at different distances from the injection point Z = -14.5 cm, -17.5 cm, -20.5 cm, -23.5 cm, -26.5 cm and -29.5 cm. In the case of σ_{div}=1.0, the emission area is large due to expansion of particles in the lower half of the plasma column. In the case with σ_{div} = 0.25, the amount of neutral particles are localized at the injection point, Z = - 14.5 cm as shown in Fig. 5.9. Hα emissivity is reduced away from the injection point. It could be due to the reduction of divergence angle index for which the particle are penetrated deeper and Hα is observed close to the core plasma. The penetration depth was calculated from the simulation results at injection point, Z = - 14.5 cm. The penetration depth is defined to be a distance from edge at x = - 18 cm to a distance where the intensity becomes maximum. The comparison of penetration depth before and after energy conservation with different divergence angle index are shown in Fig. 5.10(a) and 5.10(b). The peak position of emissivity increases with decrease of divergence angle index. It is found that the penetration depth is increased after energy conservation. The penetration depth before energy conservation is 9 cm and after energy conservation is 11 cm.

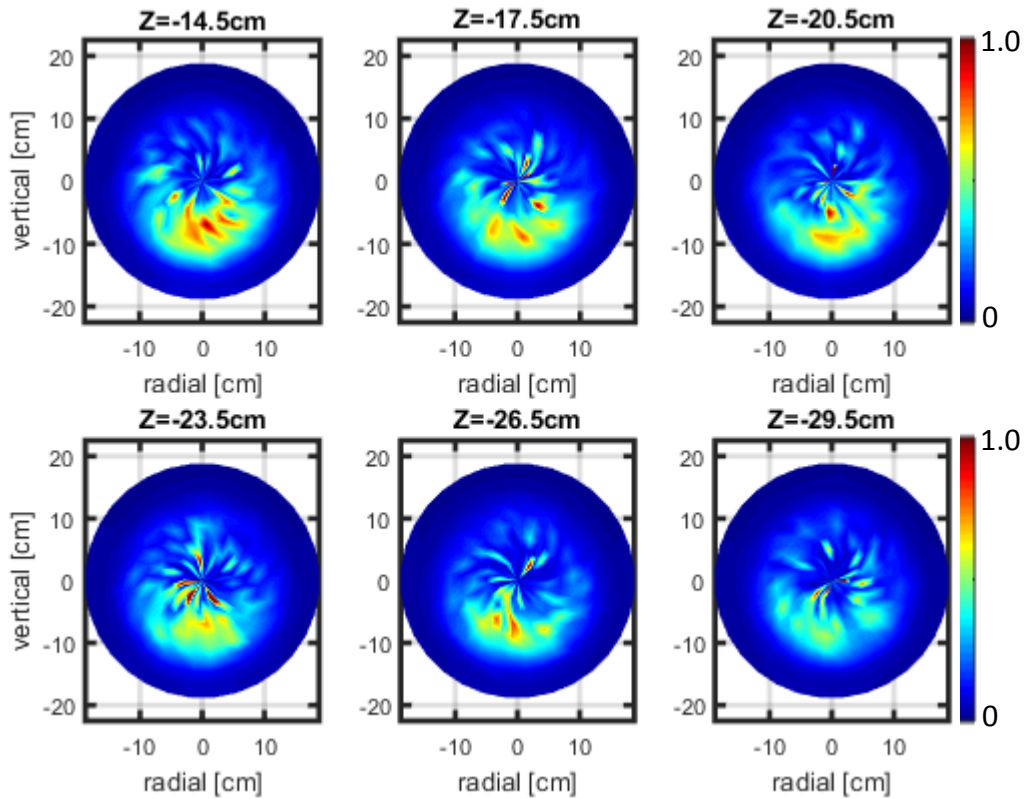Fig.5.8 Cross-sectional view of Hα line emission at different distances from the SMBI injection position for $\sigma_{div} = 1.0$
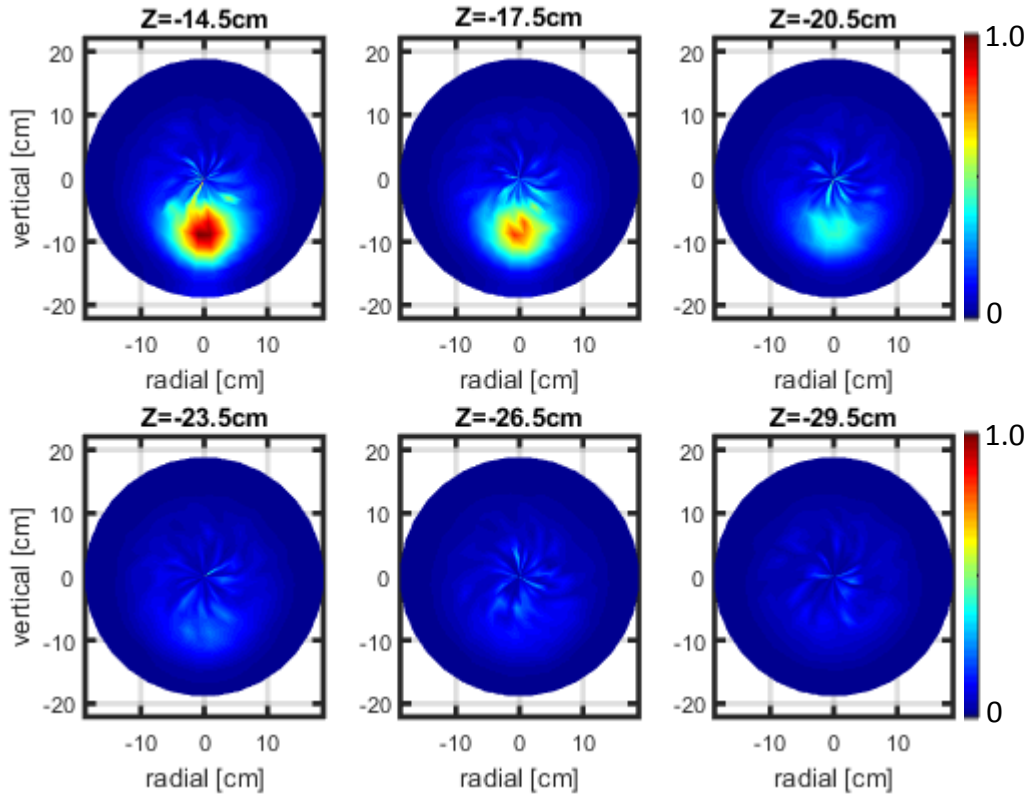
Fig.5.9 Cross-sectional view of Hα line emission at different distances from the SMBI injection position for $\sigma_{div} = 0.25$.
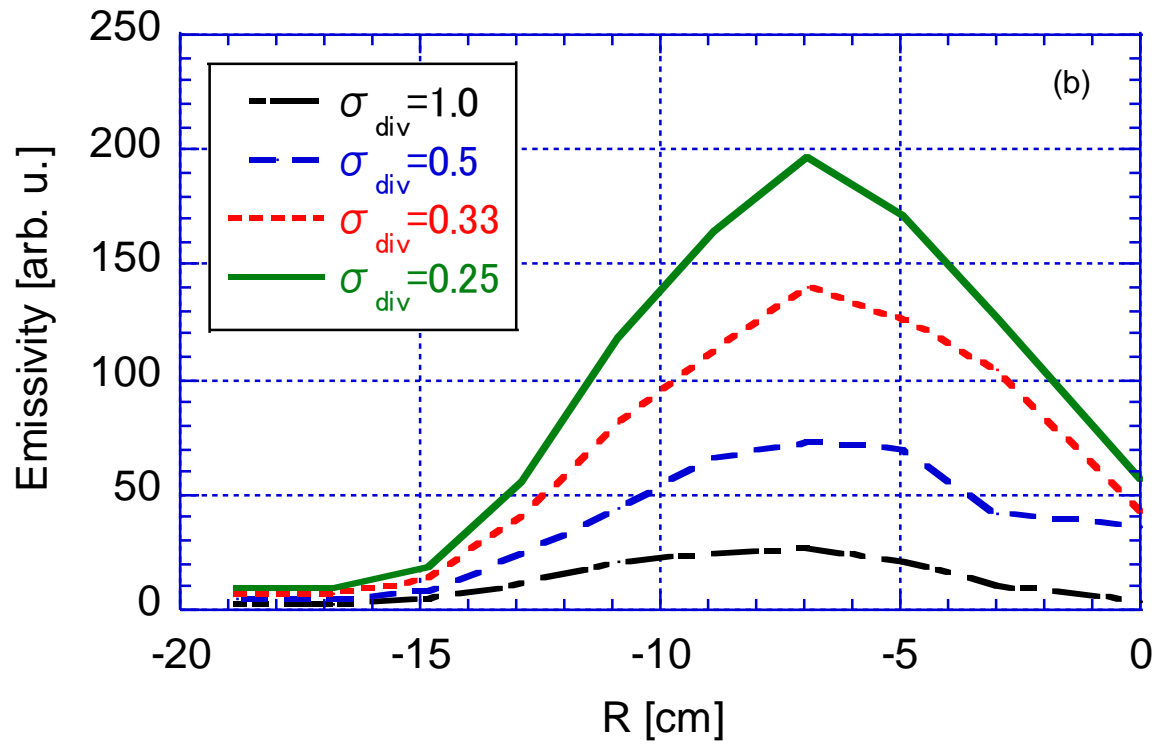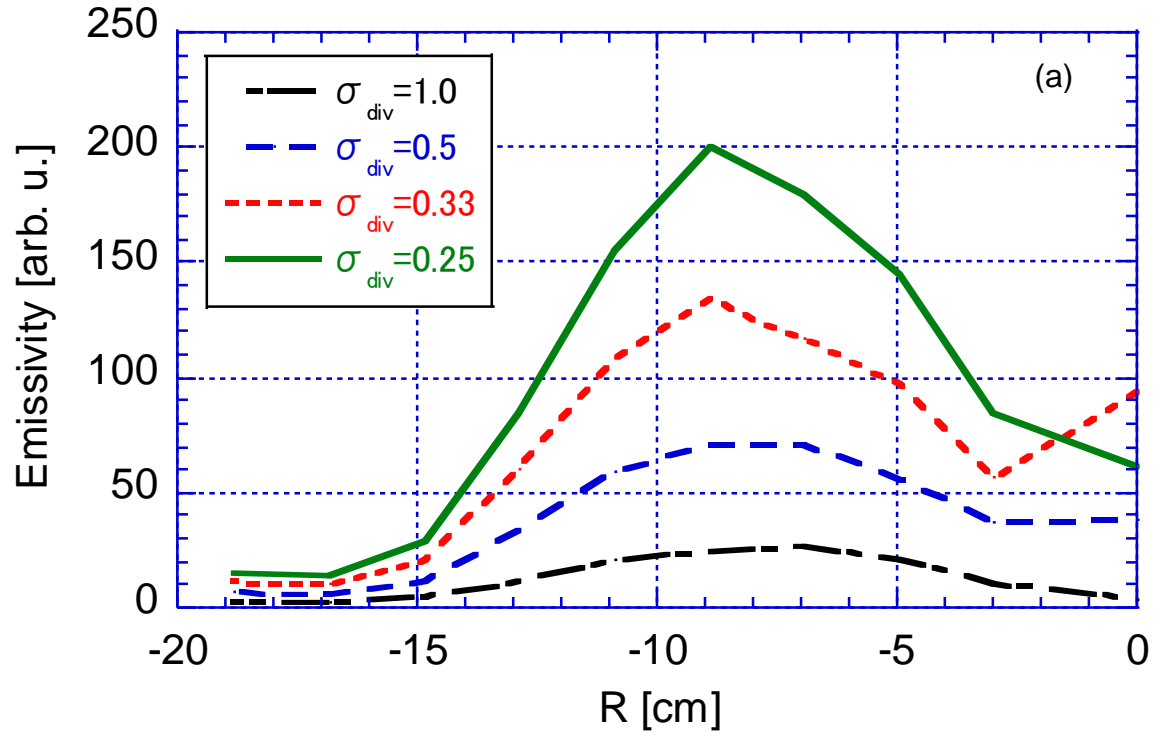
Fig.5.10 Dependence of the penetration depth on divergence angle index, (a) without energy conservation, (b) with energy conservation.

5.2.3 Axial profile of Hα intensity

The two-dimensional images (x-z or y-z) calculated by DEGAS are shown in Figs. 5.11(a)-(d) with σ_{div} = 1.0, 0.5, 0.33 and 0.25. Hα emission in larger area is observed in the case with σ_{div} = 1.0 as shown in Fig. 5.11(a). It might be due to the expansion of particles along horizontal (y-z) as well as radial (x) direction. In the case with σ_{div} = 0.5, we observed that the emission area become smaller due to reduction of expansion of particle in the axial and radial direction. The emission area is reduced more with divergence angle index σ_{div} = 0.33 and σ_{div} = 0.25 due to suppression and localization of particles near the injection point. The axial distribution of Hα emission near the SMBI injection port is shown in Figs. 5.12(a) and 5.12(b). In the case with σ_{div} = 1.0, the width of the curve is wider due to the emission from expanded particles. The Hα intensity peak position becomes narrower by decreasing the divergence angle index due to the suppression of the neutral particles. The Hα emission intensity is slightly higher in the case of energy conservation compared with non-conservation of energy as shown in Fig. 5.12(b).

(a) $\sigma_{div} = 1.0$

(b) $\sigma_{div} = 0.5$
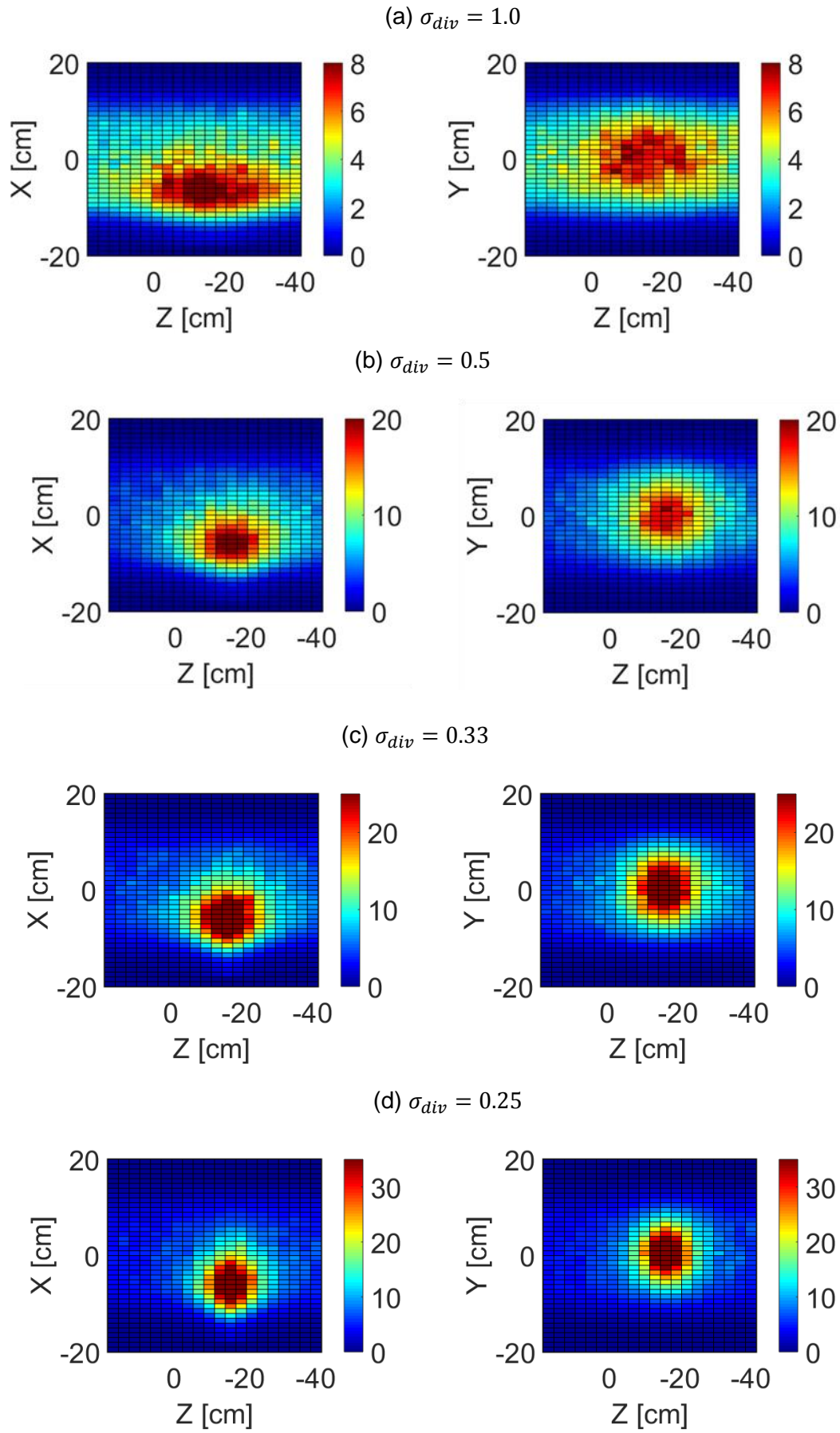
(c) $\sigma_{div} = 0.33$

(d) $\sigma_{div} = 0.25$

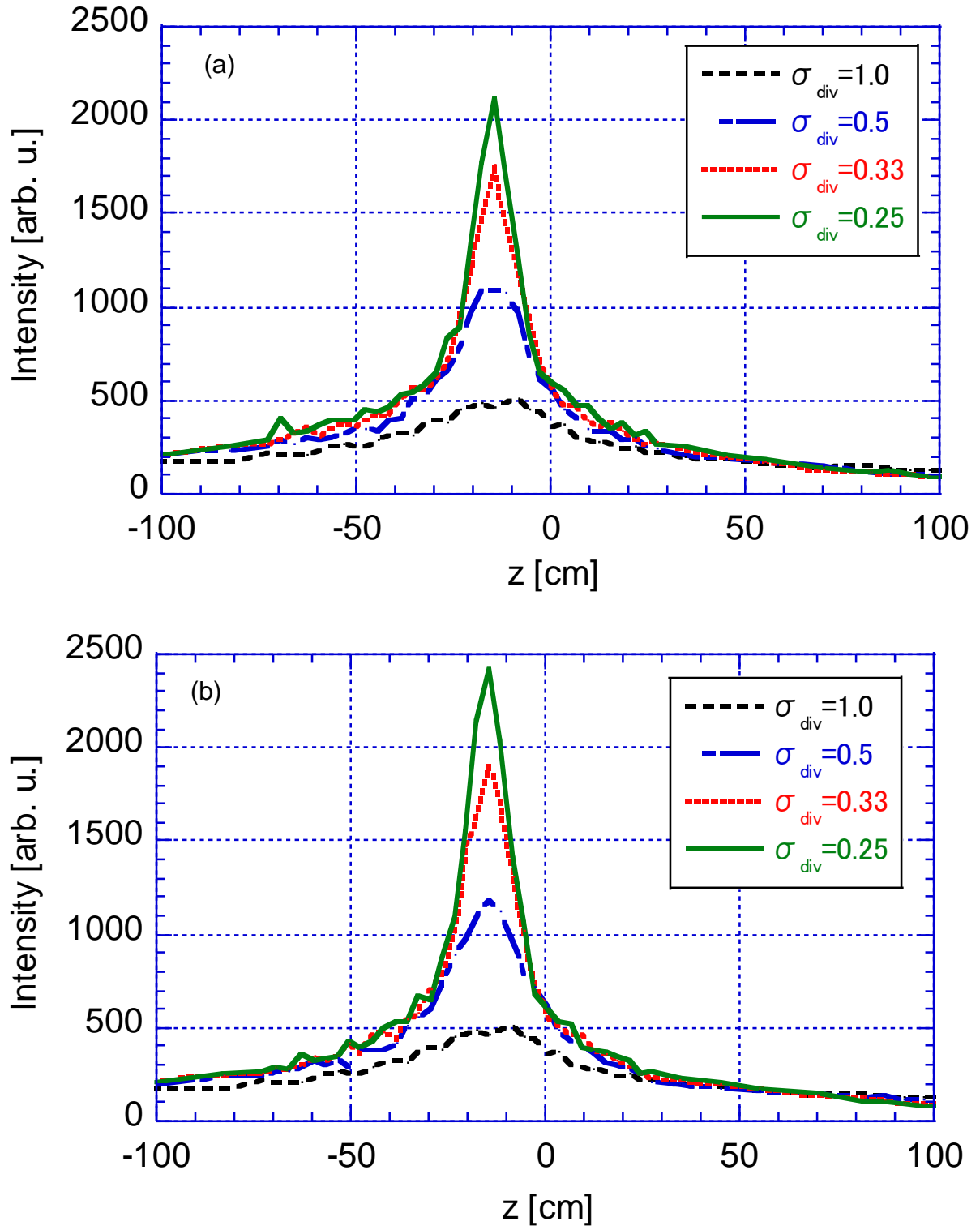Fig.5.11 2D Hα image calculated by DEGAS code at different divergence angle index.

Fig.5.12 Distribution of Hα emission intensity at different divergence angle, (a) without energy conservation, (b) with energy conservation.

5.3 Comparison between Experimental and Simulation Results

From the above results, it is found that the experimental results of the image captured by high-speed camera during SMBI with Laval nozzle can be reproduced by the simulation. Two-dimensional images are captured at the peak emission intensity as shown in Fig. 5.13(a) and Fig. 5.13(b) shows the 2-D image calculated by DEGAS simulation. Figure 5.14 shows the distribution of emission intensity along x-axis of the horizontal direction 2-D image captured by high-speed camera. From this figure it is observed that the penetration depth corresponds to 7 pixels. From the high-speed camera data, we observed that 24 pixels corresponds to 36 cm central-limiter diameter. Therefore, 7 pixels corresponds to 10.5 cm which is close to the simulation result (~11 cm). In the simulation results, the FWHM value is calculated for each divergence angle index case from Fig. 5.12(b). The FWHM value decreases with the reduction of divergence angle index as shown in Fig. 5.15. The vertical-line hatched zone and horizontal-line hatched zone in Fig. 5.15 show the region of FWHM value obtained from the experimental results in the case of only valve and with Laval nozzle, respectively. It is observed that the plenum pressure correlate with the divergence angle index. In the experimental results in the case of SMBI with only valve, the FWHM value lies in the range between the divergence angle index 0.92 to 0.5. Therefore, the SMBI experiment without nozzle case should be modeled at the initial condition between 0.92 and 0.5. In the Laval nozzle case, experimental results in saturated region (~20 cm) well agreed with divergence angle index 0.33. Therefore, SMBI experiment with Laval nozzle should be modeled at initial condition of σ_{div} = 0.33 to reproduce the experimental results.
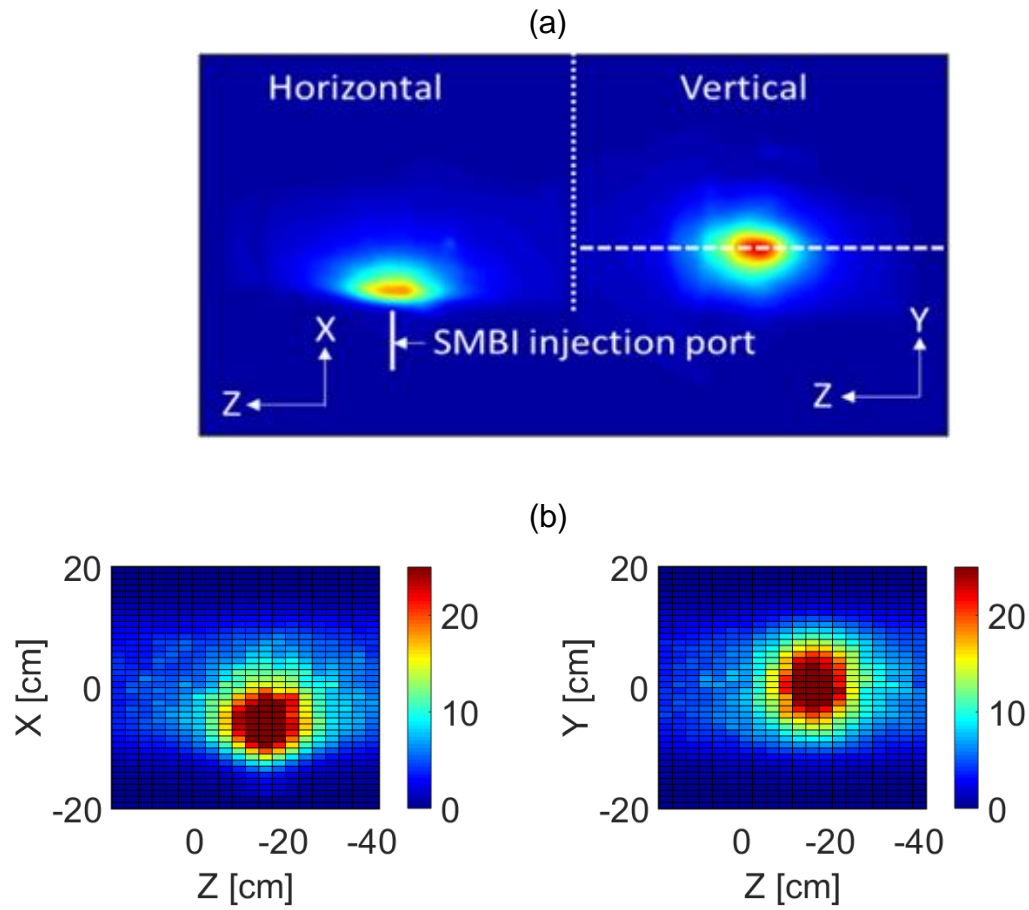
(a)

Fig.5.13 (a) 2-D image captured high-speed camera, (b) 2-D image calculated by DEGAS
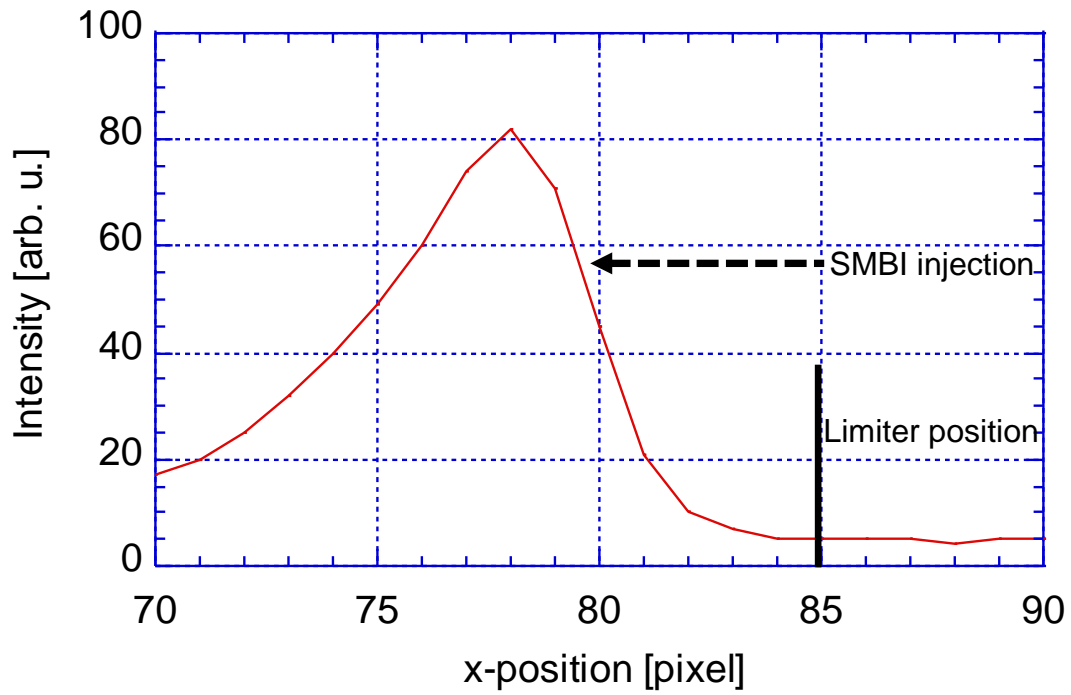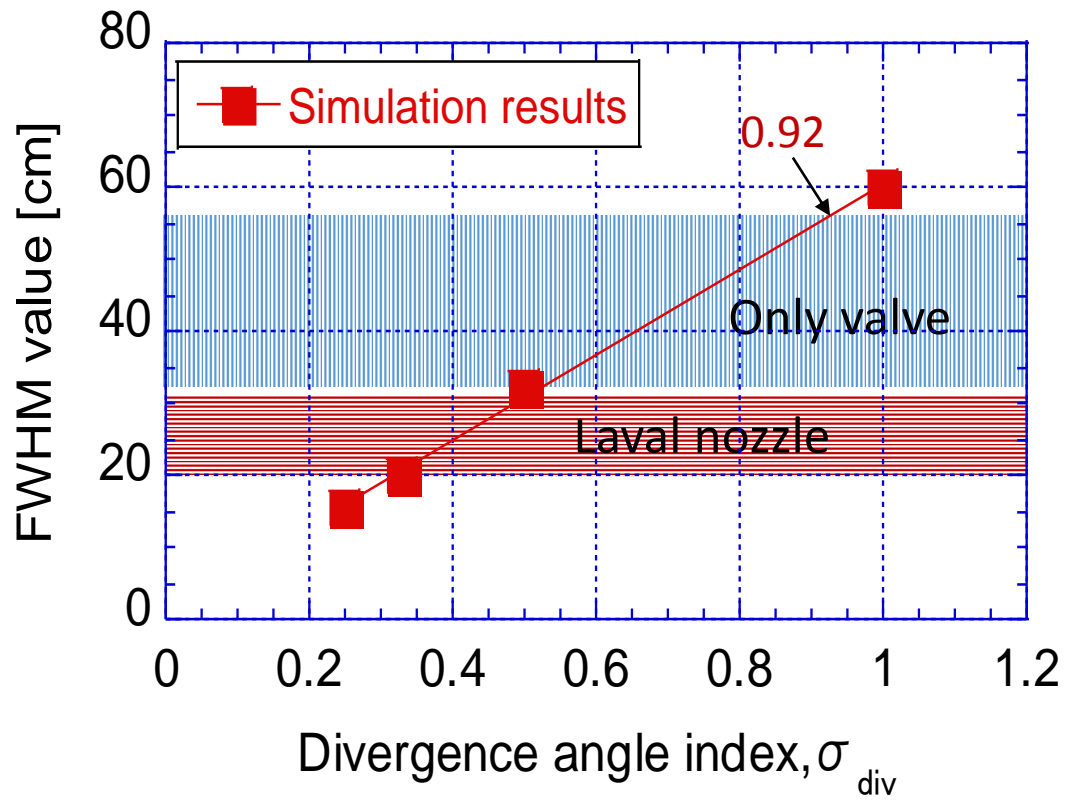

Fig.5.14 determination of penetration depth.

Fig.5.15 variation FWHM value with divergence angle index and comparison with experimental results.

5.4 Results by Varying Background Plasma Parameter

From above simulation results, it is observed that the experimental results well agreed with simulation results at divergence angle index, σ_{div} = 0.33. We also observed that the penetration depth is independent of divergence angle index. Therefore, we fixed the divergence angle index σ_{div} = 0.33 at which the value of divergence angle index well agreed to experimental results and change the background plasma parameter.

The lifetime of the neutral particles in a fusion device are a function of their velocities and the mean free path length of interaction with plasma. Assuming the ion density is equal to the electron density, the mean free path length is a function of the electron density ne, the reaction rates of the charge exchange $< \sigma v >_{CX}$ and electron impact ionization $< \sigma v >_{ion}^{e}$ as follows,

$$\lambda_p = \frac{v}{n_e(< \sigma v >_{ion}^{e} + < \sigma v >_{CX})},$$

where v is the velocity of the neutral particles. Considering a function of the mean free path length, the reaction rate depends on the electron temperature. It has been reported that SMBI has an additional effect of plasma edge cooling [24]. Therefore we carried out the simulation in different electron temperature profile.

The electron temperature profile used in this simulation as shown in Fig. 5.16. The simulation was carried out in the five different electron temperature (10 eV, 15 eV, 20 eV, 40 eV and 80 eV) in order to investigate the spatial distribution. The cross-sectional profiles of molecular hydrogen density is obtained from the simulation by changing the background electron temperature are shown in Fig. 5.17 at Z = -14.5 cm, -17.5 cm and -20.5 cm with T_e = 80 eV, 40 eV and 15 eV. When T_e = 80 eV, the molecules are localized at the bottom of the plasma. However, the molecules are spread radially as well as towards the core region in the case of low electron temperature.

The distribution of the Hα emissivity on the plasma cross-section with different background electron temperature are shown in Fig. 5.18 at different distances from the injection point Z = - 14.5 cm, -17.5 cm and -20.5 cm for T_e = 80 eV, 40 eV and 15 eV. As shown in the figure 5.18, neutral particle ionized in peripheral region was decreased in the case of low electron temperature. On the basis of this result, we evaluate the penetration depth. Figure 5.19 shows the simulation results of the penetration depth. As the electron temperature decreases, the penetration depth increases. This result indicates that radial electron profile significantly influences the penetration depth. Besides, plasma edge cooling of another effect of SMBI is a key point of clarifying the mechanism of penetration depth.

The two-dimensional images (x-z or y-z) calculated by DEGAS by changing the background electron temperature is shown in Fig. 5.20. for T_e = 80 eV, 40 eV and 15 eV. Hα emission in smaller area is observed in the case with low electron temperature. From this figure it is observed that the emission intensity reduces when electron temperature is decreased. However, the emission area shifts towards the core region. The axial distribution of Hα emission near the SMBI injection port is shown in Fig. 5.21(a). The Hα intensity peak value reduces with decrease of background electron temperature. The FWHM value is evaluated from the axial distribution of Hα emission for each background electron temperature. The variation of FWHM value with electron temperature is shown in Fig. 5.21(b). From this figure it is observed that the FWHM value decreases with increase of electron temperature. Similar results was found in the SMBI experiments with additional heating by ECRH.
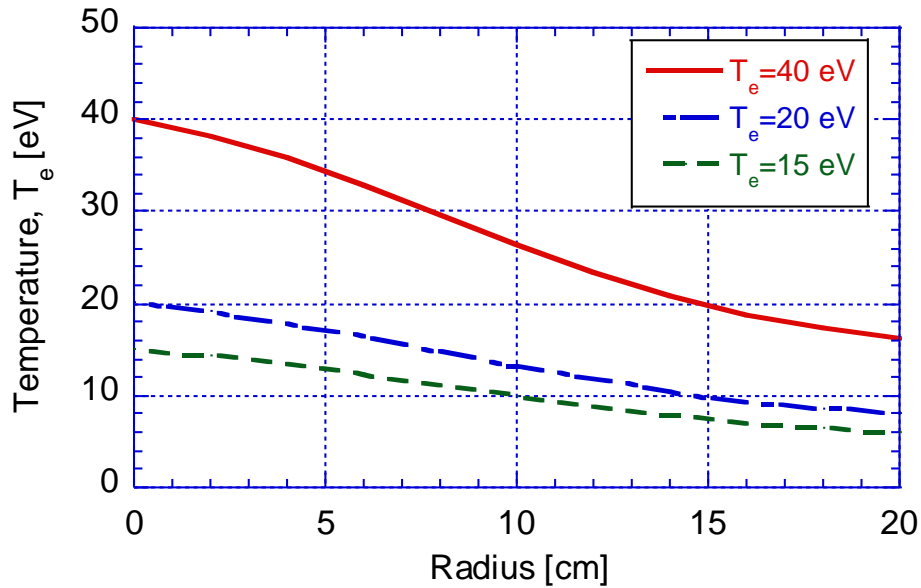
Fig.5.16 Radial profile of electron temperature, T_e.
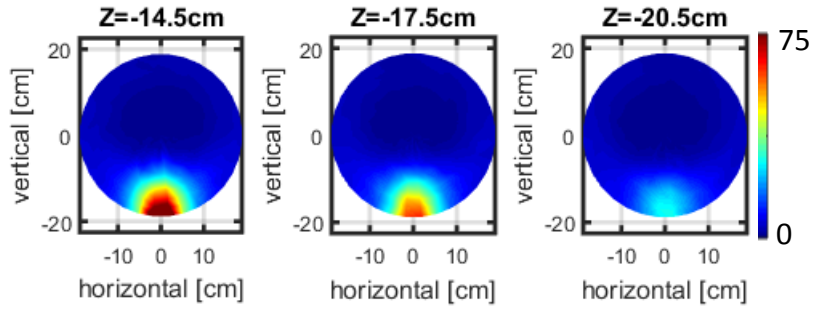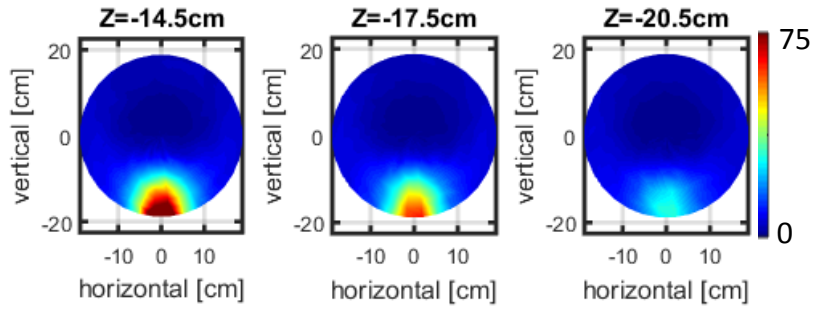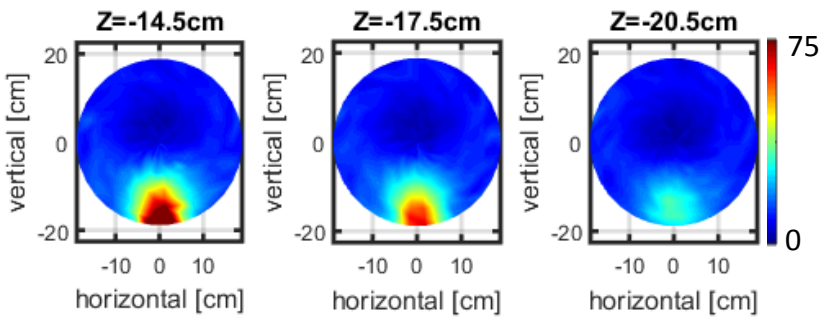
Fig.5.17 cross-sectional molecular hydrogen density profile in the case of $T_e = 80 \ eV, 40 \ eV$ and $15 \ eV$.
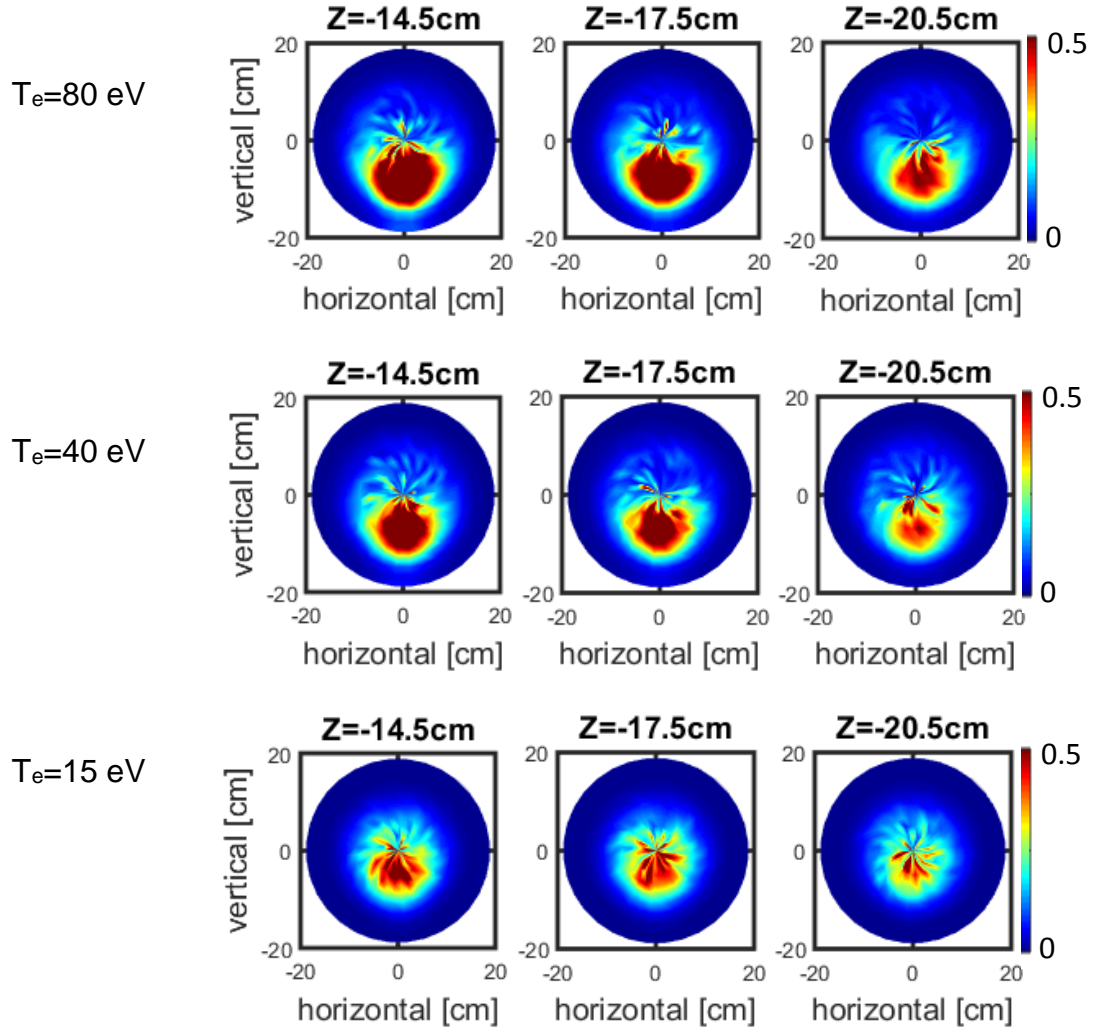
Fig.5.18 Cross-sectional view of Hα line emission at different distances from the SMBI injection position for different T_e.
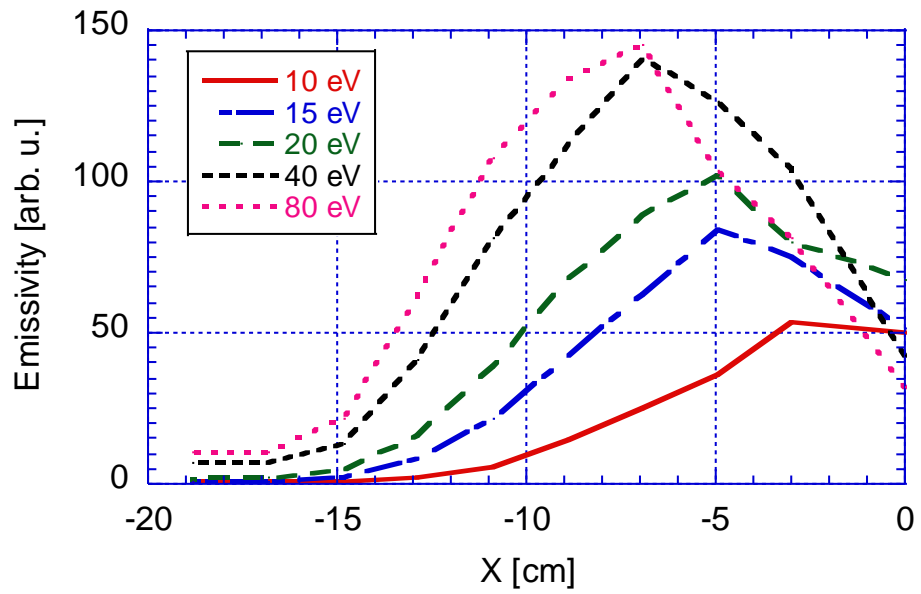
Fig.5.19 Evaluation of penetration depth in by changing background plasma parameter, T_e.
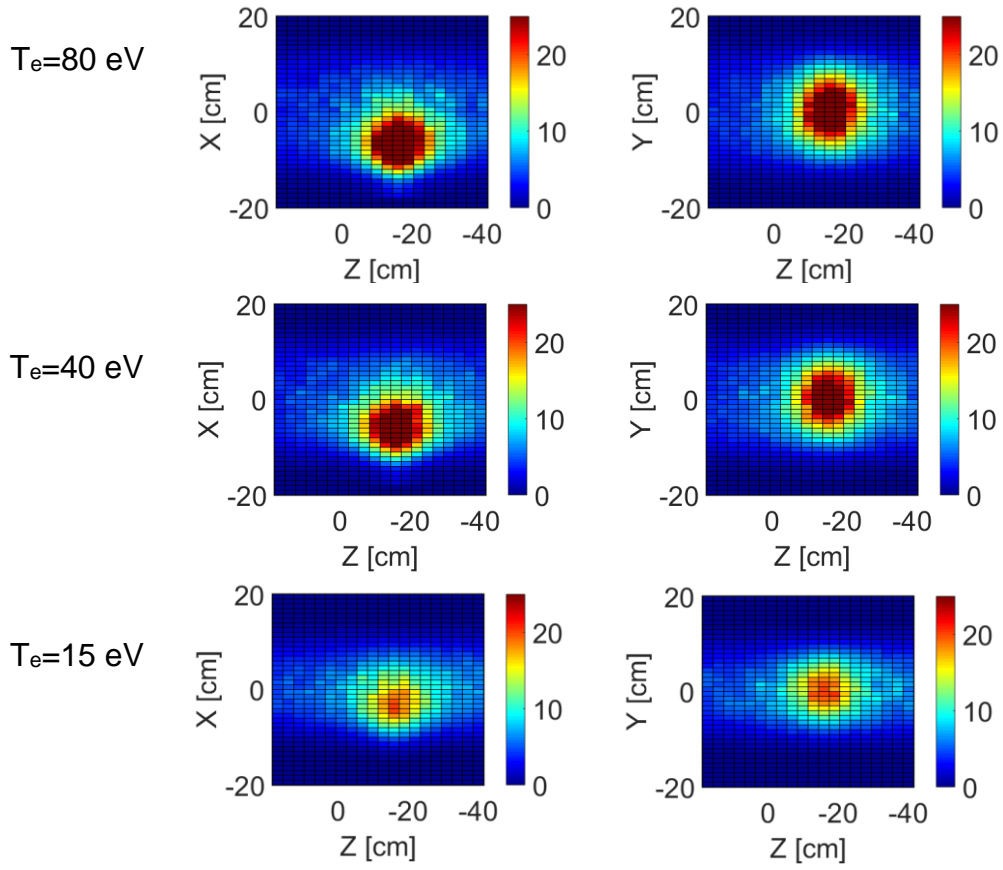
Fig. 5.20 2D Hα image calculated by DEGAS code at different electron temperature.
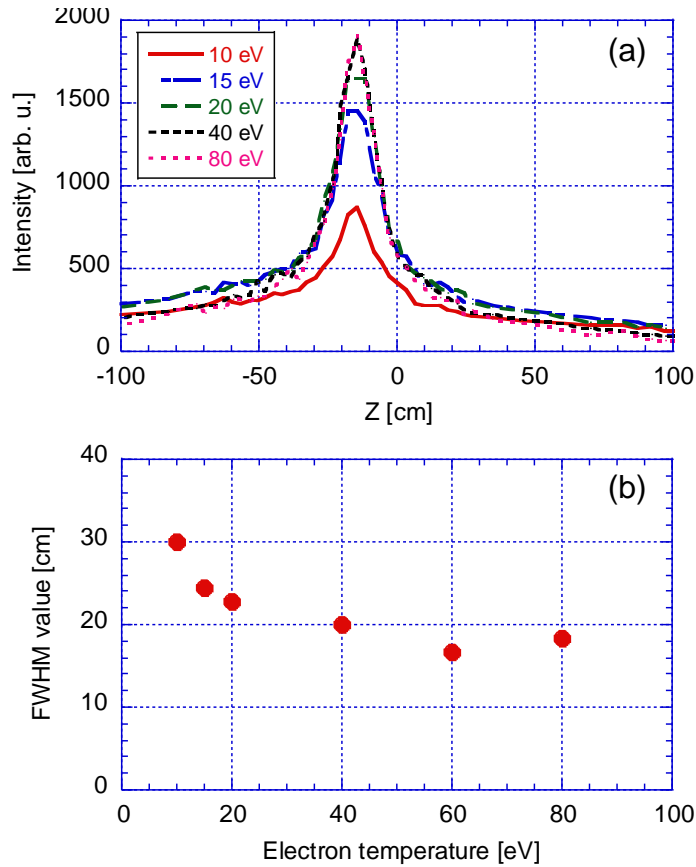
Fig.5.21 (a) Distribution of Hα emission intensity, (b) variation of FWHM value with T_e.

Chapter 6
Conclusion

In this study, we investigate the fueling characteristics and the related neutral particle behavior during SMBI in the central-cell and east anchor transition region in GAMMA 10. In the SMBI experiments in the central-cell (CC-SMBI), the characteristics of SMBI with the Laval nozzle are compared with the other nozzle in order to clarify the effectiveness of the nozzle. SMBI experiment in the east inner-transition region (EA-SMBI) in GAMMA 10 is carried out and compared with CC-SMBI results for the first time. The fully three-dimensional Monte-Carlo simulation code (DEGAS ver.63) is employed in order to understand the spatial distribution of neutral particles during SMBI. The summary of the thesis is given bellow.

Experimental Summary

In the central-cell of GAMMA 10, SMBI experiments is carried out in ion cyclotron range of frequency (ICRF) heated plasmas and those with simultaneous injection of ECRH by using a Laval nozzle. The pulse width is usually 0.5 ms and plenum pressure is varying from 0.3 MPa to 2.0 MPa throughout experiments. In the case of only ICRF heated plasma, the response of gas fueling by SMBI to the electron line-density and Hα line emission is investigated by changing the SMBI plenum pressure. At high plenum pressure (~ 2 MPa), the increase in electron line-line density was almost doubled. Since both the change in electron line-density (ΔNLcc) and Hα-line emission intensity (ΔI$_{Ha}$) increase to SMBI plenum pressure, the particle fueling rate by SMBI is proportional to the plenum pressure in this operation range. The directivity of the gas fueling by SMBI is investigated by the 2-D image captured by the high-speed camera. The full width at half maximum (FWHM) of the distribution of emission during SMBI is calculated using the image from the top view and it is an index of the directivity of gas fueling system. In the case of Laval nozzle, remarkable reduction of FWHM value is observed. Since the FWHM value of the Laval nozzle is smaller than that of straight nozzle, the directivity of Laval nozzle is better.

The gas puffing (GP) is also performed to compare with SMBI results. The experimental results show that the electron line-density is higher during SMBI than that of the gas puffing. On the other hand, the Hα intensity is low and become steeper during SMBI than the gas puffing. It indicates that SMBI with Laval nozzle is more efficient than gas puffing.

SMBI inputs a large amount of gas within a short period of time and increases the plasma density in the central-cell. Therefore, more ions flow into the end-cells. In GAMMA 10, electron cyclotron resonance heating (ECRH) is applied at plug/barrier-cells in order to form the axial confinement potential. Therefore, P/B-ECRH is applied to plug the particles that are escaped from central-cell to end-cells during SMBI. From the experimental results, it is observed that the increase in electron line-

density is higher than that of without P/B-ECRH in all plenum pressure case. It implies that the particles are confined in the central-cell due to the potential formation by the P/B-ECRH injection in the plug/barrier region. Hα-line emission intensity is also increased due to the enhancement of ionization during SMBI with P/B-ECRH. The change in electron line density is almost proportional to the change in the Hα intensity whose sightline observes the SMBI gas. These results indicate that the particle source produced by SMBI has a contribution to the increase in the electron density without saturation under the present experimental condition. The end-loss ion current is measured during by end loss ion energy analyzer (ELIEA) which is installed on both end sides in GAMMA 10. The end-loss ion current is increased during SMBI. When P/B-ECRH is used during SMBI the end-loss ion current is suppressed and increases the plasma density in the central-cell. It might be due to the formation of plug and thermal barrier potential by P/B-ECRH in the plug/barrier region. However, SMBI at high plenum pressure (~ 2.0 MPa), the P/B-ECRH could not suppressed the end loss current remarkably. It may be speculated that the plug/barrier potential is reduced due to a large amount of gas injected at high plenum pressure in the central-cell.

In order to investigate the fueling characteristics of SMBI, new type SMBI is installed in the east-anchor inner-transition region (EA-SMBI) in GAMMA 10. The SMBI plenum pressure and pulse width dependence of plasma behavior is performed in the EA-SMBI experiment. The experiential shows that the change in electron line density and Hα-line emission intensity increases linearly with plenum pressure (0.3 MPa ~ 2.0MPa). On the other hand, the pulse width dependence of EA-SMBI results shows that the line-density as well as Hα-line emission intensity increases with the SMBI pulse width. However, at longer pulse width, the line-density and Hα emission is saturated. By comparing both CC-SMBI and EA-SMBI results it is observed that the plenum pressure dependence of change in electron line-density is slightly higher in the case of CC-SMBI at high plenum prssure.

In the central-cell SMBI experiment, the diamagnetism (DMcc) is decreased during SMBI. The bottom value of DMcc almost constant in all plenum pressure (0.3 MPa ~ 2.0 MPa). This is due to the increase in the charge exchange (CX) energy loss of the hot ions produced by ICRF. On the hand, in the EA-SMBI, the diamagnetism is decreases gradually with the increase of plenum pressure and pulse width. At the longer pulse operation (2 ms) the bottom value of DMcc is low compared with the higher plenum pressure (2.0 MPa). On the other hand, the increase of the electron line-density is high in the case of high plenum pressure compared with long pulse width. It implies that SMBI with high plenum pressure is more effective than longer pulse width. The reduction of diamagnetism during EA-SMBI may be due to the degradation of ICRF heating efficiency because there is no Hα emission is observed in the central-cell during EA-SMBI.

The fueling efficiency, η is estimated in the central-cell SMBI experiments. The fueling efficiency during SMBI experiments is defined as the ratio of the increase in plasma electron contents to the injected particles by SMBI. The fueling efficiency during SMBI is about 23% and SMBI with ECRH is about 31%. The electron temperature is increased during ECRH injection and high Hα emission intensity is observed during SMBI due to the enhancement of ionization. It is also observed that the electron line-density in the central-cell is higher in the case of ECRH injection due to potential

formation by ECRH. Therefore, the fueling efficiency is increased during SMBI with ECRH. The obtained fueling efficiency in GAMMA 10 is almost near to the value of other devices like LHD, JT-60U, Tore Supra, ASDEX-U, EAST tokamak, etc.

Simulations Summary

The neutral transport simulation is successfully applied to GAMMA 10 in order to investigate precisely the spatial distribution of neutral particle behavior during SMBI. To simulate the molecular beam injected by SMBI, σ_{div} is introduced as an index the divergence angle of the initial particle. When the value of divergence angle index is less than unity, the divergence of launched particles is reduced. The axial and radial profile of neutral transport is investigated for different value of divergence angle index. The perpendicular velocity component of the initially injected particle is reduced in the case of $\sigma_{div} < 1.0$. The parallel component of the velocity along the fueling direction is modified to conserve the energy and the results are compared after velocity modification. The simulation results well explains the GAMMA 10 SMBI experimental results with Laval nozzle at divergence angle index 0.33.

The simulation results well explained the experimental results after velocity modification based on energy conservation. It is found that the particles are suppressed and localized in the injection point according to the reduction of divergence angle index, σ_{div}. The neutral particles behavior have been shown a clear dependence on the initial particle source. When the value of initial particle source is reduced, the simulation results are mostly similar with the experimental results. We also evaluated the penetration depth of SMBI-induced particles and it is clarified that the penetration depth has no dependence on the directivity of the particles from the radial distribution of Hα emissivity in the plasma cross-section.

The simulation is also carried out in the different profiles of electron temperature in order to check the sensitivity of the background plasma parameter. The simulation results indicates that the penetration depth depended on the background plasma parameter, electron temperature. The penetration depth increases with the decrease of electron temperature. The radial and axial distribution of Hα emission area shifts towards the core region in the case of low electron temperature. The FWHM value decreases with increase of background electron temperature. This results well explains the SMBI experimental results with additional heating by ECRH.

Concluding Remark

The fueling characteristics by SMBI is investigated by both experiments and simulations. Better directivity is clarified in the case of SMBI with Laval nozzle. The enhancement of ionization and confinements of particles during SMBI with additional heating ECRH leads to the improvement of the fueling efficiency.

In the simulation, the code is modified in order to conserve the energy of the initial particles. SMBI experimental results with Laval nozzle is well agreed with the simulation results after energy conservation. It is also observed that the penetration depth depends on the background plasma parameter.

From the above results, the fueling characteristics by SMBI with Laval nozzle obtained in experiments and neutral transport simulations during SMBI will be useful for developing the fueling study. These results also enable us to analyze in detail the neutral particle behavior without dependence of the fueling method. The beneficial knowledge obtained from this study may contribute for the optimization of fueling in future plasma confinement devices such as ITER and DEMO.

Acknowledgements

Appendix A

Theory of Supersonic Gas Flow and Design of Laval Nozzle

A.1 Theory of Supersonic Gas Flow

Supersonic gas flow is produced by a "Laval nozzle". The theory of supersonic gas flow is described below [47].

The stream-tube, where the cross section area A to vary with distance x, is assumed, as illustrated in Fig. A.1. The steady flow, where the cross-section area, A, the pressure, p, the density, n_f, and the velocity, v are functions of x only, is defined as quasi-one-dimensional flow. One the other hand, in the case of one-dimensional flow that is treated as strictly constant-area flow, three physical mechanisms, such as a normal shock, heat addition and/or friction, cause the flow properties to change with x even though the area constant [48]. Although the actual physical flow through the variable-area duct is three-dimensional, in the case of quasi-one-dimensional flow, the flow properties described as a function of x. This is due to assuming that the flow properties are uniform across any given cross section of area A. The quasi-one-dimensional flow is an approximation to the actual physics of the flow.

In order to steady quasi-one-dimensional flow, the continuity equation is derived from the integrated calculation over the control volume, as follows,

$$-\oiint_S n_f \, V.dS = \frac{\delta}{\delta t} \iiint_V n_f \, dV \, , \tag{A.1}$$

when integrated over the control volume in Fig. A.1 leads, for steady flow, directly to

$$n_{fi}v_i A_i = n_{fii}v_{ii}A_{ii}. \tag{A.2}$$

In Eq. (A.2) the term $n_{fi}v_i A_i$ is the surface integral over the cross-section at location 1 and $n_{fii}v_{ii}A_{ii}$ is th surface integral over the cross-section at location 2. The surface integral taken over the side of the control surface between location 1 and 2 is zero, because the control surface is a stream tube. Hence V is assumed oriented along the surface and hence $V.dS = 0$ along the side.

From Eq. (A.2),

$$n_f vA = constant. \tag{A.3}$$

Hence,

$$d(n_f vA) = 0. \tag{A.4}$$

The momentum equation for steady quasi-one-dimensional flow is estimated from the integral form of the momentum equation, assuming steady flow and no body forces, as follows,

$$\oiint_S \left(n_f \, V.dS\right)V + \iiint_V \frac{\delta\left(n_f V\right)}{\delta t} dV = \iiint_V n_f f \, dV - \oiint_S p \, dS \,, \tag{A.5}$$

$$p_i A_i + n_{fi} v_i^2 A_i + \int_{A_i}^{A_{ii}} p dA = p_{ii} A_{ii} + n_{fii} v_{ii}^2 A_{ii}. \tag{A.6}$$

In order to obtain a differential form of the momentum equation, apply Eq. (A.6) to the infinitesimal control volume sketched in Fig. A.2 where the length in the x-direction is dx:

$$pA + n_f v^2 A + n_f v^2 A + n_f dA = (p + dp)(A + dA) + (n_f + dn_f)(v + dv)^2 (A + dA). \tag{A.7}$$

Dropping all second order terms involving products of differentials, this becomes

$$Adp + Av^2 dn_f + n_f v^2 dA + 2n_f vA dv = 0. \tag{A.8}$$

Expanding Eq. (A.4), and multiply by v,

$$n_f v^2 dA + n_f vA dv + Av^2 dn_f = 0. \tag{A.9}$$

Subtracting this from Eq. (A.8), we obtain

$$dp = -n_f v dv. \tag{A.10}$$

From Eq. (A.4),

$$\frac{dn_f}{n_f} + \frac{dv}{v} + \frac{dA}{A} = 0. \tag{A.11}$$

To eliminate dn_f/n_f from Eq. (A.11) consider Eq. (A.10)

$$\frac{dn_f}{n_f} = \frac{dp}{dn_f}\frac{dn_f}{n_f} = -v dv. \tag{A.12}$$

There are no dissipative mechanisms such as friction, thermal conduction, or diffusion acting on the flow. Thus, the flow is isentropic. Hence, any change in pressure, dp, in the flow is accompanied by a corresponding isentropic change in density, dn_f. Therefore, we can write,

$$\frac{dp}{dn_f} = \left(\frac{\partial p}{\partial n_f}\right)_s = v_s^2, \tag{A.13}$$

where v_s is the sound speed. Eq. (A.13) is a fundamental expression for the speed of sound. Combining Eqs. (A.12) and (A.13),

$$v_s^2 \frac{dn_f}{n_f} = -v dv,$$

$$\frac{dn_f}{n_f} = -\frac{v \, dv}{v_s^2} = -\frac{v^2 \, dv}{v_s^2 v} = -M^2 \frac{dv}{v}, \tag{A.14}$$

where M is the Mach number which is defined as $M = v/v_s$. Substituting Eq. (A.14) into Eq. (A.11),

$$\frac{dA}{A} = (M^2 - 1)\frac{dv}{v}. \tag{A.15}$$

This equation is called the area-velocity relation and significant equation. It tells us this information:

1. $M \to 0$ (Incompressible flow)

$$\frac{dA}{A} = -\frac{dv}{v}.$$

$$Av = const.$$

This is the familiar continuity equation for incompressible flow.

2. $0 \leq M \leq 1$ (Subsonic flow)

$$\frac{dA}{A} = -C\frac{dv}{v} \ (C > 0).$$

$$dA > 0 \Rightarrow dv > 0$$

$$dA < 0 \Rightarrow dv < 0.$$

The velocity increases in a converging duct and decreases in a diverging duct.

3. $M > 1$ (Supersonic flow)

$$\frac{dA}{A} = C\frac{dv}{v} \ (C < 0).$$

$$dA > 0 \Rightarrow dv > 0$$

$$dA < 0 \Rightarrow dv < 0.$$

The velocity increases in a diverging duct and decreases in a converging duct.

4. $M = 1$ (Sonic flow)

$$\frac{dA}{A} = 0.$$

From the above results, the flow with the speed of the subsonic becomes supersonic speed flow when the flow passes through a minimum radius of the area which is called throat. In contrast, the supersonic flow becomes the subsonic flow when the flow passes through the throat as shown in Fig.

A.3. That is, in order to obtain the supersonic speed, it is necessary to pass through the throat. "Laval nozzle" is the nozzle to achieve supersonic flow using this property. Next, a relation equation of the area and Mach number in nozzle is shown as follows. Consider the duct shown in Fig. A.4. At the throat, the flow is sonic. Hence, denoting conditions at sonic speed by an asterisk, we have $M^* = 1$ and $v^* = v_s^*$ at the throat. The area of the throat is A^*. At any other section of the duct, the local area, Mach number, and velocity are A, M, and v, respectively. Apply Eq. (A.2) between these two locations:

$$n_f^* v^* A^* = n_f v A, \tag{A.16}$$

Since $v^* = v_s^*$, Eq. (A.16) becomes

$$\frac{A}{A^*} = \frac{n_f^*}{n_f} \frac{v_s^*}{v} = \frac{n_f^*}{n_{f0}} \frac{n_{f0}}{n_f} \frac{v_s^*}{v}, \tag{A.17}$$

where n_{f0} is the stagnation density, $An_{f0} = p_s / R_G T_s$, and is constant throughout the isentropic flow. The ratio of total to static density at a point in the flow as a function of Mach number M at that point is given as follows [49],

$$\frac{n_{f0}}{n_f} = \left(1 + \frac{\gamma-1}{2} M^2\right)^{1/(\gamma-1)}, \tag{A.18}$$

And apply this to sonic conditions, we have

$$\frac{n_{f0}}{n_f^*} = \left(\frac{\gamma+1}{2}\right)^{1/(\gamma-1)}. \tag{A.19}$$

Also, by definition, and from a direct relation between the actual Mach number M and the characteristics Mach number M^*,

$$\left(\frac{v}{v_s^*}\right)^2 = M^{*2} = \frac{\frac{\gamma+1}{2} M^2}{1 + \frac{\gamma-1}{2} M^2}. \tag{A.20}$$

Squaring Eq. (A.17), and substituting Eqs. (A.18), (A.19), and (A.20), we have

$$\left(\frac{A}{A^*}\right)^2 = \left(\frac{n_f^*}{n_{f0}}\right)^2 \left(\frac{n_{f0}}{n_f}\right)^2 \left(\frac{v_s^*}{v}\right)^2,$$

$$\left(\frac{A}{A^*}\right)^2 = \left(\frac{2}{\gamma+1}\right)^{2/(\gamma-1)} \left(1 + \frac{\gamma-1}{2} M^2\right)^{2/(\gamma-1)} \left(\frac{1 + \frac{\gamma-1}{2} M^2}{\frac{\gamma+1}{2} M^2}\right),$$

$$\frac{A}{A^*} = \frac{1}{M} \left[\frac{2}{\gamma+1}\left(1 + \frac{\gamma-1}{2} M^2\right)\right]^{(\gamma+1)/2(\gamma-1)}, \tag{A.21}$$

Equation (A.21) is called the area-Mach number relation. The Mach number at any location in the duct is a function of the ratio of the local duct area to the sonic throat area.

A.2 Design of Laval Nozzle

The Laval nozzles is designed referring to NACA technical note [50]. Especially, a part of method of Foelsch was used in this design. Design of Laval nozzle is divided into three sections. First section is upstream of the throat. This section is arbitrary curved line. Other two sections are important for the Laval nozzle. Second section is called expansion section where expansion wave is generated and propagate across the flow downstream reflecting from the opposite wall. Third section is called straightening section where all the expansion waves generated by the expansion section are canceled. The point of junction of the expansion section and straightening section is called an "inflection point". The angle of the duct wall at inflection point is largest in the all section of the Laval nozzle as shown in Fig. A.5.

Before design, the diameter of throat, d, the Mach number of the design value, M_t and the angle of the inflection point, θ_1 were determined. Typical design parameters of Laval nozzle for SMBI are $d = 0.6$ mm, $M_t = 11.5$ and $\theta_1 = 12.5°$, respectively.

Firstly, the design of the expansion section is described. Although the curve line of the expansion section is also arbitrary, the coordinate at inflection point, (x_1, y_1), have to be determined. The cross section area at the throat, A^* is πy^{*2}, where y* denotes the radius of throat. The streamline through (x_1, y_1) is radial surface. The cross section area of the radial surface, A_1, is as follows,

$$A_1 = 2\pi r_1^2 (1 - cos\theta_1), \tag{A.22}$$

From Fig. A.6,

$$r_1 sin\theta_1 = y_1, \tag{A.23}$$

$$\frac{A_1}{A^*} = \frac{2r_1^2}{y^{*2}}(1 - cos\theta_1). \tag{A.24}$$

Hence,

$$y_1 = y^* \sqrt{\frac{A_1}{A^*} \frac{sin^2\theta_1}{2(1-cos\theta_1)}}. \tag{A.25}$$

This is the *y*-coordinate of the inflection point. However, A_1/A^* is unknown now. When the nozzle is axial symmetry, the velocity at the inflection point, v_1 is related to θ_1 as follows,

$$v_1 = v_t - 2\theta_1, \tag{A.26}$$

where v_t is Prandtl-Meyer function,

$$v_t = \sqrt{\frac{\gamma+1}{\gamma-1}} \, tan^{-1}\sqrt{\frac{\gamma-1}{\gamma+1}(M^2 - 1)} - tan^{-1}\sqrt{M^2 - 1}. \tag{A.27}$$

The Mach number at the inflection point, M_1, is also estimated from Eqs. (A.26) and (A.27).

$$\sqrt{\frac{\gamma+1}{\gamma-1}}\,tan^{-1}\sqrt{\frac{\gamma-1}{\gamma+1}(M^2-1)}-tan^{-1}\sqrt{M^2-1}-2\theta_1$$

$$=\sqrt{\frac{\gamma+1}{\gamma-1}}\,tan^{-1}\sqrt{\frac{\gamma-1}{\gamma+1}(M_1^2-1)}-tan^{-1}\sqrt{M_1^2-1}. \tag{A.28}$$

A_1/A^* is calculated by Eq. (A.21), substituting M_1.

$$\frac{A_1}{A^*}=\frac{1}{M_1}\left[\frac{2}{\gamma+1}\left(1+\frac{\gamma-1}{2}M_1^2\right)\right]^{(\gamma+1)/2(\gamma-1)}. \tag{A.29}$$

The curve line of the expansion section is given by the Foelsh method in Ref. [50], as a third-order function,

$$y=y^*+\frac{tan\theta_1}{x_1}x^2\left(1-\frac{x}{3x_1}\right). \tag{A.30}$$

Substituting $(x, y) = (x_1, y_1)$ to Eq. (A.30) and solving the equation for x_1,

$$x_1=\frac{3}{2}\left(\frac{y_1-y^*}{tan\theta_1}\right). \tag{A.31}$$

This is the x-coordinate of the inflection point.

Next, the design of straightening section is shown as follows. The assumptions of this method, or rather its boundary conditions, may be variously stated:

(1) Along the Mach line emanating from the inflection point, the velocity vectors are co-original,

(2) the Mach number is constant along the arc of the circle which passes through the inflection point of the wall perpendicularly (and obviously its center is the origin of the velocity vectors),

(3) in the region between this arc and the Mach line from the inflection point, the Mach number is a function solely of the radius from the vector origin.

The radius of vector at the throat, r^* is as follows,

$$r^*=\sqrt{\frac{A^*}{A_1}}r_1. \tag{A.32}$$

The minim step of the Mach number is determined as the step number of 500,

$$\Delta M = \frac{M_t - M_1}{500}, \tag{A.33}$$

where M_t is the Mach number of the design value. The angle at the point of P is estimated from next equation, substituting the Mach number,

$$\theta = \frac{v_t - v(M)}{2}. \tag{A.34}$$

The relation is given by continuity equation from Fig. A.7, as follows

$$2\pi r^2(cos\theta - cos\theta_1) = \pi[l\,sin(\theta + \alpha_0) + rsin\theta + (r + l\,cos\alpha_0)\,sin\theta]l\,sin\alpha_0, \tag{A.35}$$

where α_0 is the Mach angle at the point P. The left-hand side of this equation means the area formed by the arc between the points of P and P'. In contrast, the right-hand side of this equation means the area of side of the circular truncated cone, where the side surface is formed by the points of Q and Q'. This equation can be solved for the length between the points of P and Q, l, as follows,

$$l = \frac{2rsin\alpha_0\,sin\theta - \sqrt{4r^2sin^2\alpha_0sin^2\theta - 4(2r^2cos\theta - 2r^2cos\theta_1)(-cos\alpha_0sin\alpha_0sin\theta - sin\alpha_0sin(\alpha_0 + \theta))}}{2(-cos\alpha_0sin\alpha_0sin\theta - sin\alpha_0sin(\alpha_0 + \theta))}. \tag{A.36}$$

The coordinate, (x, y), in straightening section are determined by l,

$$x = rcos\theta + lcos(\theta + \alpha_0) + (x_1 - r_1cos\theta_1), \tag{A.37}$$

$$y = l\,sin(\theta + \alpha_0) + rsin\theta, \tag{A.38}$$

This is the points of the straightening section. We have to calculate until the end of exit hole of Laval nozzle. At the inflection point, the length of l needs to be the minimum value.

Figure A.8(a) shows cross section of the new Laval nozzle of 0.6 mm throat diameter designed for the SMBI device. This nozzle is designed to generate a gas flow of $M_t = 11.5$ and the inflection angle of 12.5°. Figure A.8(b) shows the photograph of new Laval nozzle of 0.6 mm throat diameter.
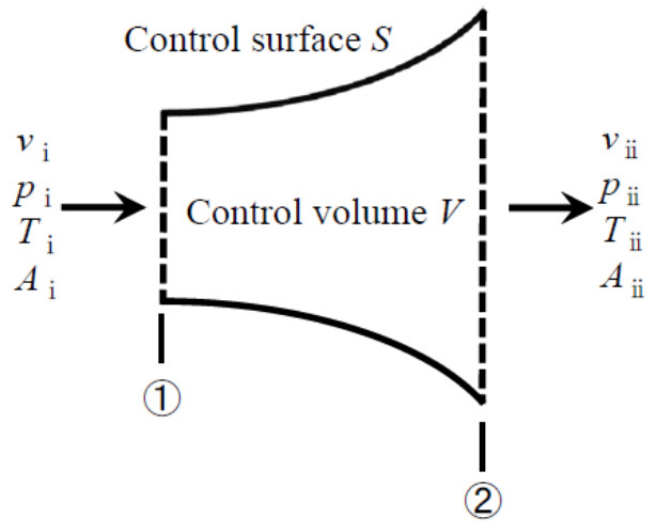
Fig.A.1 The model of quasi-one-dimensional flow.
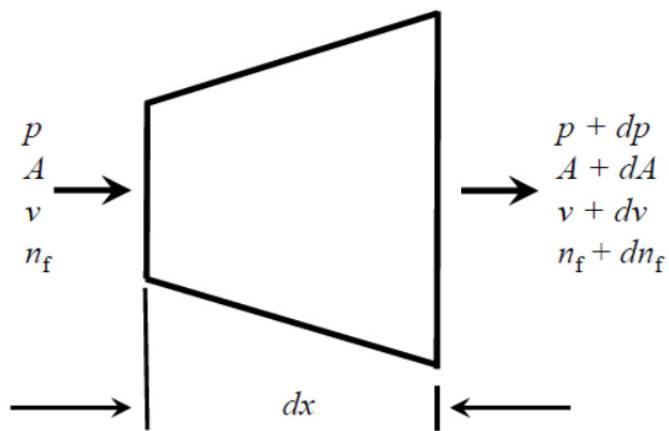
Fig.A.2 Incremental volume.
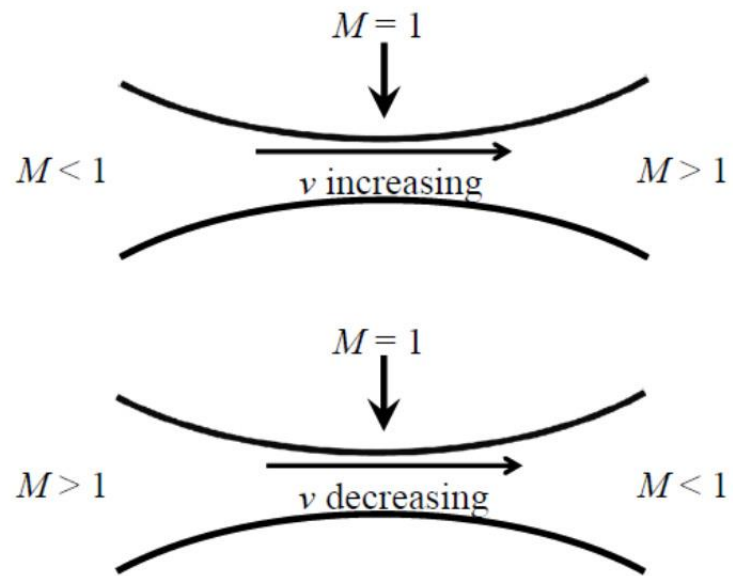
Fig.A.3 Flow in a convergent-divergent duct..
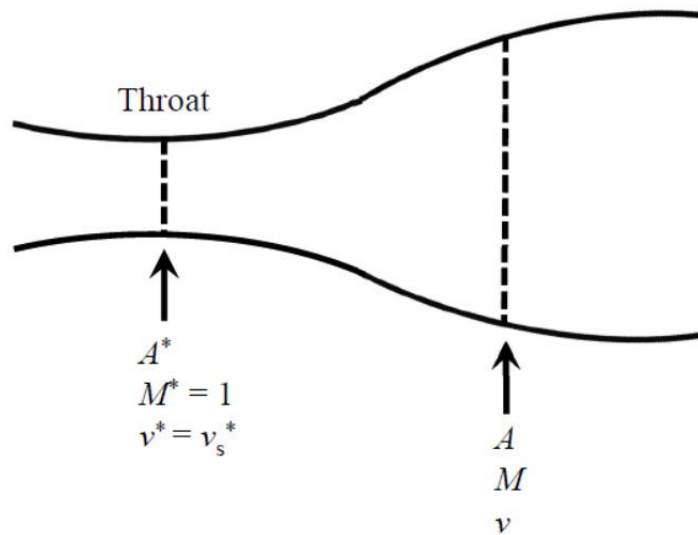
Fig.A.4 Geometry for derivation of the area Mach number relation..
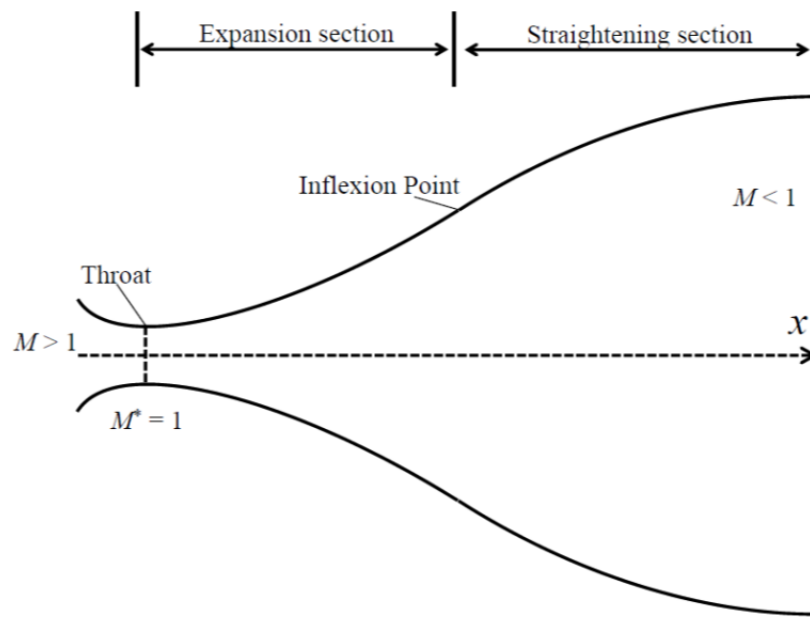
Fig.A.5 Sketch of Laval nozzle.
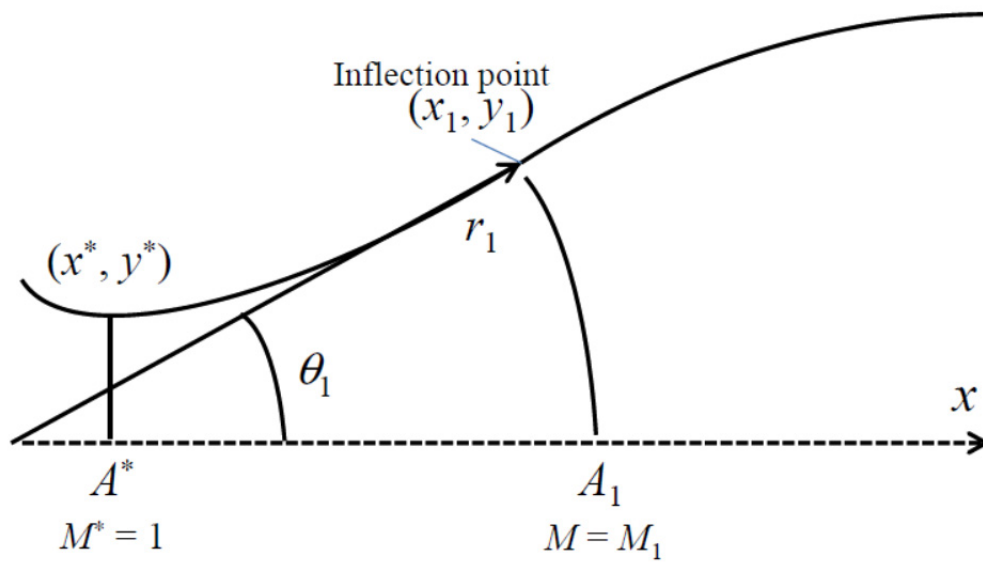
Fig.A.6 Design of expansion section.
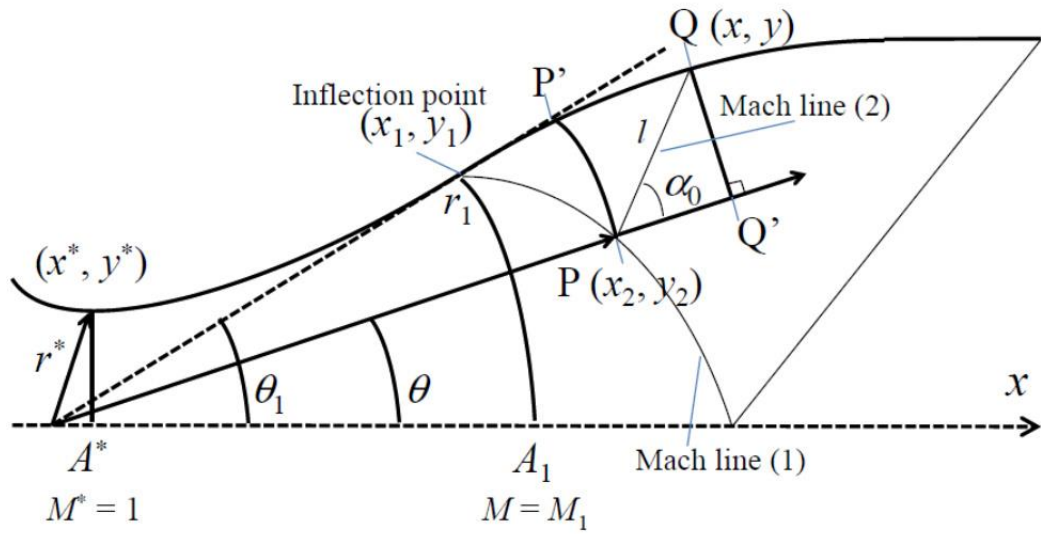
Fig.A.7 Design of straightening section.

(a)

$\phi 0.6$ mm
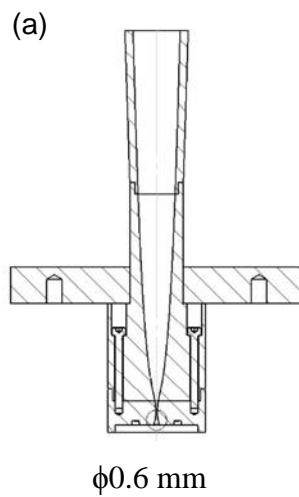
(b)
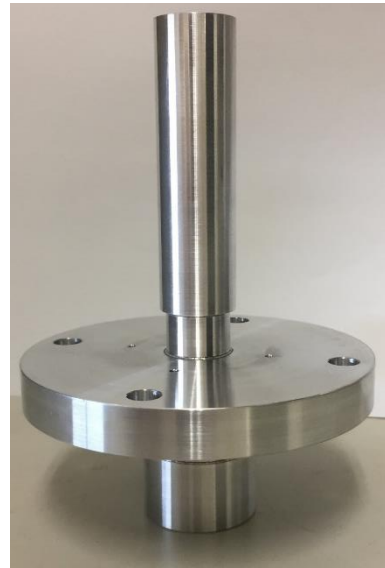
Fig.A.8 (a)Cross-section and (b) photograph of the new Laval nozzle installed in the east anchor inner-transition region in GAMMA 10 device.

Appendix B
DEGAS Code

The DEGAS is a Monte-Carlo simulation code in order to obtain the profiles of density and temperature of the neutral particles in the three-dimensional plasmas. The DEGAS code has widely been used for the evaluation of neutral transport in various machines. The computational process for the neutral density and temperature in plasma is described in this appendix.

B.1 Boltzmann Equation

The lifetimes of the neutral particles in a fusion device are a function of their velocities, the mean free path length of interaction with the plasma λ_p and the distances to the device walls l_ω. Assuming the ion density is equal to the electron, the mean free path length is a function of the electron density n_e, the reaction rates of the charge exchange $< \sigma v >_{CX}$ and electron impact ionization $< \sigma v >_{ion}^e$ as follows,

$$\lambda_p = \frac{v}{n_e(< \sigma v >_{ion}^e + < \sigma v >_{CX})} \tag{B.1}$$

where v is the velocity of the neutral particles. Then mean free path length of the particles, l_{tot} is

$$l_{tot} = \frac{\lambda_p l_\omega}{\lambda_p + l_\omega} \tag{B.2}$$

In order to obtain the neutral density and temperature in a plasma, it is assumed that the Boltzmann equation describing the neutral particle distribution $f(x, v)$ over position x, and velocity v, space is time-independent,

$$v \cdot \nabla f(x) = C(f)(x, v) \tag{B.3}$$

where $C(f)$ is the neutral-plasma collision term. For simplicity, assuming that the plasma is a slab bounded on one side by a flat wall, Eq. B.3 can be rewritten in only 1-dimension,

$$v_x \frac{\partial f}{\partial x} = C(f) \tag{B.4}$$

for $x > 0$, with one boundary condition on f, at the wall at $x = 0$,

$$f(0, v) = f_+(v) \tag{B.5}$$

In the collision term for atomic hydrogen, the electron impact ionization and charge exchange processes were included. Then the ionization term $S(f)$ in $C(f)$ is,

$$S(f) = -f(x, v) \int_\omega \|v - w\| \sigma_e f_e(x, w) dw \qquad (B.6)$$

where $fe(x, w)$ is the electron distribution function and $\| a \|$ denotes the length of the vector a. Now in general $\|w\| \gg \|v\|$, so that, assuming $f_e(x, w) = n_e(x) f_M(w)$, where f_M is a Maxwellian velocity distribution, Eq. B.6 can be rewritten as,

$$\begin{aligned} S(f)(x, v) &= -f(x, v) n_e(x) \int_\omega \|w\| \sigma_e f_M(w) dw \\ &= -f(x, v) n_e(x)_S \end{aligned} \qquad (B.7)$$

where

$$s = \int_\omega \|w\| \sigma_e f_M(w) dw \qquad (B.8)$$

The charge exchange term, $X(f)$ in $C(f)$ is,

$$X(f)(x, v) = \int \|v - w\| \sigma_{CX} [f(x, w) f_i(x, v) - f(x, v) f_i(x, w)] dw \qquad (B.9)$$

Simplifying Eq. B.9 is the fact that $\sigma_{CX} \|v - w\|$ is a slowly varying function of the relative velocity, which can then be assumed to be a constant c. Taking $f_i(x, v) = n_i(x) f_M(v)$, Eq. B.9 then becomes

$$X(f)(x, v) = n_i(x) c \left[f_M(v) \int_\omega f(x, w) dw - f(x, v) \right] \qquad (B.10)$$

Returning to Eq. B.3, assuming $ne = ni = n$, the following relation can be observed,

$$v_x \frac{\partial f}{\partial x} = S(f) + X(f)$$

$$= -fns + cn\left[f_M \int_\omega f(x,w)dw \right.$$

$$\left. - f\right] \tag{B.11}$$

$$= -fn(s+c)$$

$$+ ncf_M \int_\omega f(x,w)dw$$

It is useful to parameterize the distance variable to units, z of mean free path lengths (the optical depth),

$$z(x) = \int_0^x \frac{dy}{\lambda_{tot}(y)} = \int_\omega^x \frac{n(y)(c+s)dy}{v_{T_i}} \tag{B.12}$$

where v_{T_i} is the ion thermal velocity. With this change of variables, integrating Eq. B.11 over v_y and v_z gives,

$$u\frac{\partial F}{\partial z} + F(u,z) = \frac{c}{s+c}g(u)\int_{-\infty}^\infty F(u,z)du \tag{B.13}$$

where $u = v_y/v_{T_i}$, $F(u,z) = \iint f(x,v)dv_y d\,v_z$, and $g(u)$ is the ion velocity distribution.

To illustrate how the Monte Carlo method can be used to solve Eq. B.3, simplify Eq. B.3, for argument's sake, by assuming that no charge exchange occurs, so that the 1-dimensional version [Eq. B.13] of Eq. B.3 is

$$u\frac{\partial F}{\partial z} = -F(u,z) \tag{B.14}$$

Making the further assumption that $|u| = 1$, Eq. B.14 has the solution

$$F(x) = \exp[-z(x)]$$

$$= exp\left[-\int_0^x \frac{d_y}{\lambda_{tot}(y)}\right] \tag{B.15}$$

Now the solution Eq. B.14 can be derived from a different point of view. Let $\xi(x)$ be the probability that a particle travels at least a distance x without making a collision. The probability of traveling at least a distance $x + dx$ without making a collision is

$$\xi(x+dx) = \xi(x) - \xi(x)\,dx/\lambda_{tot}(x) \tag{B.16}$$

and solving for $\xi(x)$ gives

$$\xi(x) = exp\left[-\int_0^x \frac{ds}{\lambda_{tot}(s)}\right] \tag{B.17}$$

which is just Eq. B.15.

The Monte Carlo method of solving Eq. B.14 is to track test flights using Eq. B.17 to determine points of collision. Take a uniform random variable (URV) ξ between 0 and 1 and solve

$$\xi(x) = exp\left[-\int_0^{x(\xi)} \frac{ds}{\lambda_{tot}(s)}\right] \tag{B.18}$$

for the collision point $x(\xi)$. By running a sequence of test flights a distribution of collision points is determined and, knowing the remaining terms in $C(f)$, such as plasma density and temperature and the reaction cross-sections, the distribution function is solved.

In order to solve the integral equation Eq. B.18 for $x(\xi)$, the pseudo-collision algorithm (PCA) is used in DEGAS. Given the initial x_0 and v, let λ_m be the shortest mean free path length in the entire plasma for the test flight. Move the test flight to

$$x_1 = x_0 - ln(\xi)\lambda_{min}v_l \tag{B.19}$$

where ξ is a URV, $0 < \xi < 1$, and $v_1 = v/\|v\|$. Let $\rho = \lambda_{min}/\lambda_{tot}(x_1)$, and test for a collision: Choose a new URV, ξ_1. If $\xi_1 \leq \rho$ then a collision occurs. If $\xi_1 > \rho$ then a pseudo-collision is occurred and the procedure is repeated until a collision occurs.

B.2 Test Flight Weighting

Each test flight is initially given a weight of $\omega = 1$. If a total source of *Jatoms/s* is being modeled with N test flights, each test flight then represents $\gamma = J/Natoms/s$ at its start. As the test flight progresses through a sequence of collisions the weight is reduced to account for attenuation by ionization. This method is called suppressed absorption. ω is multiplied at each collision by the probability of charge exchange, $\rho_{CX} = 1 - \rho_{ion}$. The probability of the ionization ρ_{ion} for atomic hydrogen is represented as follows,

$$\rho_{ion} = \frac{n_e\langle\sigma v\rangle_{ion}^e + n_i\langle\sigma v\rangle_{ion}^i}{n_i\langle\sigma v\rangle_{CX}^e + n_i\langle\sigma v\rangle_{ion}^i + n_e\langle\sigma v\rangle_{ion}^e} \tag{B.20}$$

where $\langle\sigma v\rangle_{ion}^i$ is the rate coefficient for the proton ionization. For example, after the first collision, a test flight would represent $\rho_{CX}(\gamma\omega)$ *atoms/sec*, with $(1 - \rho_{ion})$ $(\gamma\omega)$*atoms/sec* having been ionized. This weight attenuation process continues until w is less than some pre-assigned minimum weight

ω_{min}. At this point, one reaction between a pure charge exchange or ionization is chosen. In the case of the charge exchange reaction, ω remains unchanged and the flight is continued, while ω is set to be 0 and the flight is ended in the ionization case.

B.3 Scoring

At a collision, a weight of $(1 - \rho_{CX}) \cdot \omega$ is ionized. The sum

$$\tau_j = \sum (1 - \rho_{CX})\omega \qquad (B.21)$$

taken over all collisions in plasma zone j of all test flights, represents the ionization rate in zone j, in units of test flight weight. This is converted to S_j $ionizations/m^3$ by multiplying by γ and dividing by the volume vol_j of zone j,

$$S_j = \gamma\tau_j/vol_j \qquad (B.22)$$

The charge exchange ion power loss in zone j is equal to

$$\gamma \sum \rho_{CX}\, \omega(\kappa E^+ - E^0)/vol_j \qquad (B.23)$$

where the sum is over all collisions in zone j, κ is the charge exchange weight correction coefficient described as follows,

$$\kappa = \frac{\sigma_{CX}\|v\|}{\langle\sigma v\rangle_{CX}} \qquad (B.24)$$

where σ_{CX} is the charge exchange cross section and $v = v_{new} - v_{old}$ with the incoming test flight velocity v_{old}. A velocity of the neutral after the charge exchange reaction v_{old} is chosen from the Maxwellian distribution of ion velocities. E^0 is the energy of the incoming neutral and E^+ is the energy of the incoming ion. The power gained by ions due to ionization processes equals

$$\gamma \cdot \sum (1 - \rho_{CX}) \cdot w(E^0 - \rho'_{ion}E^{ion})/vol_j \qquad (B.25)$$

where

$$\rho'_{ion} = \frac{n_i\langle\sigma v\rangle^i_{ion}}{n_i\langle\sigma v\rangle^i_{ion} + n_e\langle\sigma v\rangle^e_{ion}} \qquad (B.26)$$

is the ion impact ionization probability, and E^{ion} is the energy necessary for ionization. The neutral

density n_{0j} in zone j is derived from the relation

$$S_j = n_{0j}(n_{ej} < \sigma_e v > + n_{ij} < \sigma_i v >) \tag{B.27}$$

where the only unknown is n_{0j}. The average energy of neutrals $\bar{E}_j^0$ ionizing in zone j can be computed independently and is given by

$$\bar{E}_j^0 = \gamma \cdot \sum (1 - \rho_{CX}) w E^0 / S_j \tag{B.28}$$

where the sum is taken as in Eq. B.21, and $E0$ is the neutral energy at a collision. Equations B.21 and B.28 cannot be used in zones without plasma, because the sums are empty there. In plasma-less regions a fictitious plasma of pseudo-ions Ψ is assumed, whose reaction

$$\Psi + H_0 \rightarrow \Psi + H_0 \tag{B.29}$$

leaves H_0 unchanged in every way. Taking the sum

$$\tau_j^\Psi = \sum w \tag{B.30}$$

over all collisions with pseudo-ions in zone j, the neutral density n_{0j} then obeys

$$S_j^\Psi = \gamma \tau_j^\Psi = \gamma \tau_j^\Psi = n_{0j} n_{\psi j} \langle \sigma v \rangle_\Psi \tag{B.31}$$

where $n_{\psi j}$ is the pseudo-ion density in zone j and $\langle \sigma v \rangle_\Psi$ is the rate coefficient of reaction B.29.

In the DEGAS code, the scorings are made not at each collision but at each pseudo-collision for the improvement of the statistics. For example, the sum in Eq. B.21 is replaced by the sum over all pseudo-collisions in zone j,

$$\tau_j' = \sum \frac{\lambda_{min}}{\lambda} (1 - \rho_{CX}) \omega \tag{B.32}$$

B.4 Neutral Reflection at Wall

In general, for each projectile/target combination, experiment or computation will give a 5-dimensional differential scattering distribution,

$$P(E, \alpha, v, \theta, \phi) v^2 \, dv \sin\theta d\theta d\phi \tag{B.33}$$

where E and α are the incident energy and polar angle, respectively. v, θ and ϕ are the velocity, polar and azimuthal angles of the reflected particle, respectively. The azimuthal angle is measured from the plane of the incident trajectory. To each incident E and α is associated the 3-dimensional conditional distribution,

$$P_{E,\alpha}(v,\theta,\phi)v^2 dv \sin\theta \, d\theta \, d\phi \qquad (\text{B.34})$$

The parameter of the reflection particle is obtained as follows. First v_0 is chosen from

$$f_{E,\alpha}^1(v) = \iint P_{E,\alpha}(v,\theta,\phi)dv\sin\theta \, d\theta \, d\phi \qquad (\text{B.35})$$

Given v_0 then θ_0 is picked from

$$f_{E,\alpha}^2(\theta) = \iint P_{E,\alpha}(v_0,\theta,\phi)d\phi \qquad (\text{B.36})$$

and finally, with v_0 and θ_0 known, ϕ_0 can be chosen from the distribution.

$$f_{E,\alpha}^3(\phi) = P_{E,\alpha}(v_0,\theta_0,\phi) \qquad (\text{B.37})$$

where $P_{E,\alpha}$ has been suitably normalized.

B.5 Atomic and Molecular Processes

In the DEGAS code, the following assumptions are included about the plasma-neutral interactions and neutral reflection.

1. The following reactions B.a-B.m show the plasma-neutral interactions included in the DEGAS code.

Charge Exchange:

$$p + H \rightarrow H + p \qquad (\text{B. a})$$
$$H_2^+ + H_2 \rightarrow H_2 + H_2^+ \qquad (\text{B. b})$$
$$p + H_2 \rightarrow H_2^+ + H \qquad (\text{B. c})$$

Electron Impact Ionization:

$$e + H \rightarrow e + H^+ + e \qquad (\text{B. d})$$
$$e + H_2 \rightarrow e + H_2^+ + e \qquad (\text{B. e})$$

Electron Dissociation:

$$e + H_2 \rightarrow e + H + H \tag{B. f}$$
$$e + H_2 \rightarrow e + H + H^+ + e \tag{B. g}$$
$$e + H_2^+ \rightarrow H + H \tag{B. h}$$
$$e + H_2^+ \rightarrow e + H^+ + e \tag{B. i}$$
$$e + H_2^+ \rightarrow e + H^+ + H^+ + e \tag{B. j}$$

Recombination:

$$e + p \rightarrow H \tag{B. k}$$

Ion Impact Ionization:

$$p + H \rightarrow p + H^+ + e \tag{B. l}$$
$$p + H_2 \rightarrow p + H_2^+ + e \tag{B. m}$$
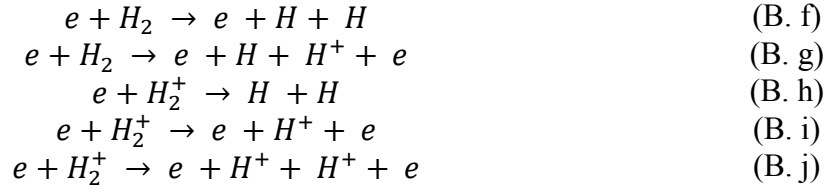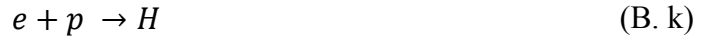
The rate coefficients or cross sections for the reactions are taken from the experimental data and theoretical results which are mainly referred in [9]. CX reaction rates are calculated as a function of the ion temperature, ion density and the energy of neutral particle. The model of electron impact ionization processes of neutral hydrogen includes the effects of multi-step ionization as a function of the plasma density and electron temperature.

2. The effect of the neutral-neutral and neutral-ion elastic scattering is neglected.

3. Neutral hydrogen atoms and molecules sticking to the wall desorb immediately as hydrogen molecules with the energy corresponding to a wall temperature.

Reference

[1]   R. D. Hazelitine and J. D. Meiss, Plasma confinement, Chapter 1.3 p.3 Addison-weslet publishing company (1992).

[2]   ITER project htt//www.iter.org/.

[3]   Y. Kamada et al., Nucl. Fusion, 41, No 10 (2001) 1311.

[4]   J.W. Hughes et al., Nucl. Fusion, 47 (2007) 1057.

[5]   R. Sakamoto et al., Nucl. Fusion 41 (2001) 381.

[6]   L. Yao et al., Nucl. Fusion 47 (2007) 1399.

[7]   M.M. Islam et al., Plasma Fusion Res. 11 (2016) 2402053.

[8]   K. Hosoi et al., Plasma Fusion Res. 9 (2014) 3402087.

[9]   A. Murakami et al., Plasma Phys. Control. Fusion 54 (2012) 055006.

[10]   K. Hosoi et al., Trans. Fusion Technol. 63 (2013) 244.

[11]   M. M. Islam et al., AIP Conf. Proc. 1771 (2016) 030018.

[12]   L. Yao et al., Nucl. Fusion 38 (1998) 631.

[13]   L. Yao et al., Nucl. Fusion 44 (2004) 420.

[14]   D. L. Yu et al.,Nucl. Fusion 52 (2012) 082001.

[15]   L. Nie et al., Plasma Phys. Control. Fusion 56 (2014) 055066.

[16]   X. R. Duan et al., Nucl. Fusion 50 (2010) 095011.

[17]   C. Y. Chen et al., J. Plasma Fusion Res. SERIES 9 (2010) 37.

[18]   A. Murakami et al., Plasma Fusion Res. SERIES. 9 (2010) 79.

[19]   A. Murakami et al., Plasma Fusion Res. 6 (2011) 1402135.

[20]   B. Pegourie et al., J. Nucl. Mater. 313-316 (2003) 539.

[21]   J. Bucalossi et al., 19th IAEA Conf. Lyon (2002) WX/P4-04.

[22]   H. Takenaga et al., Nucl. Fusion et al., 50 (2010) 115003.

[23]   H. Takenaga et al., Nucl. Fusion et al., 49 (2009) 075012

[24]   T. Mizuuchi et al., Contrib. Plasma Phys. 50 No. 6-7 (2010) 639

[25]   T. Mizuuchi et al., J. Nucl. Mater. 415 (2011) S443.

[26]   L. Zang et al., Phys. Plasmas 21 (2014) 042308.

[27]   P. T. Lang et al., Plasma Phys. Control. Fusion 47 (2005) 1495.

[28]   V. A. Soukhanovskii et al., Rev. Sci Instrum. 75 (2004) 4320-4323.

[29]   V. A. Soukhanovskii et al., 31st EPS Conf. on Plasma Phys. London, ECA, 28B (2004) P-2.190.

[30]   X. Zheng et al., Plasma Phys. Control. Fusion 55 (2013) 115010.

[31]   M. Inutake et al, Physi. Rev. Lett. 55 (1985) 939.

[32]   T. Tamano, Phys. Plasmas 2 (1995) 2321.

[33]   K. Yatsu et al., Nucl. Fusion 39 (1999) 1707.

[34]   S. A. Allen et al, Nucl. Fusion 27 (1987) 2149.

[35]   F. Sano et al., Nucl. Fusion 45 (2005) 1557.

[36]   T. Mizuuchi et al., Nucl. Fusion 47 (2007) 395.

[37]   D. B. Heifetz et al., J. Comp. Phys. 46 (1982) 309.

[38]   D. P. Stotler et al., Phys. Plasmas. 3 (1996) 4084.

[39]   M. Ichimura et al., Nucl. Fusion 28 (1998) 799.

[40]   M. Ichimura et al., J. Plasma Fusion Res. SERIES, 3 (2000) 58.

[41]   T. Imai et al., J. Plasma Fusion Res. 85, (2009) 378-382.

[42]   E. Kawamori et al., J. Plasma Fusion Res. SERIES 3 (2000) 473.

[43]   E. Kawamori, Ph. D. Thesis Univ. Tsukuba (2006).

[44]   Y. Kubota et al., Plasma Fusion Res. 2 (2007) S1057.

[45]   Y. Kubota, Ph. D. Thesis Univ. Tsukuba (2006).

[46]   A. L. Qualls et al., Proc. 13th Symp. Fusion Engineering, No. 2 (1989) p.1244.

[47]   A. Murakami et al., PhD Thesis, The Graduate University of Advanced Studies (2001).

[48]   J. D. Anderson "Modern compressible flow with historical perspective" Chapter 5, p.195, The McGraw-Hill Companies, (2004).

[49]   J. D. Anderson "Modern compressible flow with historical perspective" Chapter 3, p.80, The McGraw-Hill Companies, (2004).

[50]   NACA Technical Note No. 1651 (1948).

[51]   M. Yoshikawa et al., Journal of Instrumentation, 7 (2012) C03003.

[52]   W. Molvik, Rev. Sci. Instrum. 52 (1981) 704.

[53]   J. H. Foote et al., Rev. Sci. Instrum. 56 (1985) 5.

[54]   K. Muraoka, et al., J. Nucl. Mater. 176-177 (1990) 231.

[55]   N. Nishino et al., Plasma Fusion Res. 1 (2006) 035.

[56]   Y. Nakashima et al., J. Nucl. Mater. 363-365 (2007) 6016.

[57]   H. Kawano et al., J. Plasma Fusion Res. 2 (2007) S1126.

[58]   L. C. Johnson and E. Hinnov, J. Quant. Spectrosc. Radiat. Transf. 13 (1973) 333.

[59]   T. Fujimoto et al., J. Phys. Soc. Japan 54 (1985) 2905.

[60]   K. Sawada et al., Phys. Rev. E 49 (1994) 5565.

[61]   Y. Nakashima et al., J. Nucl. Mater. 196-198 (1992) 493.

[62]   M. Shoji, PhD Thesis, University of Tsukuba (1995).

[63]   S. Kobayashi PhD Thesis, University of Tsukuba (2001).

[64]   Y. Higashizono et al., Trans. Fusion Technol. 47, No. 1T (2005) 297.

[65]   Y. Nakashima et al., J. Plasma Fus. Res. 6 (2004) 546.

[66]   Y. Nakashima, et al., J. Nucl. Mater. 337-339 (2005) 466.

[67]   Y. Higashizono et al., J. Plasma Fus. Res. 2 (2007) S1087.

[68]   Y. Nakashima et al., J. Plasma Physics vol. 72, part 6 (2006) 1123.

[69]   Y. Nakashima, et al., Trans. Fusion Sci. and Technol. 51, No.2T (2007) 82.

[70]   K. Hosoi, PhD Thesis, University of Tsukuba (2014).

[71]   M. M. Islam et al., IOP Conf. Series: Journal of Physics: 959 (2018) 012007.